Characterization and optimization of a dual channel PERCA for the investigation of the chemistry of peroxy radicals in the upper troposphere

Deniz Kartal

Universität Bremen 2009

Characterization and optimization of a dual channel PERCA for the investigation of the chemistry of peroxy radicals in the upper troposphere

Vom Fachbereich für Physik und Elektrotechnik

der Universität Bremen

zur Erlangung des akademischen Grades eines

Doktor der Naturwissenschaften (Dr. rer. nat.)

genehmigte Dissertation

von

M.Sc. Deniz Kartal

wohnhaft in Bremen

1.	Gutachter:	Prof. Dr. J.P. Burrows
2.	Gutachter:	Prof. Dr. Peter Lemke

Eingereicht am: 01.09.2009

Tag des Promotionskolloquiums: 09.10.2009

INDEX

ABSTRACT

The research of peroxy radical chemistry is an important topic that provides essential knowledge about photo oxidant formation and night time chemistry. Peroxy radicals play an important role in the formation and depletion reactions of ozone in the troposphere. They also play a key role in the cleaning processes of the atmospheric pollution.

At the Institute of Environmental Physics (IUP) of the University of Bremen, laboratory studies are performed to characterize and design a dual channel reactor system (DUALER: DUal channel Airborne peroxy radical chemicaL amplifiER) for the measurements of peroxy radicals on an airborne platform in the upper troposphere. The IUP DUALER system, based on the PERCA (Peroxy Radical Chemical Amplification) technique was deployed on the DLR-Falcon 20 of German Aerospace Centre (DLR) during the measurement campaign AMMA SOP2 (African Monsoon Multidisciplinary Analysis, Special Observation Period 2).

The West African Monsoon (WAM) is associated with deep convective transport of air masses to the upper troposphere impacted by anthropogenic and natural emissions. The analysis of the measurement results of the DUALER has the aim of understanding the identification of different air masses with different photochemical activity and developing knowledge of source and sink processes of peroxy radicals, as well as the formation and destruction mechanisms of ozone in the upper levels of the troposphere during the WAM.

At the experimental part of this work, the implementation of a pressure chamber for improving the characterization procedure of the IUP DUALER for different pressure levels is presented and the results are compared with the performance of the instrumentation during AMMA.

INTRODUCTION

Peroxy radicals, HO_2 and RO_2, where R stands for any organic chain, play an essential role in the chemistry of the troposphere, particularly in the formation and depletion mechanisms of ozone. In addition, they can be used as indicators for the photochemical activity of the air masses. Radical chemistry in the troposphere has been the subject of intensive research and reviews (Clemitshaw et al., 2004; Monks et al., 2005). The quantification of the impact of radicals in a particular environment is a complex issue. Radicals are the intermediates of many chemical reactions. Therefore their impact results from the balance between existing sources and sinks of NO_x ($NO+NO_2$), CO, volatile organic compounds (VOC) and O_3. Consequently, there are still many unknowns concerning radical formation and effect both in clean and polluted atmospheres. Measurement data for high levels of the troposphere is very scarce; therefore the measurements performed at higher levels of the troposphere are important for understanding tropospheric chemistry.

The West African Monsoon (WAM) is believed to be critical for global atmospheric chemistry. The anthropogenic and biogenic sources of the trace gases play an important role in the oxidizing cycles of the troposphere and are summarized in Figure 1. The natural sources depending on the vegetation type, soil moisture and temperature are expected to change with changing climate. The emissions of VOC, which are important precursors of peroxy radicals, depend on the vegetation type. The tropical forest canopy is, for instance, the main source of isoprene (Zimmerman et al., 1988, Guenther et al., 1995). Higher atmospheric carbondioxide concentrations and temperatures are expected to increase isoprene emissions. Lelieveld et al., 2008 have proposed that natural isoprene oxidation recycles OH efficiency in low NO_x air through reactions of organic peroxy radicals.

In addition, tropical soils are an important source of NO (Yienger and Levy et al., 1995), and forest soils are one of the main sources of atmospheric dinitrogenoxide which is an important greenhouse gas. Regarding the NO_x budget, the production of NO by lightening in convective clouds is also an important source of NO_x especially at West Africa which is the most electrically active region of the world.

Another important issue in the study of atmospheric photochemistry over Africa is the biomass burning which remains as the most important anthropogenic source of trace gases in West Africa. Under ideal conditions when the oxygen supply is enough, combustion of the organic matter produces water vapour and carbon dioxide. As the oxygen supply is never sufficient consequently the combustion is incomplete and pyrolysis of vegetable matter lead to the formation of reduced compounds such as CO, CH_4, VOC, NO, NH_3, H_2S, SO_x and aerosols.

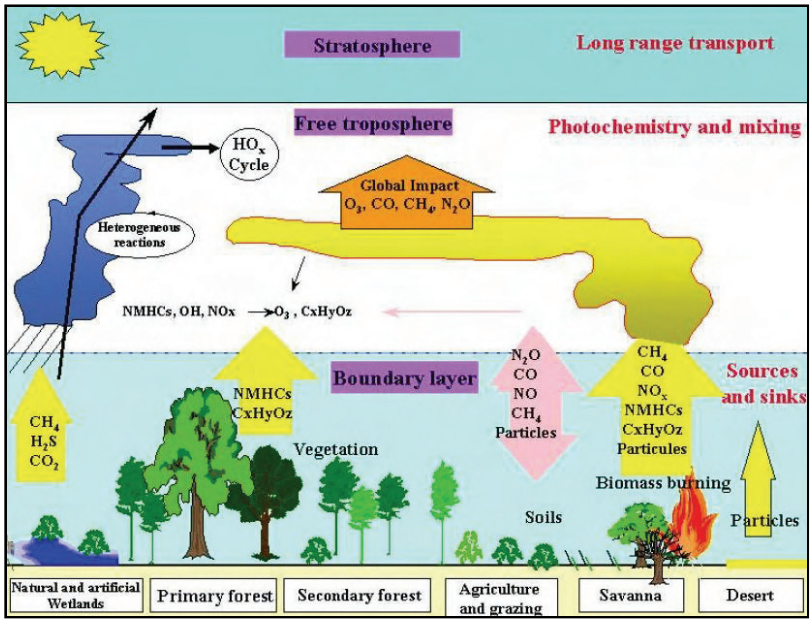

Figure 1 Overview of major chemical species in the WAM region, their fates and impacts. (International Science Plan for AMMA May 2005).

The deep convection events associated with the monsoon can transport these precursors and their oxidation products to the upper troposphere and lower stratosphere where they can be transported on regional and global scales. (International Science Plan for AMMA May 2005). West Africa is a vast zone where several types of mesoscale convective systems (MCS) develop according to the latitude, surface conditions and topography. MCS is usually defined as a single cumuliform and well vertically developed cloud or a cluster of such clouds, of typical horizontal extent 100x100 km^2, the mesoscale, between the local and synoptic scale. In particular, the MCS enclosed into synoptic-scale African Easterly Waves during the West African Monsoon are considered to be the origin of about 40% of the Atlantic tropical cyclones and responsible for troposphere-stratosphere exchange (Augustí-Panareda, and Beljaars et al., 2008). The outflow of the boundary of a MCS is a suitable environment for lifting, leading to an effective transport of trace gases, aerosols, and water vapour from the boundary layer into the free atmosphere.

West Africa is therefore a suitable environment for investigating the photochemical activity by the measurement of peroxy radicals in air masses impacted by MCS. The knowledge about the chemical composition of these air masses during intense convective episodes is scarce. The ozone formation is expected to be favoured by the vertical transport of hydrocarbons and peroxides as the peroxy radicals are produced by UV photolysis and react rapidly with NO which is also transported vertically and horizontally transported, or produced by lightning. The total yield of formation of ozone depends on UV radiation, potential losses of radicals (aerosols, clouds), and the vertical budget of radical precursors (Cantrell et al., 2003a, c).

The Institute of Environmental Physics of the University of Bremen (IUP-UB) participated in the international measurement campaign AMMA (African Monsoon Multidisciplinary Analysis) which took place during the wet monsoon season in August 2006 in West Africa. IUP-UB contributed with the measurements of the total sum of peroxy radicals using the PERCA (**Pe**roxy **R**adical **C**hemical **A**mplification) technique on board of the German scientific aircraft DLR-Falcon (DLR: Deutsches Zentrum für Luft und Raumfahrt).

PERCA is one of the most frequently used technique for the measurement of the total sum of peroxy radicals, has been gradually improved since it was proposed by Cantrell and Stedman et al., 1982, and there is abundant literature describing new developments (Reiner et al., 1997; Cantrell et al., 1996, 2003a-b; T.J. Green et al., 2003, Mihele and Hastie et al., 1998; Mihele et al., 1999; Reichert et al., 2003), and characterisation for the ambient measurement of peroxy radicals, as well as the deployment in diverse polluted and remote areas (e.g. Monks et al., 1996, Carslaw et al., 1999; Burkert et al., 2001a-b, 2003; M.D. Andrés Hernández et al, 2001; Cantrell et al., 1996a; Volz-Thomas et al., 2003; Zanis et al., 2003; Fleming et al., 2006a-b). Recent developments addresses the speciation of different peroxy radicals, in particular the separate detection of the organic peroxy radicals to HO_2 (Edwards et al., 2003; Fuchs et al., 2008).

In most of the cases, the measurement system consists of a single reactor and detector. However, for remote areas and airborne measurements, dual systems, comprising two identical reactors and one or two detectors, have recently been developed in order to increase sensitivity and accuracy in the case of rapid changing background concentrations which can interfere in the radical determination (Cantrell et al, 1996b; Green et al., 2003).

The main points of the present work are the improvement of the PERCA technique by developing a DUALER instrument (DUal channel Airborne peroxy radical chemicaL amplifiER) for airborne measurements and the analysis of the peroxy radical measurements carried out during the AMMA measurement campaign on board of the research aircraft DLR-Falcon.

This doctoral thesis reports on the laboratory studies carried out for the characterization and the optimization of the DUALER instrument and on the peroxy radical airborne measurements performed with the same DUALER.

The present study is therefore a contribution to the investigation of the PERCA technique applications on airborne platforms. The results obtained during the measurement campaign in West Africa provide important information for further understanding of photochemical processes and photochemical activity of air masses during the WAM.

1 Theoretical background

The investigation of the peroxy radical chemistry in the upper troposphere is a central objective of the present work. In this context, the chemistry of peroxy radicals in the troposphere and the related aspects of atmospheric physics are briefly introduced in this chapter. More detailed information can be found in consulting books (Seinfeld and Pandis, 1997; Egbert Boeker, 1994; Richard P. Wayne, 2000). In addition the experimental techniques for peroxy radicals are summarized. The last section of this chapter gives brief information about the chemical kinetics supporting the modelling studies of this work.

1.1 Main physical features of the atmosphere

1.1.1 Vertical variation of atmospheric pressure and temperature

A main feature of the atmosphere of the Earth is the vertical variation in pressure and temperature. As a consequence chemical and physical atmospheric properties are changing vertically. These changes are the basis to divide the atmosphere into layers.

The lowest layer of the atmosphere is the troposphere, extending from the Earth's surface up to the tropopause, which is at different altitude, depending on the latitude and the time of year. Over the Equator the average height of tropopause is about 18 km and at poles about 8 km. The troposphere has a negative temperature gradient with increasing altitude. The vertical mixing is rapid; if the lifetime of a molecule is long enough it can across the entire troposphere.

The stratosphere extends from the tropopause to the stratopause (45 to 55 km altitude), the temperature increases with altitude, and as a consequence the vertical mixing is slow. The increase in temperature in this layer (Figure 1.1) is caused by the UV absorption by the stratospheric ozone layer.

The mesosphere is the layer where the temperature decreases with altitude to the mesopouse which is the coldest point of atmosphere. The vertical mixing within the mesosphere is rapid. The mesosphere extends from 50 to 80 km altitude and the extension of mesopause is from 80 to 90 km.

The thermosphere has a positive temperature gradient, as a result of the absorption of short wavelength radiation by N_2 and O_2 that allows rapid vertical mixing. The ionosphere is a region between the upper mesosphere and lower thermosphere where ions are produced by photoionization.

The exosphere is the layer where the gas molecules with sufficient energy can escape from the Earth's gravitational attraction.

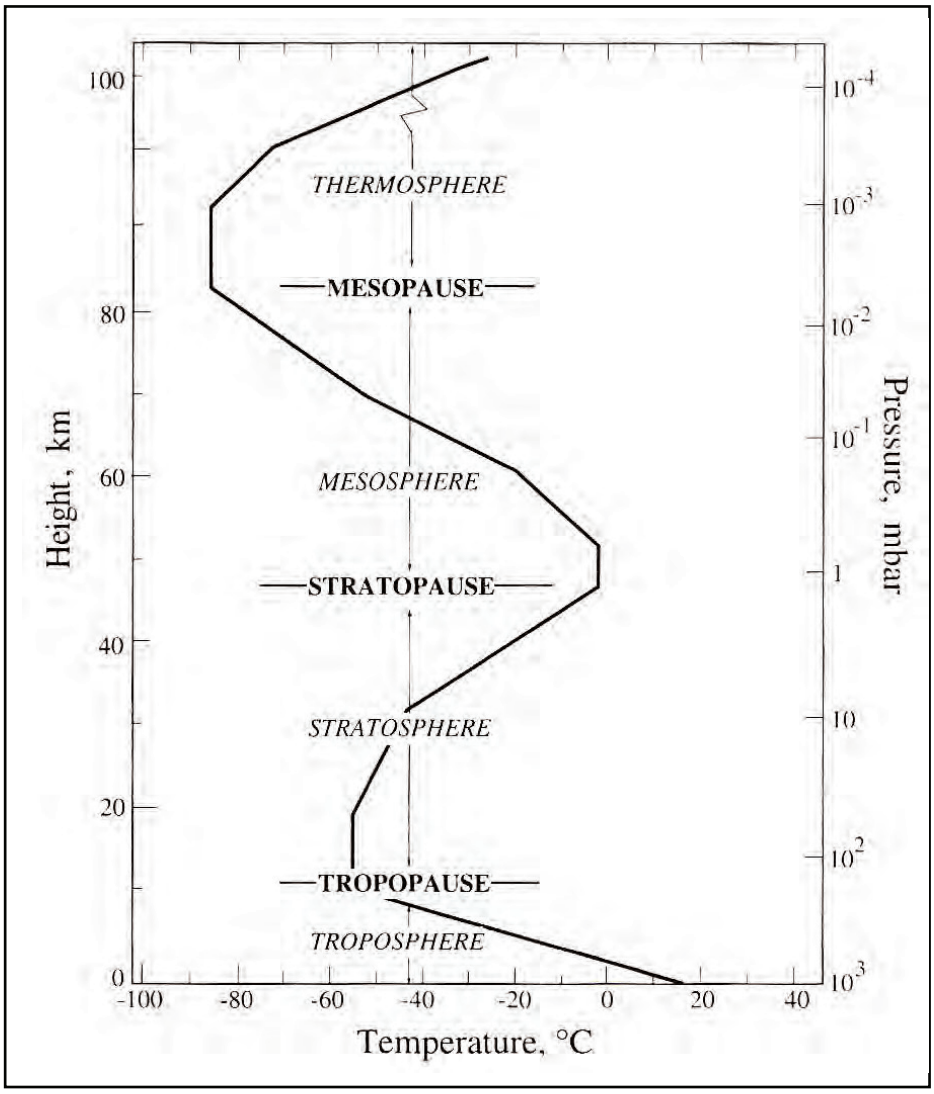

Figure 1.1 Layers of atmosphere and the temperature and pressure variation of the vertical profile. (Seinfeld; Pandis "Atmospheric Chemistry and Physics" 1996)

The decreasing of pressure (Figure 1.1) with height can be explained with the hydrostatic equation, as the pressure at each height is due to the weight of the air located above:

$$\frac{dP(z)}{dz} = -\rho(z) * g \tag{1.1}$$

$\rho(z)$ is the mass density of air at height z, g is the acceleration due to the gravity and P is the pressure. Taking into account the ideal gas law,

$$\rho(z) = \frac{M_{air} * P(z)}{R * T(z)} \tag{1.2}$$

where M_{air} is the molecular weight of air (28.97 g mol^{-1}) ,T temperature, R the universal gas constant 8.314 J mol K^{-1}.

Thus,

$$\frac{dP(z)}{dz} = -\frac{M_{air} * g * P(z)}{R * T(z)} \tag{1.3}$$

which can be written as

$$d\ln(P(z)) = -\frac{dz}{\frac{R * T(z)}{M_{air} * g}} \tag{1.4}$$

$$P(z) = P_0 * \exp\left\{-\int_0^z \frac{M_{air} * g}{R * T(z)} dz\right\} \tag{1.5}$$

Where $H(z) = \frac{R * T(z)}{M_{air} * g}$ is a characteristic length scale for decrease of pressure with height.

If the temperature can be taken to be approximately constant, just to obtain a simple approximate expression for P(z) then the pressure decrease with height is approximately exponential;

$$\frac{P(z)}{P_0} = e^{-z/H} \tag{1.6}$$

Where $H = RT/M_{air}\, g$ is called the scale height. The concept of the scale height can be applied individually to atmospheric species, $H_i = RT/M_i\, g$, $P_i(z)$ partial pressure of species i. The scale height depends on the molecular weight so the high molecular gas masses tend to concentrate close to the Earth's surface, and lighter gasses at higher altitude. Because of the overwhelming effect of turbulent mixing in the atmosphere, however, this separation based on molecular mass does not occur in the lower atmosphere. In the lower atmosphere the scale height H is about 8 km at T=273K.

The vertical temperature decrease with altitude in Figure 1.1 is expected to be the result of the work of expansion. Considering a parcel of gas is moving up and down in the atmosphere that is in pressure equilibrium, but thermally isolated from the surroundings, enables to calculate the change of temperature with altitude. Since no heat flows (adiabatic conditions) and the gas is dry, the temperature profile calculated is the dry adiabatic lapse rate. The first law of the thermodynamics can be expressed as

$$dU = dq + dw \tag{1.7}$$

Where dU is the change of the internal energy, dq the heat supplied to the system and dw the work done on it. In the case of a box of gas with a volume V that has no heat exchange with the surrounding (adiabatic conditions, dq=0 and dw=-PdV) and the gas inside is dry, according to these considerations the following expressions can be derived.

From the definition of enthalpy, H,

$$dH = dU + PdV + VdP \tag{1.8}$$

According the considerations,

$$dH = VdP \tag{1.9}$$

The heat capacity of the gas at constant pressure, C_p, is defined as $\left(\frac{dH}{dT}\right)_P$, so that

$$C_p dT = VdP \tag{1.10}$$

Considering the equation (1.1) thus;

$$C_p dT = -V\rho g dz \tag{1.11}$$

For the unit mass of gas, for which $V=1/\rho$, replacing the C_p by the value appropriate to unit mass (c_p) leads to;

$$-\frac{dT}{dz} = \frac{g}{c_p} = \Gamma_d \tag{1.12}$$

The dry adiabatic lapse rate, Γ_d, depends only on the acceleration due to the Earth's gravity and the average heat capacity per unit mass of the atmospheric gases.

For wet, but not saturated air the lapse rate is estimated by an extension of equation (1.12) by using the w_m mass fraction of water vapour ;

$$c_p = (1 - w_m) * c_{p\,air} + w_m * c_{p\,water\,vapour} \tag{1.13}$$

The calculated value for Γ_d is ≈ 9.8 K km^{-1}.The lapse rate for humid air is Γ_h always smaller than Γ_d being $3 < \Gamma_h < \Gamma_d$.

This information allows determining whether any particular dry atmosphere is stable or unstable with respect to convection. If the actual temperature gradient in the atmosphere

$-\left(\frac{dT}{dz}\right)$ is less than Γ_d (Figure1.2 (b)) the atmosphere is stable. Any attempt of an air parcel to rise is counteracted by PdV cooling that makes it colder and denser than its surroundings.

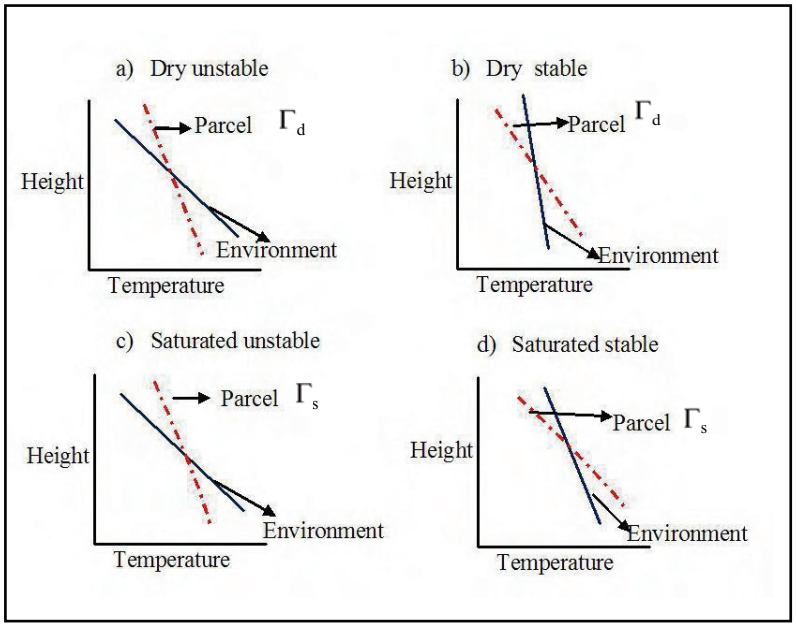

Figure1.2 Comparison between environmental lapse rate and parcel lapse rate for different degrees of atmospheric stability. (Archie W. Culp Jr, Principles of energy Conversion, 1991)

Conversely, if there is a tendency for $-\left(\frac{dT}{dz}\right)$ to be greater than Γ_d convection would be set up (Figure1.2 (a)). The stability conditions in saturated air are the same as in unsaturated ones (Figure1.2 (c) (d)). Partial saturation is treated in two stages, with Γ_d being applicable until temperatures low enough to cause condensation, and Γ_s which is the lapse rate for saturated air thereafter. In these circumstances, a situation known as conditional instability can arise. If the atmospheric lapse rate is smaller than Γ_d but higher than Γ_s, the atmosphere is stable unless some kind of forced lifting (for example; wind) raises gas to an altitude where condensation occurs. From this point of view the atmosphere is unstable.

1.1.2 Large Scale Motion of the atmosphere

1.1.2.1 The General Circulation

There is a continuous exchange of moisture, momentum, and energy exchange between the atmosphere, ocean and land. However, there is a balance of total input and output of the energy budget of Earth. The amount of input and output energy is however, not balanced locally. The uneven distribution is caused by latitudinal variations in insolation and differences in absorptivity of the Earth's surface which lead to large scale air motions of the Earth.

To predict the general pattern of macro scale air circulation on the Earth, the consideration of both tendency for thermal circulation and the influence of Coriolis force is necessary. Figure 1.3 shows the nature of the general circulation of the atmosphere. At either side of the Equator is thermal circulation, in which warm tropical air rises and cool, northern air flows toward the equator. The circulation does not extend all the way to the poles because radiative cooling of the upper northward flow causes it to fall at about 30° N and S latitude. The Coriolis force acting on these cells leads to easterly winds, called trade winds. The same situation occurs in the polar regions, in which warm air from the temperate zones moves northward in the upper levels, eventually cooling by radiation and subsiding at the poles. The result is the polar easterlies.

In the temperature regions, 40° and 55° latitude, both tropical and polar regions are not influencing significantly. The major feature of these temperature regions are large-scale weather systems, which result in the circulation shown in Figure 1.3. The surface winds in the Northern Hemisphere are westerlies because of the Coriolis force.

At the boundaries between thermal circulation at the Equator, 30°, and 55° N and S latitude there are calm regions. The observed net precipitation near the Equator and the polar front is explained by rising air that cools. At 30° N and S latitude a strong subsidence of dry air occurs, since the air loses its moisture upon ascension in the equatorial zone. As a result, net evaporation of the oceans occurs from 10° to 40° N and S latitude.

The general circulation pattern shown in Figure 1.3 does not represent the actual state of atmospheric circulation on a given day. The irregularities of land masses and their surface temperatures tend to disrupt the smooth global circulation patterns described above. Another influence that tends to break up the zonal patterns is the Coriolis force. Air that converges at low levels toward the region of low pressure must also execute a circular motion because of Coriolis forces. The effect of friction at the surface is to direct the winds at low levels in part toward regions of low pressure, producing a inward spiralling motion. This vortex-like motion is given the name cyclone. The center of a cyclone is usually a rising column of warm air. Similarly, a low level diverging from high pressure region will spiral outward. Such a region is called anticyclone.

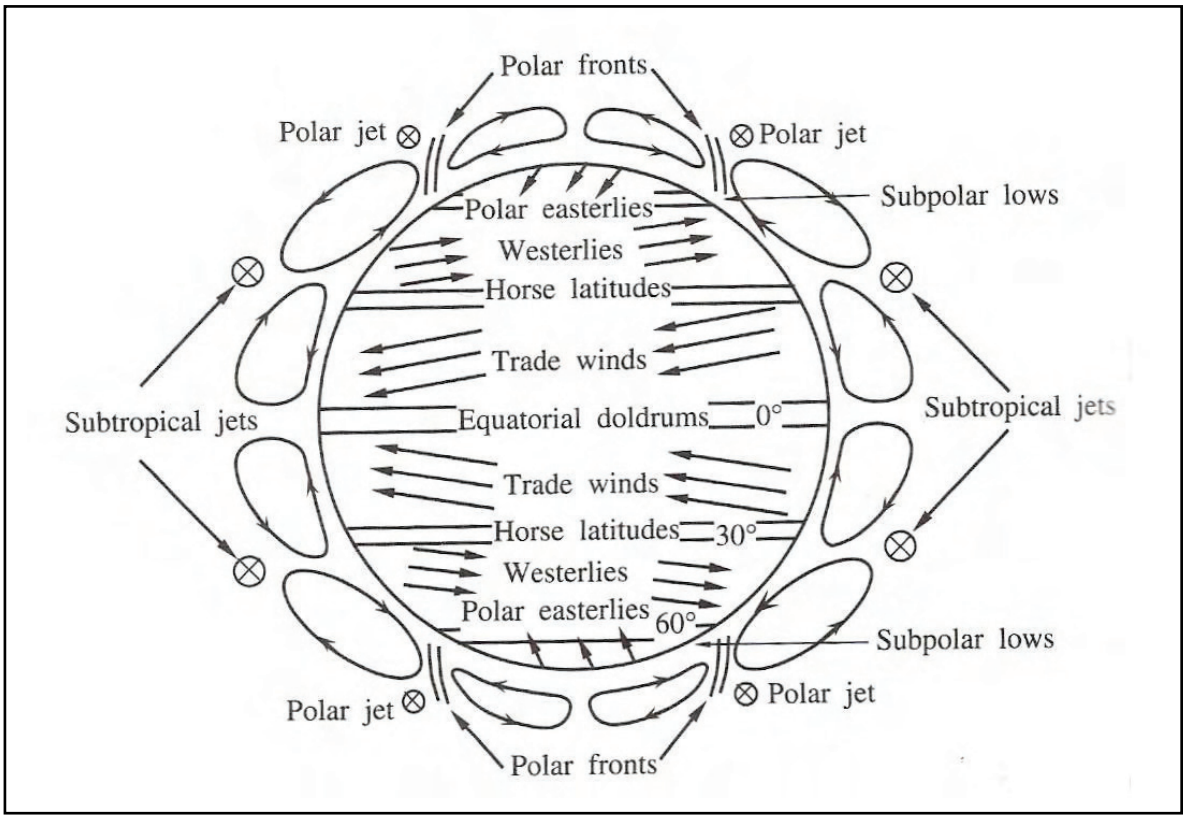

Figure 1.3 Schematic representation of the general circulation of the atmosphere. (Seinfeld; Pandis "Atmospheric Chemistry and Physics" 1996)

1.1.2.2 Troposphere-Stratosphere Exchange

The troposphere-stratosphere exchange plays an important role in transporting anthropogenic species to the stratosphere. A direct consequence of this is the well known depletion of the stratospheric ozone. In the opposite, the downward transport from the stratosphere represents an important source of ozone into the troposphere and establishes the basic removal mechanism for many stratospheric species, including those involved in ozone depletion. The vertical mixing rates of stratosphere and troposphere are different and the inhomogeneity of the chemical composition and radiative environment of the stratosphere makes it difficult to determine the rate of the tropospheric species supplied to and removed from stratosphere regions.

The troposphere-stratosphere exchange occurs when the air is forced into the stratosphere by tropical cumulus convective turrets. In the tropics moist convection strongly transports material vertically. The shading in Figure 1.4 shows the lower stratosphere most directly affected by large scale-motion mentioned in section 1.1.2.1.

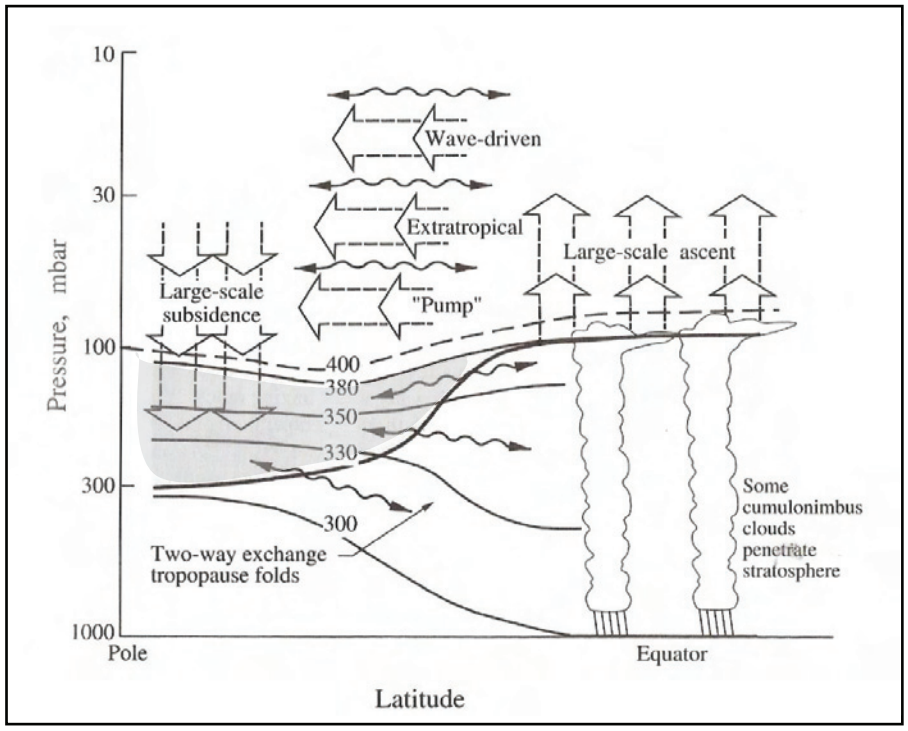

Figure 1.4 Dynamical aspects of stratosphere-troposphere exchange. (Holton et al., 1995)

The wave-driven pumping from the extratropical stratosphere results with the net flux from the tropical troposphere to the stratosphere (the large horizontal arrows in Figure 1.4), (Holton et al., 1995). The shaded region of the stratosphere, is the only part of the stratosphere that can receive material from the troposphere by transport along surfaces of constant potential temperature.Stratospheric air above this region cannot reach the troposphere without slowly descending. Exchange between the shaded region of stratosphere and the troposphere can be significantly faster than that between the stratosphere overlaying this region and the shaded region. Much of the ozone transport from the lower most stratosphere into troposphere is believed to occur in connection with tropopause folding events.

1.1.2.3 Mesoscale convective systems

The term mesoscale convective system (MCS) is a convective system that is considerably larger than an individual thunderstorm. They form when clouds occurring in response to convective instability amalgamate and organize upscale into a single cloud system with a very large cirriform cloud structure. The MCS are an important link between atmospheric convection and larger scale atmospheric circulation; they are associated in various ways with larger-scale wave motions (Carbone et al., 2002).

A mesoscale convective system consists of convective and stratiform precipitation, and the components of MCS develop mesoscale circulation as they mature. With the latent heating and cooling in the convective region, the upward motion takes the form of a deep

layer ascent drawn into the MCS. The ascending layer overturns as it rises but overall retains a coherent layer structure. The large scale flow determines the direction of the middle level layer of inflow enters the stratiform region of the MCS and descends in response to diabatic cooling at middle to low levels. A middle level mesoscale convective vortex, which may contribute to tropical cyclone development, develops in the stratiform region and prolongs the MCS. The propagation of an MCS may have an discrete component but may further be influenced by waves and disturbances generated both in response to the MCS and external to the MCS (Hauze et al., 2004).

MCSs are account for a large proportion of precipitation in both the tropics and warmer midlatitudes. Long –lasting, slow mowing MCSs are a major cause of flooding, and these systems often contain hail, strong winds and even tornadoes.

1.1.3 Radiation and molecule interaction in the atmosphere

Atmospheric molecules can absorb or scatter radiation. The absorption is the interaction process between the matter (gas, solid, fluid) and a photon leading to an energy transfer which affects the molecular structure.

Absorption of high energy atom $AB + h\nu \rightarrow AB^*$ may result in following photophysical and photochemical processes;

Luminescence:	$AB^* \rightarrow AB + h\nu$
Ionization :	$AB^* \rightarrow AB^+ + e$
Quenching :	$AB^* + M \rightarrow AB$ (M is any molecule acting as energy carrier)
Dissociation :	$AB^* \rightarrow A + B$
Chemical reaction :	$AB^* + C \rightarrow A + BC$

Each molecule has a particular absorption cross section, which is the ability of the molecule to absorb a photon, is wavelength and at most cases temperature dependent.

Scattering occurs if the photon changes its direction after the interaction with the molecule. The scattering can be elastic when the photon conserves its energy or inelastic when there is an energy exchange between the molecule and the photon. In the atmosphere there are two types of scattering called Rayleigh and Mie scattering. The scattering efficiency and the phase function Mie parameter depends on the ratio of particle size and wavelength as shown in Equation(1.14):

$$m = \frac{2 * \pi * d}{\lambda} \tag{1.14}$$

d is the diameter of the particle assumed to be spherical and λ the wavelength of the photon .

Rayleigh scattering occurs when the particle size is small compared to the wavelength of the photon ($m \ll 1$). The blue sky is due to the strong scattering of the shorter wavelengths. Mie scattering occurs when the particle size is at the same range with the wavelength of the photon ($m \approx 1$). The result of Mie scattering is the white colour of the clouds.

1.2 Radicals in the Troposphere

Peroxy radicals (hydroperoxyl HO_2, and organylperoxyl RO_2; R=organic chain), play an essential role in the chemistry of the troposphere, particularly in the formation and depletion mechanisms of ozone. The pathways of the reactions differ at polluted and clean air masses.

The photolysis of NO_2 is the only tropospheric source of ozone;

$$NO_2 + h\nu(\lambda < 420nm) \rightarrow NO + O\ ^3P \quad (1.15)$$

$$O(^3P) + O_2 \rightarrow O_3 \quad (1.16)$$

$$NO + O_3 \rightarrow NO_2 + O_2 \quad (1.17)$$

This is a null cycle in the absence of peroxy radicals. The peroxy radicals react with NO and lead to ozone production;

$$HO_2 + NO \rightarrow OH + NO_2 \quad (1.18)$$

$$RO_2 + NO \rightarrow RO + NO_2 \quad (1.19)$$

Reactions (1.18) and (1.19) are additional sources of NO_2 so that the peroxy radicals are leading to O_3 production in polluted areas.

In low concentrations of NO_x, they destroy ozone;

$$HO_2 + O_3 \rightarrow OH + 2O_2 \quad (1.20)$$

$$OH + O_3 \rightarrow HO_2 + O_2 \quad (1.21)$$

$$2O_3 \rightarrow 3O_2$$

1.2.1 Sources of peroxy radicals

The peroxy radical chemistry is related to the hydroxyl radical OH, which dominates the oxidation reactions of the troposphere. OH is produced by the photolysis of ozone at $\lambda < 320\,\text{nm}$ which leads to a singlet oxygen atom that reacts with H_2O;

$$O_3 + h\nu(\lambda < 320\,\text{nm}) \rightarrow O(^1D) + O_2 \quad (1.22)$$

$$O(^1D) + H_2O \rightarrow 2OH \quad (1.23)$$

In addition, nitrous acid, HONO, photolysis rapidly at wavelengths $\lambda \leq 400\text{nm}$ during daytime and yields OH;

$$HONO + h\nu(\lambda \leq 400\text{nm}) \rightarrow OH + NO \quad (1.24)$$

At night time the reaction of nitrate radical (NO_3) and HO_2 acts as a night time source of OH;

$$HO_2 + NO_3 \rightarrow OH + NO_2 + O_2 \quad (1.25)$$

Conversely, the main sources of the peroxy radicals are the oxidation reactions of OH with carbonmonoxide (CO), methane (CH_4), and volatile organic compounds (VOC). Formaldehyde (HCHO) acts as a source of peroxy radicals by photolysing wavelengths $\lambda < 340\text{nm}$ and oxidation reaction with OH (see reactions(1.36),(1.37),(1.38)). The nitrate radical is a night time source of peroxy radicals. The reactions of ozone with VOCs containing a double bond contribute as HO_2 source to the peroxy radical chemistry. All these processes are explained more in detail in the following in relation to the atmospheric significance of the peroxy radicals in the following.

In the presence of NO_x the oxidation of CO leads to a net production of ozone;

$$OH + CO \xrightarrow{O_2} HO_2 + CO_2 \quad (1.26)$$

$$HO_2 + NO \rightarrow OH + NO_2 \quad (1.18)$$

$$NO_2 + h\nu(\lambda < 420\text{nm}) \rightarrow NO + O\ ^3P \quad (1.15)$$

$$O(^3P) + O_2 \rightarrow O_3 \quad (1.16)$$

$$CO + 2O_2 + h\nu \rightarrow CO_2 + O_3 \quad (1.27)$$

The oxidation of methane (CH_4), the simplest alkane, with OH is an important source of peroxy radicals:

$$CH_4 + OH \rightarrow CH_3 + H_2O \quad (1.28)$$

The methyl radical reacts with O_2 to produce the methyl peroxy radical CH_3O_2,

$$CH_3 + O_2 + M \rightarrow CH_3O_2 + M \quad (1.29)$$

Under tropospheric conditions methyl peroxy radical can react with NO, NO_2 and HO_2 radicals, and other organic peroxy radicals (RO_2), being the reactions with NO and HO_2 radicals most important (Seinfeld; Pandis "Atmospheric Chemistry and Physics").The reaction with NO leads to the formation of the methoxy (CH_3O) radical,

$$CH_3O_2 + NO \rightarrow CH_3O + NO_2 \quad (1.30)$$

The methoxy radical reacts with oxygen to produce formaldehyde and hydroperoxyl ;

$$CH_3O + O_2 \rightarrow HCHO + HO_2 \quad (1.31)$$

The reaction of CH_3O_2 with the HO_2 radical leads to the formation of methyl hydroperoxide;

$$CH_3O_2 + HO_2 \rightarrow CH_3OOH + O_2 \quad (1.32)$$

which can photolyse or react with the OH radical

$$CH_3OOH + h\nu \rightarrow CH_3O + OH \quad (1.33)$$

$$CH_3OOH + OH \rightarrow H_2O + CH_3O_2 \quad (1.34)$$

The overall oxidation process of methane can be written as follows (Figure 1.5):

$$CH_4 + OH \rightarrow CH_3 + H_2O \quad (1.28)$$

$$CH_3 + O_2 + M \rightarrow CH_3O_2 + M \quad (1.29)$$

$$CH_3O_2 + NO \rightarrow CH_3O + NO_2 \quad (1.30)$$

$$CH_3O + O_2 \rightarrow HCHO + HO_2 \quad (1.31)$$

$$HO_2 + NO \rightarrow OH + NO_2 \quad (1.18)$$

$$2(NO_2 + h\nu(\lambda < 420nm) \rightarrow NO + O\ ^3P) \quad (1.15)$$

$$2(O(^3P) + O_2 \rightarrow O_3) \quad (1.16)$$

Net: $$CH_4 + 4O_2 + h\nu \rightarrow HCHO + 2O_3 + H_2O \quad (1.35)$$

The net production of the CH_4 oxidation is HCHO and ozone. The reaction pathways after the oxidation of CH_4 and CO_2 vary according to the NO_x concentrations in the troposphere.

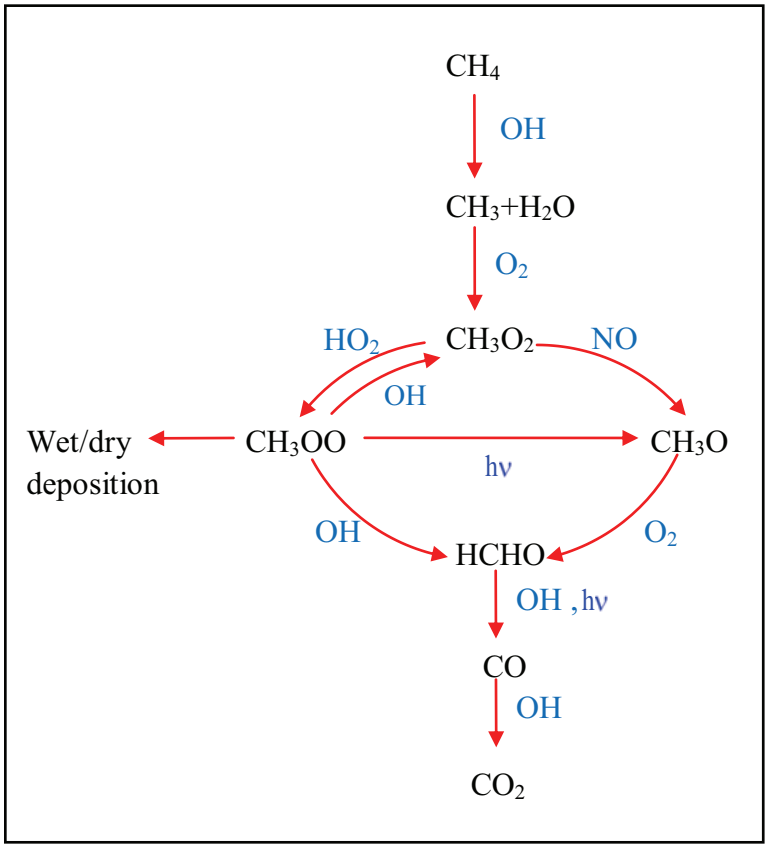

Figure 1.5 Atmospheric methane oxidation chain.(Seinfeld; Pandis "Atmospheric Chemistry and Physics" 1997)

The oxidation and the reaction of methyl peroxy radical CH_3O_2 with NO leads to production of formaldehyde (Figure 1.5). HCHO is emitted from anthropogenic sources and is a product of the oxidation of hydrocarbons. The formaldehyde can photolyse and oxidise to produce peroxy radicals through different pathways:

$$HCHO + h\nu(\lambda < 340\,nm) \rightarrow H_2 + CO \quad (1.36)$$

$$HCHO + h\nu(\lambda < 340\,nm) \rightarrow H + HCO \quad (1.37)$$

$$HCHO + OH \rightarrow CHO + H_2O \quad (1.38)$$

The reaction (1.36) is followed by;

$$HCHO + h\nu(\lambda < 340\,nm) \rightarrow H_2 + CO \quad (1.36)$$

$$CO + OH \xrightarrow{O_2} HO_2 + CO_2 \quad (1.26)$$

$$H_2 + OH \xrightarrow{O_2} HO_2 + H_2O \quad (1.39)$$

$$\text{Net:} \quad HCHO + h\nu(\lambda < 340\,nm) + 2OH + 2O_2 \rightarrow CO_2 + 2HO_2 + H_2O \quad (1.40)$$

The reaction (1.37) is followed by;

$$HCHO + h\nu(\lambda < 340\,nm) \rightarrow H + CHO \quad (1.37)$$

$$CHO + O_2 \rightarrow HO_2 + CO \quad (1.41)$$

$$CO + OH \xrightarrow{O_2} HO_2 + CO_2 \quad (1.26)$$

$$H + O_2 + M \rightarrow HO_2 + M \quad (1.42)$$

$$\text{Net:} \quad HCHO + h\nu(\lambda < 340\,nm) + 3O_2 + OH \rightarrow 3HO_2 + CO_2 \quad (1.43)$$

The reaction (1.38) is followed by;

$$HCHO + OH \rightarrow CHO + H_2O \quad (1.38)$$

$$CHO + O_2 \rightarrow HO_2 + CO \quad (1.41)$$

$$CO + OH \xrightarrow{O_2} HO_2 + CO_2 \quad (1.26)$$

$$HCHO + 2OH + 2O_2 \rightarrow 2HO_2 + CO_2 + H_2O \quad (1.44)$$

As mentioned above, the nitrate radical is a night time source of peroxy radicals. The nitrate radical is formed with the reaction of ozone and NO_2 (Wayne et al., [1991]);

$$NO_2 + O_3 \rightarrow NO_3 + O_2 \tag{1.45}$$

The nitrate radical photolyses rapidly during the day but, plays a dominant role in oxidation reactions of most of the organic compounds at night.

$$NO_3 + RH \rightarrow HNO_3 + R \tag{1.46}$$

$$R + O_2 \xrightarrow{M} RO_2 \tag{1.47}$$

The reaction of NO_3 with HO_2 can provide a night time source for OH;

$$NO_3 + HO_2 \rightarrow OH + NO_2 + O_2 \tag{1.48}$$

The OH produced in reaction (1.48) further oxidizes VOCs and produces peroxy radicals at night.

Another important source of HO_2 is the ozonolysis, i.e, the reaction of ozone with alkenes. The reaction mechanism differs according to the type of alkene. The reaction of ozone and alkenes continues as a primary ozonide which is not stable, and decomposes to produce a carbonyl compound and the so called "Criegee intermediate". Criegee intermediate decomposes via a number of pathways or is thermalized by collisions with the surrounding gas. The reaction for the simplest alkene is;

$$CH_2 = CH_2 + O_3 \rightarrow HCHO + [H_2COO]^* \tag{1.49}$$

One of the products of (1.49) is HCHO acting as a source of HO_2. The Criegee intermediate $[H_2COO]^*$ decomposes to H, HCO and OH with a total radical yield of approximately 0.45 (Paulson and Orlando, et al., 1996).

1.2.2 Sinks of Peroxy radicals

The loss reactions of the peroxy radicals are different in polluted and unpolluted air.

In unpolluted air (at low NO mixing ratios), the dominant loss processes of peroxy radicals are their self reactions.

$$HO_2 + HO_2 \xrightarrow{M} H_2O_2 + O_2 \quad (1.50)$$

$$HO_2 + CH_3O_2 \rightarrow CH_3O_2H + O_2 \quad (1.51)$$

$$CH_3O_2 + CH_3O_2 \rightarrow 2CH_3O + O_2 \quad (1.52)$$

The washout of the peroxides produced from the peroxy radical self reaction is a real sink of peroxy radicals. The oxidation of the peroxides (H_2O_2: hydrogen peroxide,CH_3O_2H: methylhydroxyperoxide) leads to a production of peroxy radicals as shown in the reactions (1.53) and (1.54).

$$H_2O_2 + OH \rightarrow HO_2 + H_2O \quad (1.53)$$

$$CH_3O_2H + OH \rightarrow CH_3O_2 + H_2O \quad (1.54)$$

The photolysis of peroxides leads to OH that further produce peroxy radicals and to formaldehyde which is a source of peroxy radicals.

$$H_2O_2 + h\nu(\lambda = \text{ nm}) \rightarrow OH{+}OH \quad (1.55)$$

$$CH_3O_2H + h\nu(\lambda = \text{nm}) \rightarrow HCHO + H + OH \quad (1.56)$$

In the clouds heterogeneous reaction can convert HO_2 to H_2O_2 by producing first the superoxide ion which then reacts with more HO_2;

$$[HO_2 \rightarrow H^+ + O_2^-]_{aq} \quad (1.57)$$

$$[HO_2 + O_2^- \xrightarrow{H^+} H_2O_2]_{aq} \quad (1.58)$$

Evaporation of clouds containing high concentrations of dissolved H_2O_2 could represent a net source of H_2O_2 to the atmosphere. However the H_2O_2 can also react with OH in the aqueous phase:

$$[OH + H_2O_2 \rightarrow H_2O + HO_2]_{aq} \quad (1.59)$$

so that the sequence of reactions (1.57), (1.58), (1.59) constitutes a free-radical sink,

$$[HO_2 \rightarrow H^+ + O_2^-]_{aq} \tag{1.57}$$

$$[HO_2 + O_2^- \xrightarrow{H^+} H_2O_2]_{aq} \tag{1.58}$$

$$[OH + H_2O_2 \rightarrow H_2O + HO_2]_{aq} \tag{1.59}$$

Net: $$[OH + HO_2 \rightarrow H_2O + O_2]_{aq} \tag{1.60}$$

1.3 Basics of Chemical Kinetics

The gas molecules can react only when a bond breaking process occurs due to the direct energy exchange of the colliding molecules. The frequency of the collisions per unit volume of gas molecules of type i and j with the mass m_i and m_j can be expressed as follows;

$$Z_{ij} - \left(\frac{8kT}{\pi m_{ij}}\right)^{1/2} \pi\sigma_{ij}^2 N_i N_j \ cm^{-3}s^{-1} \qquad (1.61)$$

N_i and N_j are the number of molecules of species i and j (cm^{-3}), $\left(\frac{8kT}{\pi m_{ij}}\right)^{1/2}$ is the root-mean-square of the relative speed of the i and j molecules, k is the Boltzmann constant. $m_{ij} = {m_i m_j}/{(m_i + m_j)}$ is the reduced mass, $\pi\sigma_{ij}^2$ is the so-called collision cross section of molecules i and j. At ambient temperature and pressure the mean time between molecular collisions can be shown from equation 1.61 to be on the order of 10^{-9}.

The collision of two molecules A and B should provide a sufficient energy to break the chemical bonds. As the two molecules i and j collide the potential energy changes, as shown in Figure 1.6.

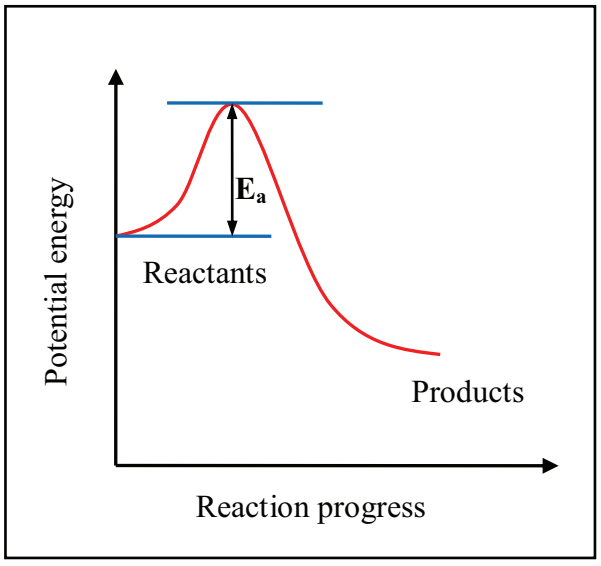

Figure1.6 A potential energy profile for an exothermic reaction. E_a activation energy of the reaction.

As the reaction proceeds, A and B come into contact, distort, and begin to exchange or discard atoms. The potential energy rises to a maximum and the cluster of atoms that corresponds to the region close to the maximum is called the activated complex. After the maximum, the potential energy falls as the atoms rearrange in the cluster, and it reaches a value characteristic for products. The climax of the reaction is the peak of the potential energy, which is called the activation energy, E_a. The activation energy is the minimum kinetic energy that reactants must have in order to form products. The fraction of collisions with a kinetic energy in excess of the energy E_a is given by the Boltzmann distribution as $e^{-E_a/RT}$. Hence, the exponential factor in (1.62) can be interpreted as the fraction of collisions that have enough kinetic energy to lead a reaction. The pre-exponential factor (A) is a measure of the rate at which collisions occur irrespective of their energy. Hence, the product A and $e^{-E_a/RT}$ gives the rate of successful collisions.

$$k = A e^{-E_a/RT} \tag{1.62}$$

A is the frequency factor, E_a the activation energy; collectively the quantities can be called Arrhenius parameters. T is the temperature, and R the universal gas constant.

The rate law of a unimolecular elementary reaction is first order in the reactant, if;

$$A \rightarrow B \qquad \frac{d[A]}{dt} = -k[A] \tag{1.63}$$

The process in equation (1.63) can be expressed graphically as in Figure 1.7

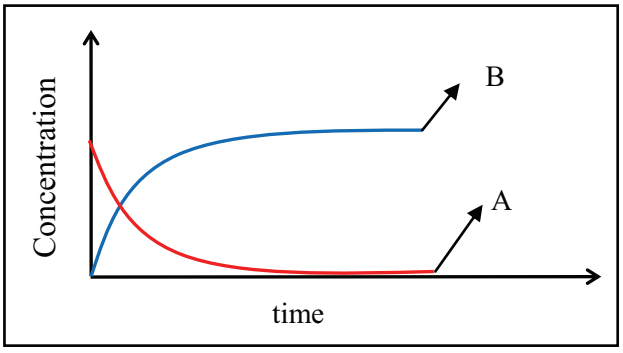

Figure 1.7 Graphical representation of the process in equation (1.63)

An elementary bimolecular reaction has a second-order rate law;

$$A + C \rightarrow B \qquad \frac{d[A]}{dt} = -k[A][C] \tag{1.64}$$

A bimolecular reaction is second-order because its rate is proportional to the rate at which the reactant species meet, which in turn is proportional to their concentrations. Bimolecular elementary reactions are believed to account for many homogeneous reactions.

The termolecular reaction can be expressed as;

$$A + B + M \rightarrow C + M \tag{1.65}$$

$$\frac{d[A]}{dt} = \frac{d[B]}{dt} = -\frac{d[C]}{dt} = k_r[A][B] \tag{1.66}$$

The rate of the termolecular reactions are pressure dependent. The reaction order depends on the M collision partner (that corresponds generally to N_2 and O_2 in atmosphere) concentration that changes with pressure. The termolecular reactions are third order reactions at low pressure and second order reactions at high pressure.

The determination procedure of the reaction rate needs to include the dependency pressure and temperature. The reaction can be described in two stages;

1. Activation : $A + B \rightarrow C^*$

2.a Stabilisation: $C^* + M \rightarrow C + M$

2.b Back reaction: $C \rightarrow A + B$

After the activation of the reaction (1.65) the C intermediate may stabilize due to the transferred excess energy by the collision partner M, or may react back to A and B. The probability of the stabilisation, which means the occurrence probability of the reaction, depends on the M concentration. A parameterization of the reaction rate for termolecular reactions has been developed by (Troe, [1983]);

$$k_r(M,T) = \frac{k_0(T)[M]k_\infty(T)}{k_0(T)[M] + k_\infty(T)} F(M, k_\infty(T), k_0(T)) \tag{1.67}$$

k_0 is the reaction rate coefficient for the low pressure;

$$k_0 = \lim_{[M]\rightarrow 0} k_r(T,M) \tag{1.68}$$

k_∞ is the reaction rate coefficient for high pressure;

$$k_\infty = \lim_{[M]\rightarrow \infty} k_r(T,M) \tag{1.69}$$

F function is the broadening factor and is expressed as;

$$F = 0.6^{\left\{1+\left[\log_{10}\left(\frac{k_0(T)[M]}{k_\infty(T)}\right)\right]^{-2}\right\}^{-1}} \tag{1.70}$$

The temperature dependence is fitted to the measured data by the following relation;

$$k_0(T) = k_0^{300}\left(\frac{T}{300}\right)^{-n}, k_\infty(T) = k_\infty^{300}\left(\frac{T}{300}\right)^{-m} \tag{1.71}$$

The exponent n is for low pressure and m is for high pressure determined. The values for k_0^{300} , k_∞^{300} ,n, m is reported either by experimental results or by model calculations.

1.4 Measurement techniques of Peroxy radicals

The high reactivity, short life time, and low concentrations of peroxy radicals make the direct measurement difficult. Common used methods to measure radicals are indirect measurement techniques. The indirect methods are depending on the conversion of peroxy radicals to other chemical species which can be detected and quantified more accurately. The indirect measurement techniques are Laser Induced Fluorescence (LIF), Chemical Ionisation Mass Spectroscopy (CIMS), and the chemical amplification technique (PERCA). The only direct measurement of peroxyradicals is the Matrix Isolation-Electron Spin Resonance (MIESR).

1.4.1 Laser Induced Fluorescence (LIF)

Laser Induced Fluorescence (LIF) can be used to determine the ambient concentration of OH and HO_2.The OH is detected in a continuous free jet of ambient air expanding through a nozzle into low-pressure detection chamber (Hard et. al., 1984; Hofzumahaus et. al., 1996). The excitation of OH occurs with a laser beam at 308 nm. The fluorescence signal of excited OH molecules from their ground state into the first electronically excited state at low pressure is measured.

The HO_2 is measured by LIF after the conversion to OH by the addition of NO to the measurement air. This method allows to measurement of OH+HO_2 but not of RO_2.The recent developments of LIF technique enable to measure RO_x radicals ($= RO_2 + RO + HO_2 + OH$) by adding a large excess of NO and CO in at reduced pressures (RO_x mode). When only CO is added HO_2 and OH is converted in to HO_2 (HO_x mode). Comparison of the different measurement modes of RO_x, HO_x, and OH, concentrations of HO_2 and RO_2 can be determined (Fuchs, H. et al., 2008). The principle of the calibration is based on the photolysis of water vapour with 185 nm. serving as a source of OH and HO_2 (Holland et al., 1995).

1.4.2 Matrix Isolation-Electron Spin Resonance (MIESR)

MIESR is the only existing direct measurement technique of peroxy radicals (Mihelcic et al., 1985, 1990, 1993).

The air sample is collected on a gold coated cold finger cooled to 77 K in a vacuum D_2O-ice matrix. The samples are analysed in laboratory conditions using the Electron Spin Resonance (ESR) technique to obtain the finger prints of radicals as a result of the interaction of the unpaired electron in the radicals with a strong magnetic field. The paramagnetic properties caused of the unpaired electron of radicals results in a spectrum that is fitted with reference spectra, to determine the measurement results. (Mihelcic et al., 1990).

NO_2, NO_3, HO_2, $CH_3C(O)O_2$ and the sum of the organic peroxy radicals can be measured with this technique. MIESR enables the discrimination of HO_2 from organic peroxy radicals

1.4.3 Chemical Ionisation Mass Spectroscopy (CIMS)

CIMS bases on the chemical ionization of H_2SO_4 formed in a chain reaction which is established by adding NO and SO_2 to the sampled air. (Eisele and Tanner et al., 1991)

The following reactions take place

$$RO_2 + NO \rightarrow RO + NO_2 \quad (1.72)$$

$$RO + O_2 \rightarrow R_{-H}O + HO_2 \quad (1.73)$$

$$HO_2 + NO \rightarrow OH + NO_2 \quad (1.18)$$

$$OH + NO \xrightarrow{M} HONO \quad (1.74)$$

$$OH + SO_2 \xrightarrow{M} HSO_3 \quad (1.75)$$

$$HSO_3 + O_2 \xrightarrow{M} SO_3 + HO_2 \quad (1.76)$$

The chain reaction ends up with the conversion of SO_3 to sulphuric acid;

$$SO_3 + H_2O \xrightarrow{M} H_2SO_4 \quad (1.77)$$

The H_2SO_4 molecules are converted to ions with nitrate ions;

$$H_2SO_4 + NO_3^- \rightarrow HSO_4^- + HNO_3 \quad (1.78)$$

The HSO_4^- ions are detected by mass spectrometry.

1.4.4 Peroxy Radical Chemical Amplification (PERCA)

The chemical amplification is an indirect measurement technique for the determination of peroxy radicals. Generally, the PERCA instrument consists of a reactor where the chemical conversion and amplification of peroxy radicals into NO_2 takes place, a control unit providing gas for the required reactions, and a detector for the detection of NO_2.

In this chapter the general aspects of the chemical amplification method is going to be explained. The PERCA instrument that is used within this work and its calibration procedure is presented more in detail in Chapter 3 (Experimental Set-up).

1.4.4.1 Principle of the measurement technique

The chemical amplification method measures the total sum of the hydroperoxy HO_2, and organylperoxy RO_2, R= organic chain, ($RO_2^* = HO_2 + \sum RO_2$).

RO_2^* is converted into NO_2 by adding NO and CO at the reactor. This leads to a chain reaction whose length determines the number of NO_2 molecules produced per peroxy radical and consequently the chemical amplification of HO_2 ;

$$HO_2 + NO \rightarrow NO_2 + OH \tag{1.18}$$

$$CO + OH \xrightarrow{O_2} CO_2 + HO_2 \tag{1.26}$$

The organylperoxy radicals react similary. RO_2 radicals are converted to RO by reacting with NO. The conversion mechanism of RO to HO_2 depends on the structure of the organic chain "R". One possible pathway is H extraction by O_2 yielding a carbonyl product;

$$RO_2 + NO \rightarrow NO_2 + RO \tag{1.72}$$

$$RO + O_2 \rightarrow R_{-H}O + HO_2 \tag{1.73}$$

$$RO \rightarrow ..... \rightarrow HO_2 + \text{organic product(s)} \tag{1.79}$$

As $\sum RO_2 \gg \sum RO$ and $[HO_2] >> [OH]$ in the troposphere, the measured signal should be a good approximation to RO_2^*. A modulated signal (Figure 1.8) is obtained by alternatively adding NO/CO and NO/N_2 to the reactor, corresponding to the measurement of total NO_2 in the amplification mode (i.e., from the conversion of peroxy radicals plus other background trace gases producing NO_2 in their reaction with NO, plus NO_2 itself) and of background NO_2 in the background mode (i.e., total NO_2 minus NO_2 from the conversion of peroxy radicals). The content of peroxy radicals in the air can be calculated from the difference between amplification and background (Figure 1.8), ΔNO_2, provided that the length of the chain reaction (CL) is determined in the laboratory.

$$CL = \frac{([NO_2]_{amplification} - [NO_2]_{background})}{[RO_2^*]} \tag{1.80}$$

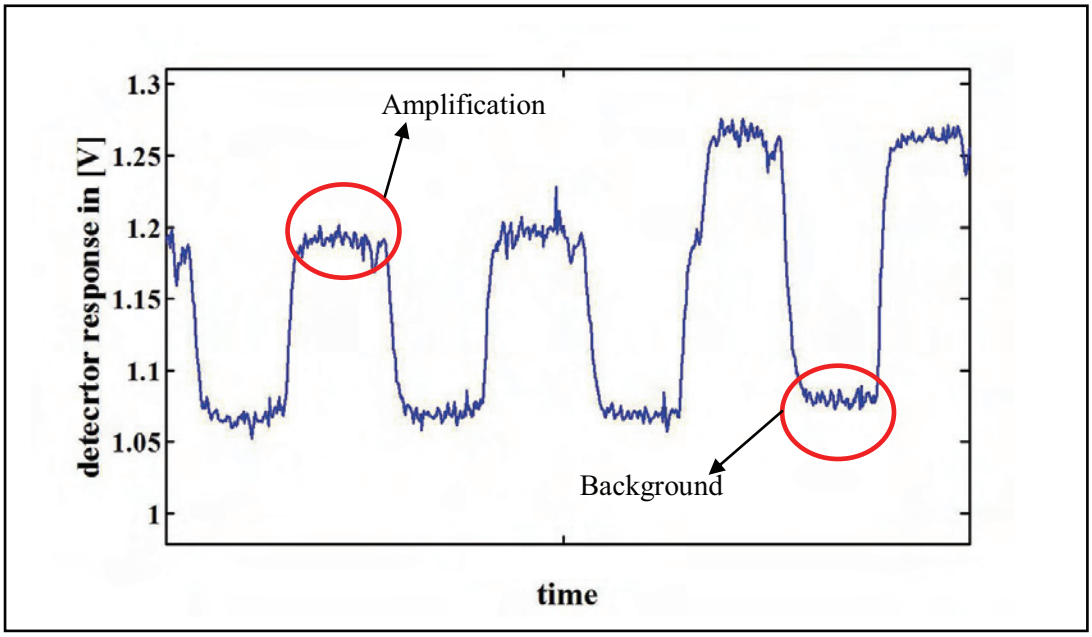

Figure 1.8 Example of modulation signal.

The CL has a limited extension because the chemical conversion of peroxy radicals in NO_2 is in competition with loss reactions in the reactor. Main loss reactions are;

$$RO_2^* + \text{wall} \rightarrow \text{nonradical products} \qquad (1.81)$$

$$OH + NO \xrightarrow{M} HONO \qquad (1.74)$$

$$OH + NO_2 \xrightarrow{M} HNO_3 \qquad (1.82)$$

$$HO_2 + NO_2 \underset{}{\overset{M}{\rightleftharpoons}} HO_2NO_2 \qquad (1.83)$$

$$HO_2 + HO_2 \rightarrow H_2O_2 + O_2 \qquad (1.50)$$

$$OH + HO_2 \rightarrow H_2O + O_2 \qquad (1.84)$$

Under the operating conditions with high NO and CO mixing ratios, radical-radical loss reactions play a secondary role. The final extent of the chemical conversion i.e., the CL depends on the shape and material of the reactor. The amplification cycle and the loss reactions can be summarized as in Figure 1.9.

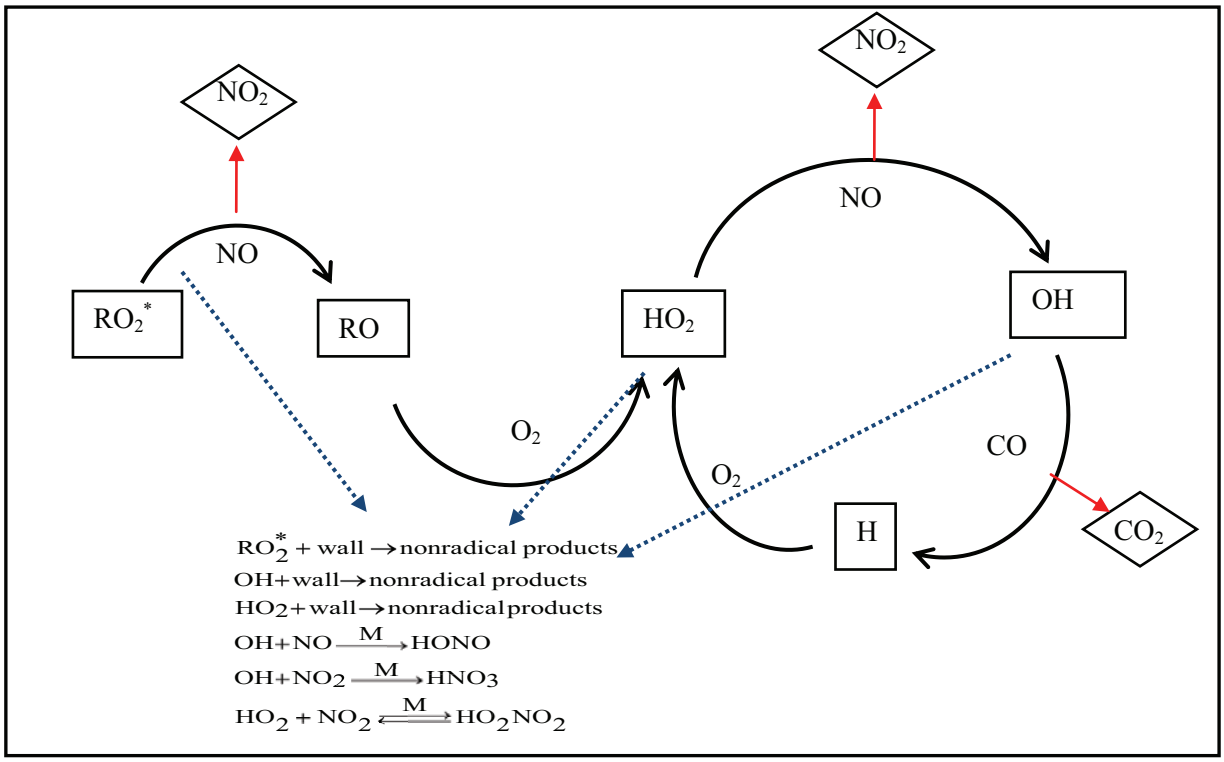

Figure 1.9 Amplification cycle and main loss reactions of the chemical amplification method.

1.4.4.2 General factors influencing the CL

The mixing ratio of the reagent gases added to the reactor affects the CL. Therefore, at the operation conditions of the PERCA the mixing ratios must be kept constant. Figure 1.10 represents a simulation of CL for different CO and NO mixing ratios determined by using the model described in Chapter 4.

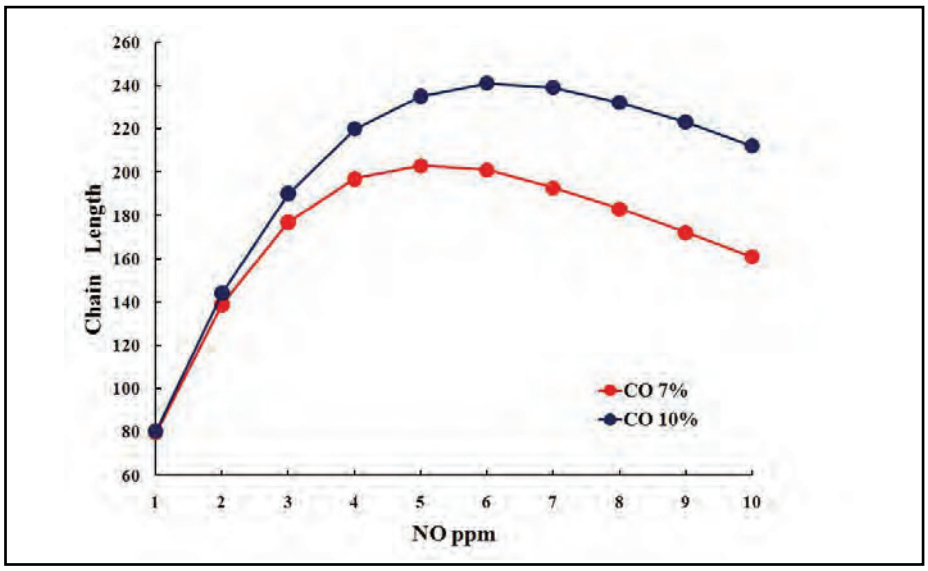

Figure 1.10 Simulation of CL for a mixture of 25 ppt HO_2 and 25ppt CH_3O_2 for different NO and CO mixing ratios.

As can be sen in Figure 1.10 the absolute CL increases by increasing CO mixing ratio. The CL has a maximum value between 4 and 6 ppm NO and decreases with increasing NO mixing ratio due to the loss reaction (1.74). Similar results are obtained by other studies (Clemitshaw et al., 1997; Cantrell et al., 1993)

The wall losses depend on the nature of the geometry, surfaces and material of the reactor where the amplification reactions are taking place. The wall losses of peroxy radicals before reaching the reaction zone are depending on the composition and nature of the sampled RO_2. The peroxy radicals that have a larger organic chain R have generally lower wall loss rates (Peroxy Radical Inter-comparison Experiment; PRICE 1994).

The dependency of the water vapour of the chain length is one of the most important effects on the efficiency of the chemical amplification method. The studies of Mihele et al., 1998;Reichert et al., 2003 show that CL decrease with increasing relative humidity. One possible explanation for the decrease in CL with relative humidity is a reaction involving HO_2, H_2O dimers and CO or NO, leading to CO_2 and OH or HNO_3 (Reichert et al., 2003). Mihele et al., 1998 proposed a reaction between H_2O, NO, HO_2 leading to HNO_3 as responsible for this effect.

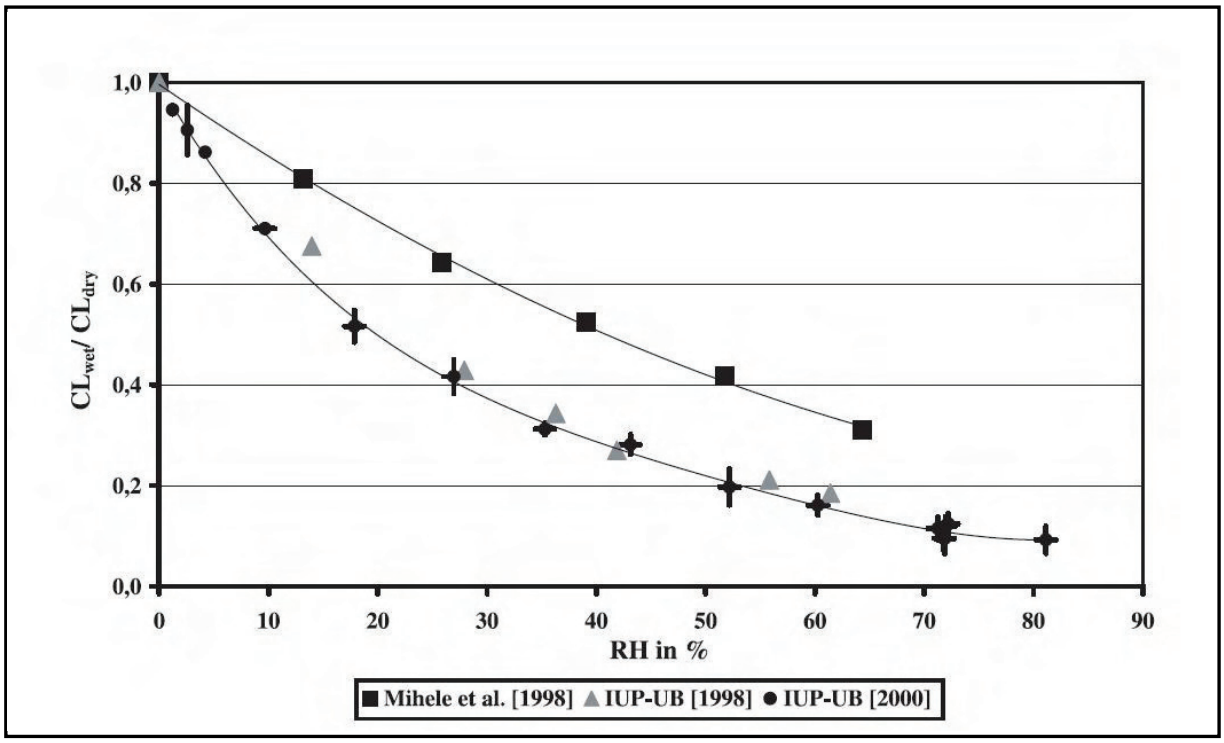

Figure 1.11 Experimental results of CL_{wet}/CL_{dry} as a function of relative humidity from different studies: square dots (Mihele et al., 1999), circle dots (Reichert et al., 2003), triangle dots (Stöbener, 1999).

The trend of the decrease in Figure 1.11 of CL in all studies is not similar. The results of Mihele et al., 1998 were obtained with a different teflon reactor to which 2 ppm NO , 4% CO were added. In contrast, the experiments performed by Reichert et al., 2003; Stöbener (1999) obtained with a glass reactor to which 3ppm NO, 9% CO mixing ratios were added. The discripancies seen in Figure 1.11 might be the result of the different extension of wall and chemical losses with varying relative humidity. The CL dependency on relative humidity should be characterized accurately for each particular set up.

2 Objectives

Peroxy radicals are key intermediates in most of the oxidation reactions taking place in the atmosphere. The determination of these very reactive species is crucial for the investigation of photochemical processes especially those related to ozone formation and depletion mechanisms. The present knowledge of the amount and vertical distribution of peroxy radicals is not sufficient to explain the photochemical activity of upper tropospheric air masses. Therefore, the measurement of peroxy radicals is essential.

PERCA (**PE**roxy **R**adical **C**hemical **A**mplifier) is a commonly used technique for the measurement of peroxy radicals on different platforms. Critical issues related to ground based measurements of PERCA are known and investigated for several years by different research groups during inter-comparison measurement campaigns. In recent years, PERCA has been deployed on aircrafts in order to gain information about the vertical distribution of peroxy radicals in the troposphere. The airborne measurements of PERCA are still in a development stage. This work aims to contribute to this development with the optimization and characterization of a PERCA instrument as well as with its deployment and operation in an airborne platform. In addition, peroxy radical measurements using this instrument are carried out within the framework of the international project AMMA (African Monsoon Multidisciplinary Analysis).

The objectives of the present work can be summarized as follows;

1. Development and optimization of a DUALER (**DU**al channel **A**irborne peroxy radical chemica**L** amplifi**ER)** instrument for the airborne peroxy radical measurements.

   This DUALER should cope with variations in pressure and in background concentrations (mainly O_3) related to the vertical and forward motion of the airborne platform.

2. Laboratory characterization of the developed instrument by experiments performed in a pressure chamber by simulating the ambient pressure conditions during the airborne measurements.

   The implementation of a pressure chamber to the calibration procedure of PERCA aims to become a tool for the characterization of airborne inlets. Main objective of these experiments is the determination of the amplification factor (chain length) at different ambient pressures and the characterization of the performance of the components of the instrumentation at different ambient pressures.

3. Development of a box model for case studies with special focus on the investigation of the effect of wall losses, which significantly affects the total amplification and conversion of peroxy radicals at the reactor.

4. Measurements of peroxy radicals within the AMMA (African Monsoon Multidisciplinary Analysis) project and subsequent interpretation of results.

   This part of the work aims to gain a deeper insight into peroxy radical chemistry and abundance in the middle and upper troposphere during the West African Monsoon (WAM) period. Special focus of interest is the chemical composition in the outflow of convective clouds and the vertical distribution of peroxy radicals.

3 Experimental

The present chapter focuses on the description of the set up deployed in the scientific aircraft DLR-Falcon (Deutsches Zentrum für Luft und Raumfahrt) during the AMMA measurement campaign and the calibration procedures used to characterize the instrument. Critical aspects and parameters are discussed in detail. The chapter ends with a detailed analysis of the errors involved in the determination of the chain length.

3.1 Dual Channel PERCA: DUALER

The DUALER developed at the Institute of Environmental Physics of University of Bremen (IUP-UB) is designed with the purpose of keeping the pressure of the measurement system constant in order to optimize the stability of the instrument response at changing pressure conditions during airborne measurements. (see Chapter 6 Results and Discussion).

3.1.1 Main components of the DUALER

The DUALER consists of a double reactor inlet and an instrumented rack. The rack of the DUALER is the operation unit of the system. The main components of the DUALER are schematically represented in Figure 3.1 and Figure 3.2.

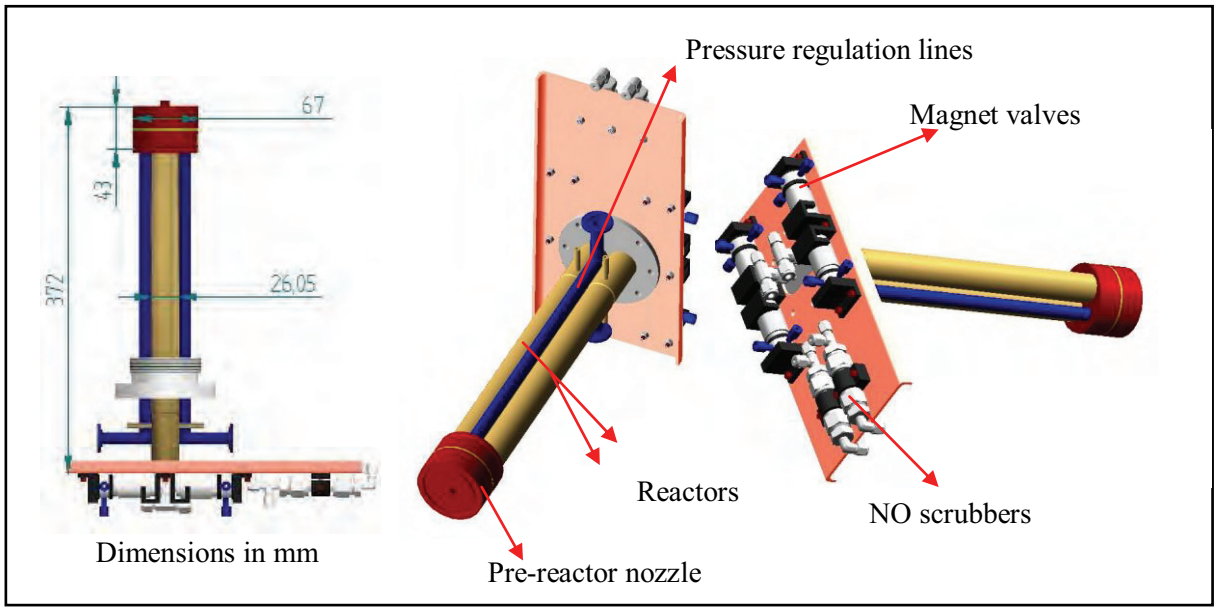

Figure 3.1 Three different views of the DUALER inlet constructed at the IUP-UB.

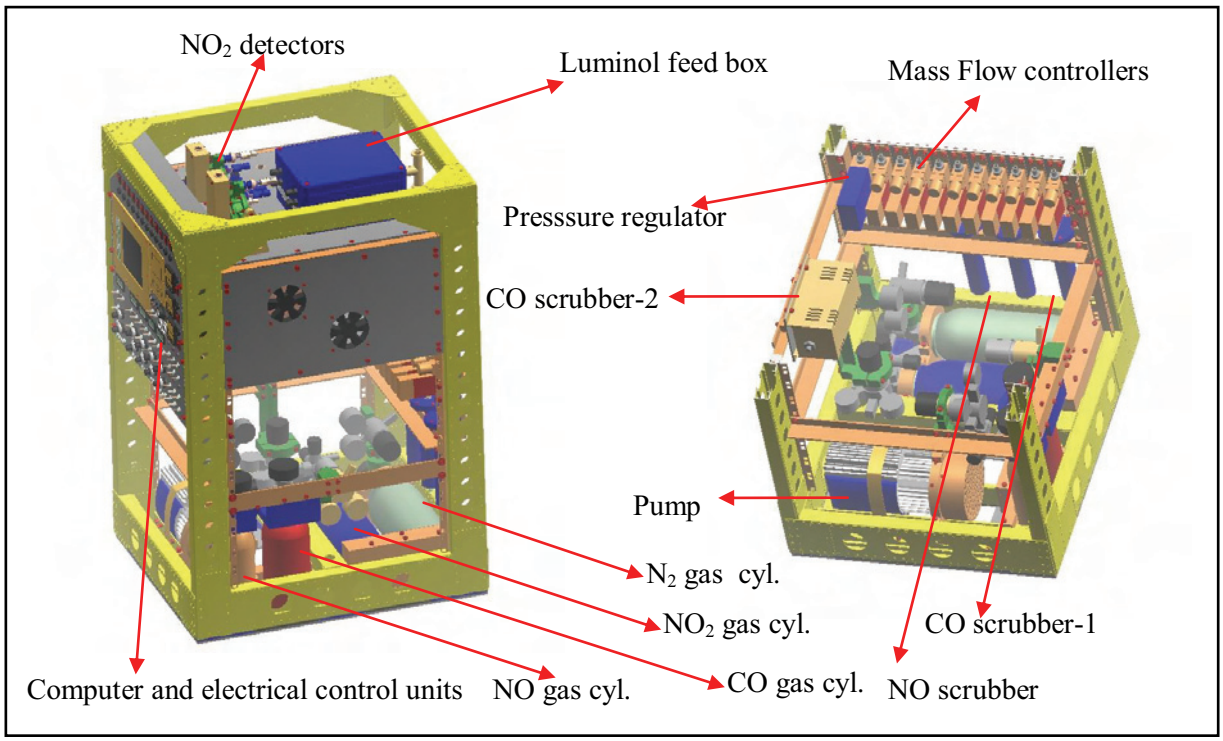

Figure 3.2 Components of the DUALER rack.

The DUALER inlet is made from stainless steel. All the inner surfaces in contact with the sampled air are coated with Teflon to minimize wall losses. The main parts of the DUALER inlet are:

Pre-reactor nozzle: In this unit the air is sampled and the pressure of the DUALER inlet is regulated. The reactors and the pressure lines are connected to this nozzle which has a volume of 54,5 cm^3 until the reactor entrances (Figure (3.3)).

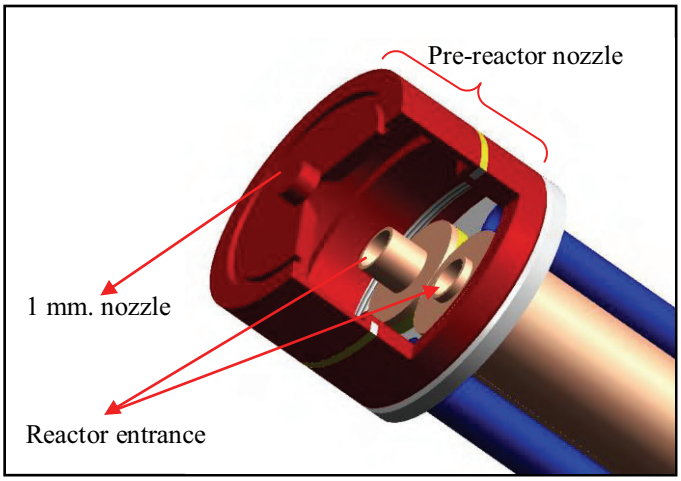

Figure 3.3 Pre-reactor nozzle

Reactors: The DUALER inlet consists of two identical reactors (21 mm ID, 310 mm L). Each reactor comprises two concentrical stainless steel tubes with 1 mm difference in diameter. The main body of the reactor is screwed in a stainless steel tube as seen in Figure 3.4. The space between the tubes is used as a gas pathway for the gases to the first addition point which consists of 8 orifices 1.5 mm ID drilled radially at the top of the reactors. The second addition point of the reactors is a T– connector located at the bottom.

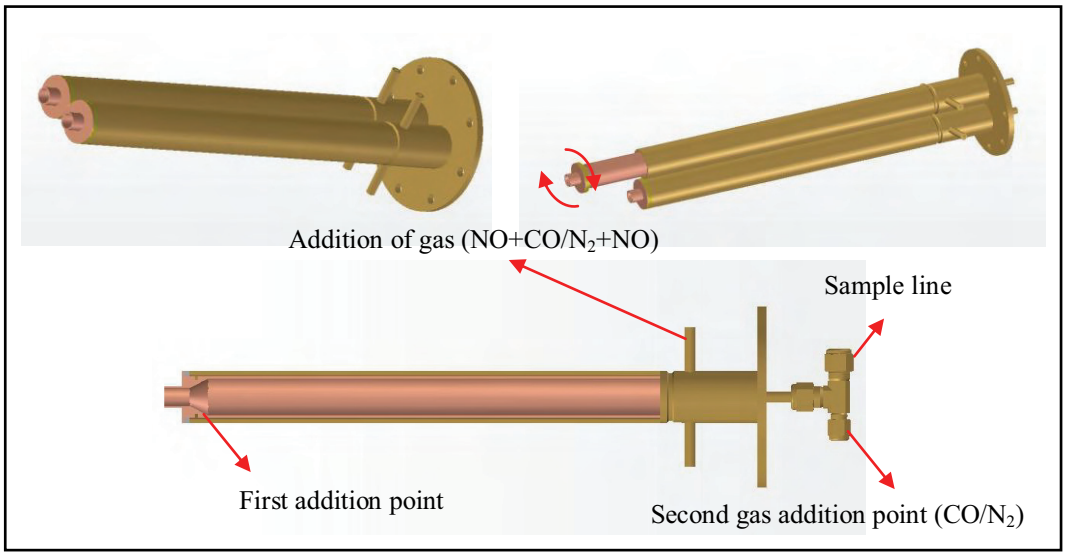

Figure 3.4 A detailed view of DUALER reactors.

Magnet valves and NO scrubber: The alternately addition of CO and N_2 to the first and second addition points of the reactors is operated by 3-way magnet valves. The NO scrubbers filled with $FeSO_4$ remove traces of NO_2 in the NO flow that is added continuously to the reactors. Both magnet valves and scrubbers are installed on a plate and connected at the bottom of the inlet (see Figure 3.1).

The main parts of the DUALER rack schematically represented in Figure 3.2 are:

Computer and the electrical control units: The computer is responsible for data acquisition. The operation of the flow controllers and magnet valves and the data collection of the detection is controlled by data cards (Data Translation,Inc DT 322 Multifunction Data Acquisition Board) that have an analog digital conversion rate of 200 kSA/s per channel. The power suppliers for the temperature sensor, relative humidity sensor, magnet valves and mass flow controllers are all installed in this unit.

Gas cylinders, mass flow controller, scrubbers and vacuum pump: The gas cylinders that are used during the flights are connected to the mass flow controllers operated by the computer and electrical control unit. The CO in the exhaust line is converted in CO_2 by means of a catalytic reaction taking place in a scrubber installed before the vacuum pump containing activated charcoal and Pt/Al pellets at T > 100°C. Additionally, there is a NO scrubber

between the NO flow controllers and the NO gas cylinder containing $FeSO_4$ to remove the NO_2 traces from NO, and a CO scrubber previous to the CO flow controllers containing charcoal/ iodine to remove iron and nickel carbonyls from CO which can interfere in the luminol reaction with NO_2. A vacuum pump connected to a pressure controller is used to regulate the pressure of the DUALER and sample the required air through the system.

NO_2 detector unit: The NO_2 detection is based on the chemiluminescence reaction of NO_2 with $5x10^{-4}$ M luminol solution taking place on the surface of a glass fibre filter. The photons released at wavelength range 400 to 500 nm are detected with a photodiode (Hamamatsu Si-1248) whose signal is amplified and converted to a voltage that is digitized and stored by a data acquisition system (Agilent Vee).

The inner view of the home made detectors can be seen in Figure 3.5. This unit consists of the detector body itself and the luminol box. The pressure of the DUALER is kept constant during the operation. Variations of the pressure of the system affect the luminol flow and the retention time of the NO_2 molecules in the detector therefore the sensitivity directly (see section 6.1.1). In the luminol box the peristaltic pump for the luminol flow is operating under the same pressure as the detector (Figure 3.6). Pressure differences between the detector and the luminol box, due to the irregularities in pressure regulation, may affect the luminol flow leading to in homogeneities in the wetness of the filter paper and results in instabilities in the detector response.

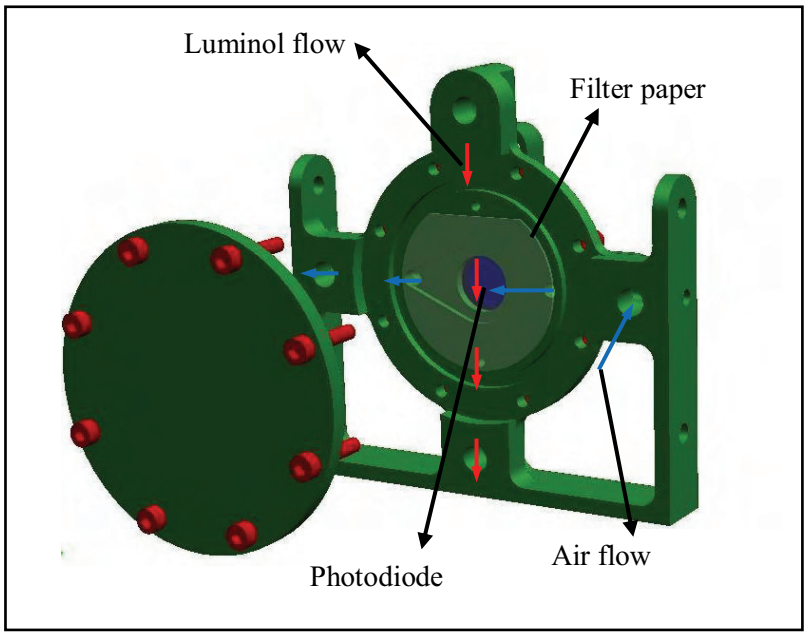

Figure 3.5 Inner view of the detector. The reaction zone (filter paper) and the photodiode are separated with a quartz glass.

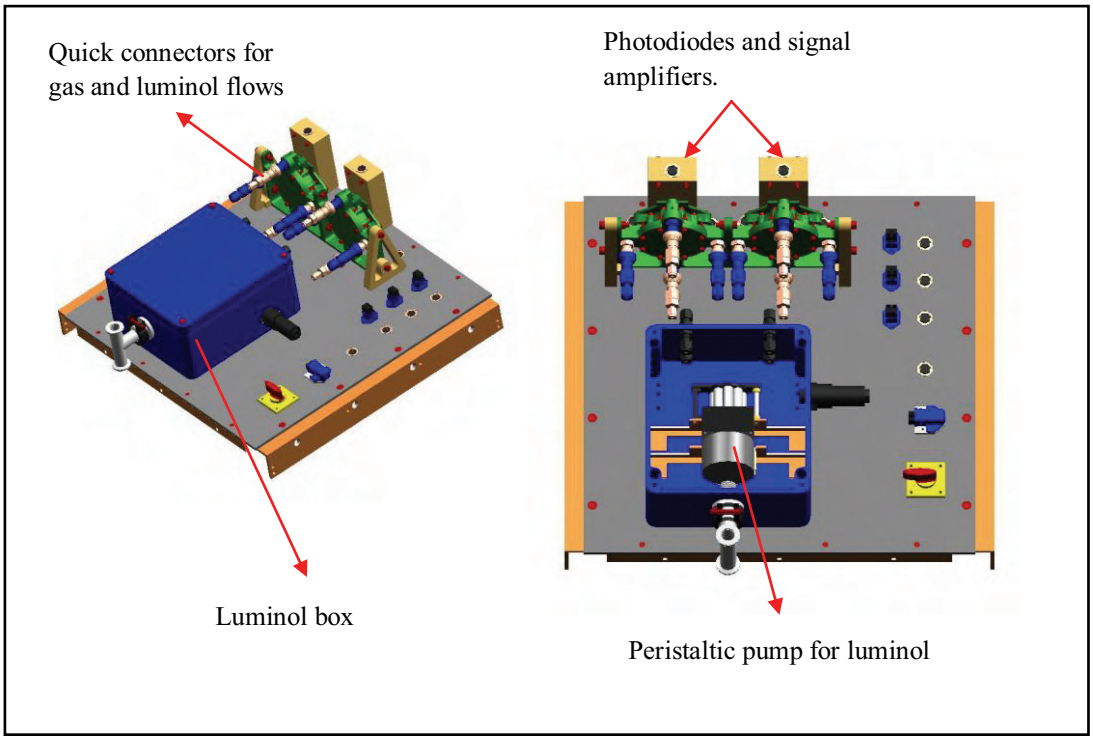

Figure 3.6 NO_2 detector unit. During the operation the detectors and the luminol box are kept at the same pressure.

3.1.2 Operation conditions of the DUALER

In the case of the IUP-UB DUALER the pressure at the pre-reactor nozzle is kept lower than the ambient pressure. The pressure in the pre-reactor nozzle is regulated with a pressure controller (Bronkhorst, Hi-Tec F 0004BI-IV-55-V), each reactor is connected to a Bronkhorst mass flow controller so modified that can operate with a pressure difference $\Delta P = 50$ mbar between the input and output , i.e pressure of the air sampled at the pressure nozzle and the pump.

The ambient air is mixed with NO and CO/N_2 as soon as it reaches the reactors. The reactors can be operated in the same or at opposite modes (Figure 3.7).Three way magnet valves operated by Agilent Vee software switch every 60 sec. the modes of the reactors (see section 1.4.4). In order to prevent pressure variations by switching the measurement modes and keep the mixing ratio the same in the detector, the same amount of N_2/CO is added at the second addition point.

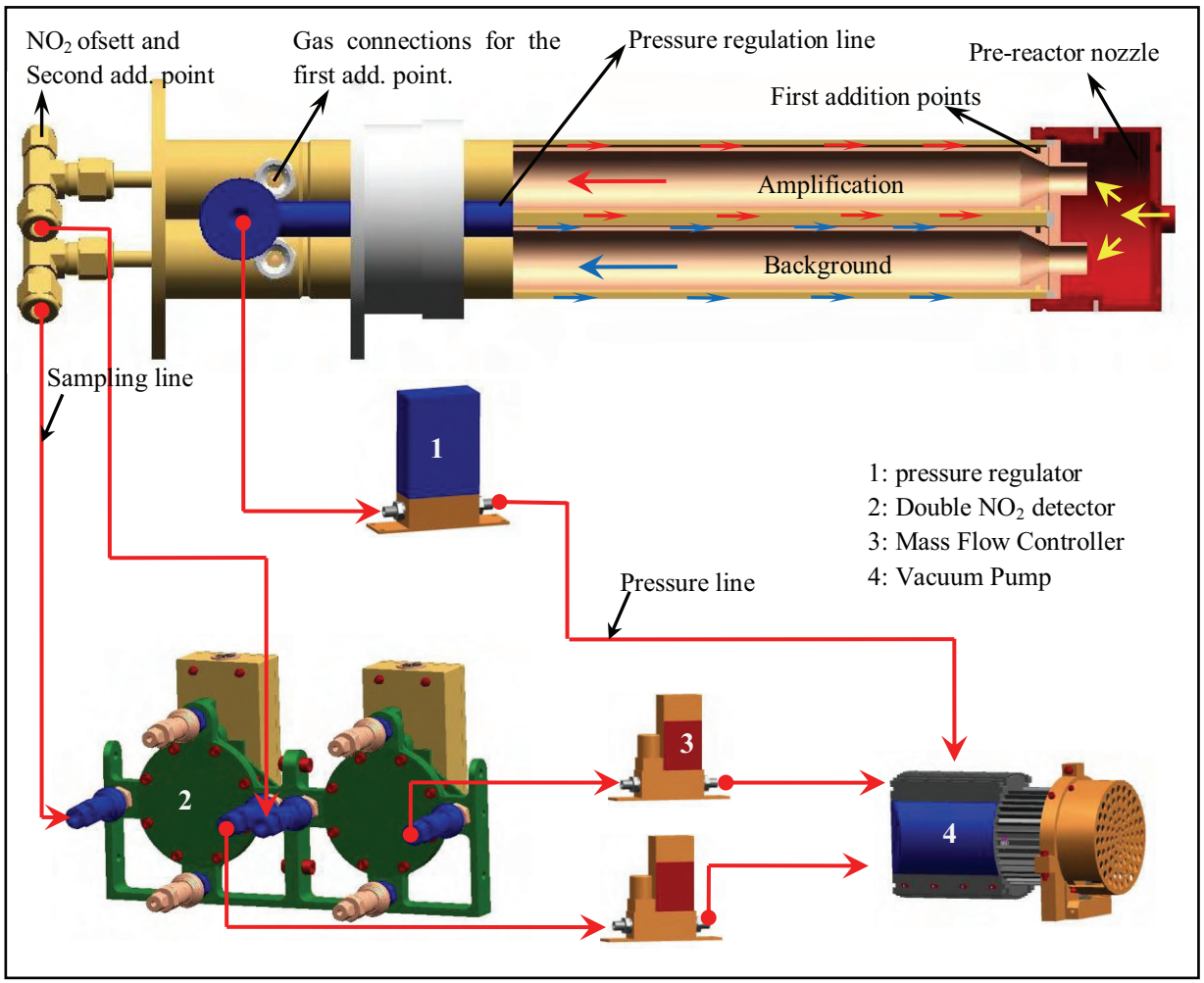

Figure 3.7 A cut view of the DUALER and schematic diagram of the main gas connections.

The DUALER is generally operated with %9 CO and 3 ppm NO.

Increasing CO mixing ratio increases the absolute value of CL (see section 1.4.4.2) but the mixing ratio has to remain lower than the explosion level. During the safety regulations of DLR-Falcon leading to limitations in the CO gas amount onboard, 7,4 % CO was added to the reactors during the AMMA flight measurements and corresponding calibrations.

NO mixing ratio around 4-5 ppm leads to a maximum absolute value of CL .The higher NO mixing ratios cause the loss reactions to dominate in the reactor and decrease of the absolute value of CL (see section 1.4.4.2). In addition, the increase of NO mixing ratio leads to a decrease in the absolute sensitivity of the NO_2 detector. The NO mixing ratio on board of DLR-Falcon is kept constant at 3 ppm.

During the AMMA flight measurements 20 ppb NO_2 was added as an offset to the detector. This mixing ratio was sufficient to have a linear response of the detectors due to the high mixing ratios of ozone contributing as NO_2 in the DUALER detector signal. In the laboratory studies the offset of the detectors was between 40-45 ppb considering the linear response of the detectors (see section 3.3.1).

3.2 Experiments under pressure controlled conditions

A calibration set up was designed and implemented in the laboratory for the characterization of reactors and detectors for airborne measurements. Aircraft measurements associated with temperature and pressure changes which can affect the performance of the instrumentation. The characterization procedures in the laboratory should simulate these variations. With this objective, the calibration unit was installed in a pressure chamber to simulate the pressure variations close to the flight conditions.

3.2.1 Pressure Chamber

The pressure chamber was used within this work to simulate pressures covering the range of the flight levels during airborne measurements. The pressure chamber is a metal cylinder whose lids are constructed from plexi-glas. The volume of the chamber is 0.2 m^3 with a inner diameter of 49.5 cm and a length of 105 cm. Along the chamber flanges are welded for the feed-through of data cables, gas lines, and electrical connections to the power suppliers of the instruments installed outside the chamber (see Figure 3.8). The chamber is evacuated with help of a vacuum pump and the pressure is regulated by using a MKS pressure regulator. Additionally, the absolute value of the pressure in the chamber is measured by a MKS barometer.

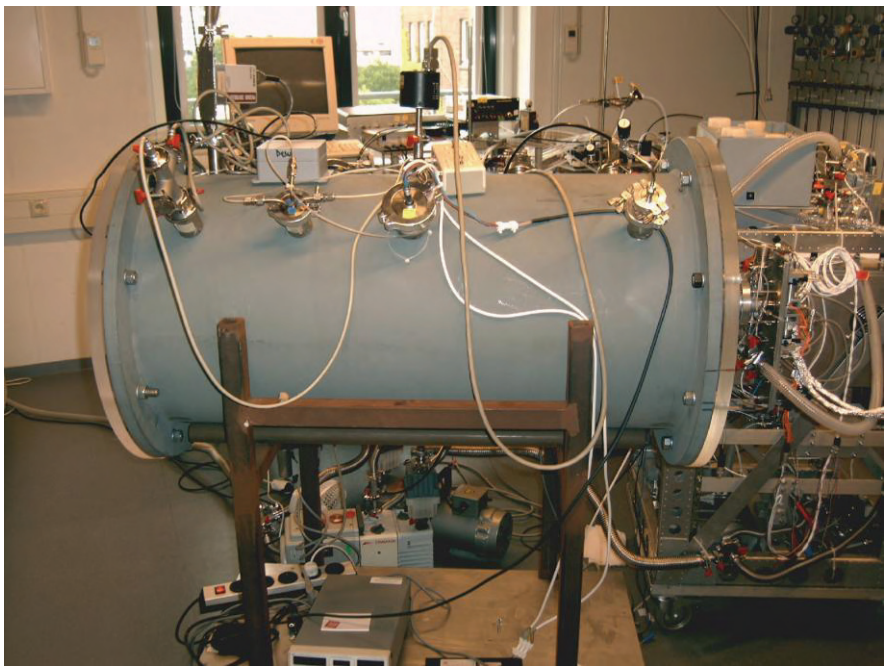

Figure 3.8 Pressure chamber with set up for the pressure characterization of the DUALER

The radical calibration source is installed inside the chamber. Radicals are produced by the photolysis of water at 184,9 nm in the presence of oxygen (Shultz et al., 1995). The water is mixed with the calibration air at a glass cell with the help of a peristaltic pump (Figure 3.9). Different water flows and consequently mixing ratios of water in the calibration air are obtained by varying the velocity of the pump. The water content in the sample air is calculated from the dew point temperature of the sample gas that is measured with a dew point sensor (Vaisala DMP 248) installed inside the chamber.

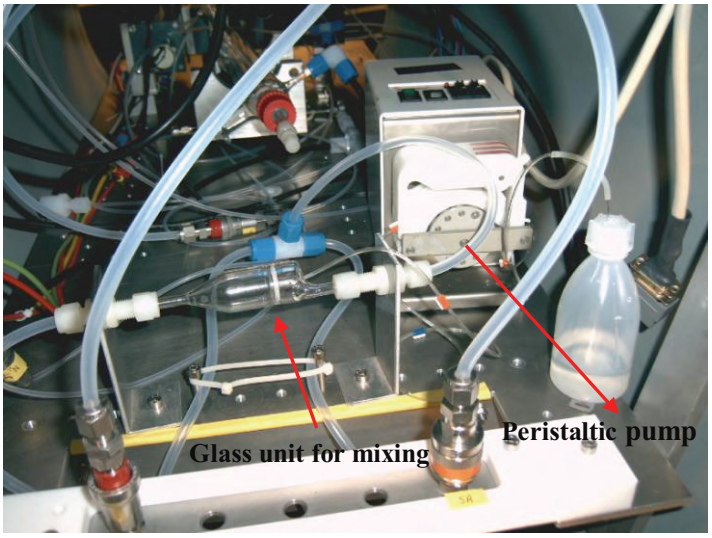

Figure 3.9 Detailed view of the humidifier of the radical source.

The humidified air goes to the photolysis zone where the radical production takes place (see section 3.3.2). Before the entrance to the photolysis zone CO is added to the calibration air to convert the OH, which is the photolysis product of water to HO_2 (see section 3.3.2).

The IUP-UB calibration source has been described in detail elsewhere (Reichert et al., 2003). The radical source represented in Figure 3.10, and consists of following components.

Hg-Lamp (Pen-Ray lamp): The 184,9 nm emission line of the mercury vapor is used for the photolysis of H_2O (see section 3.3.2). The mercury lamp is installed in a block that is kept at a constant temperature around 40°C to prevent variations in the lamp profile caused by temperature changes in the ambient air. The lamp spectrum depends on the age and the operation conditions of the lamp (Hofzumahaus et al., 1997) (see section 3.3.2.1: Determination of effective absorption cross section of O_2).

Cylindrical Lense: This lense is used to parallelize the light beam from the lamp through the absorption and the photolysis cells.

Absorption cell: The absorption cell is the zone between the Hg lamp and the photolysis zone delimited by quartz glass windows. The reduction of the intensity of the light is achieved by a use of gas filter which is a mixture of N_2O and N_2 controlled by mass flow controllers, through the absorption cell. The N_2O has at 184,9 nm a constant absorption coefficient $14{,}05 \times 10^{-20} cm^2$ $molecule^{-1}$, (Cantrell et al., 1997) that enables to reduce the maximum light intensity 90%. Different radical mixing ratios are generated by changing the light intensity at the absorption cell at constant mixing ratio of water in the calibration air.

Photolysis zone: In the photolysis zone the photolysis reactions take place. The photolysis zone is a cylindrical quartz tube with 16 mm inner diameter and 20 cm length.

Interference Filter: This filter intends the specific transmission for the wavelength of interest 184.9 nm. The peak wavelength of the filter is 184.9 nm $\pm$2.5 nm and the transmittance at this wavelength is 12.5 %.

Photomultiplier: The detection unit consists of a photomultiplier Hamamatsu 1259 with a MgF_2 window which enables a spectral response between 115 and 195 nm.

All the optical paths in the source are purged with N_2 to avoid ambient air disturbances during the calibration.

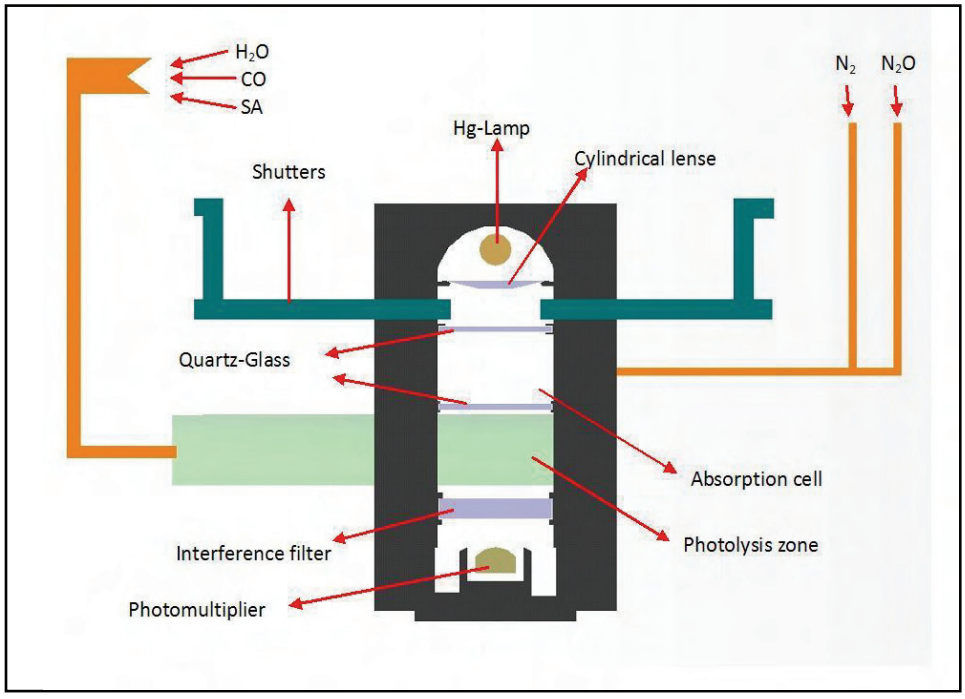

Figure 3.10 Schematic diagram of the radical source installed in the chamber

3.2.2 Installation of DUALER to Pressure Chamber

The DUALER inlet is installed to the pressure chamber with the aircraft pylon used for the airborne measurements. An adapter was constructed for the adaption of the pylon to the Plexiglas window of the pressure chamber. A block between the radical source and the aircraft pylon is placed to assure that the DUALER is sucking from the middle of the source (Figure 3.11 and 3.12), i.e., the sampling occurs always at the same position in the flow profile which warranties the reproducibility of the radical mixing ratios introduced in the DUALER inlet.

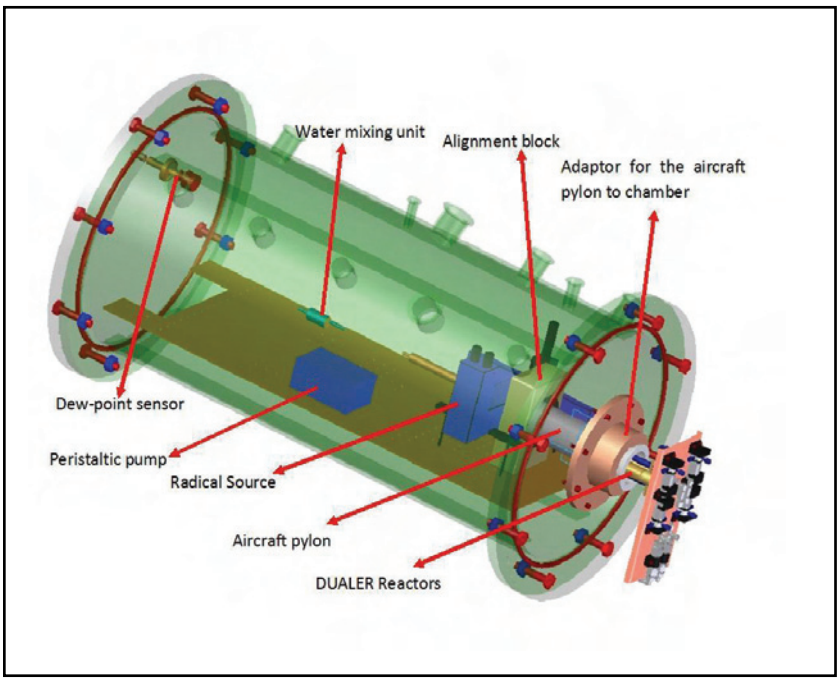

Figure 3.11 Schematic diagram of the DUALER inlet as connected to the pressure chamber for calibrations.

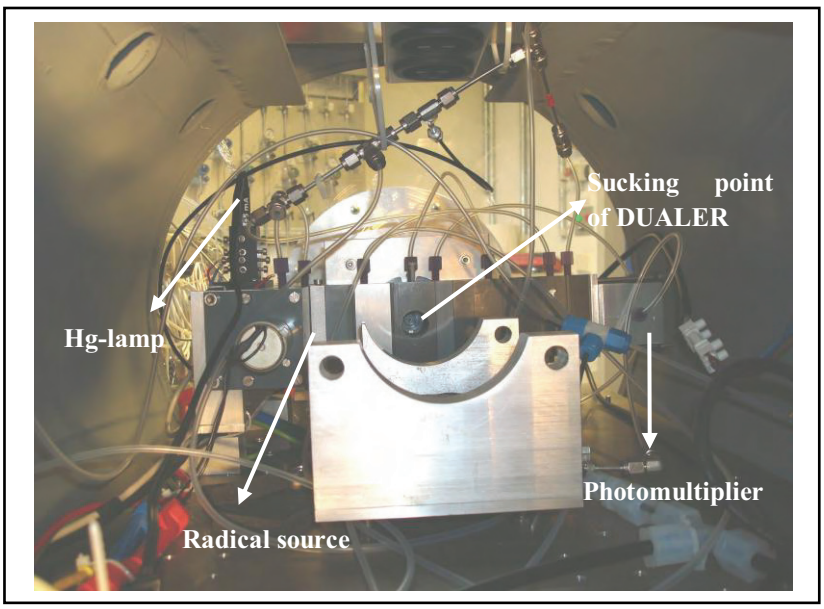

Figure 3.12 Inside view of the chamber. The photolysis unit is removed for clarity.

For the experiments performed with a single reactor (see section 6.1.2), the connection to the pressure chamber proceeds in a similar way (Figure 3.13).

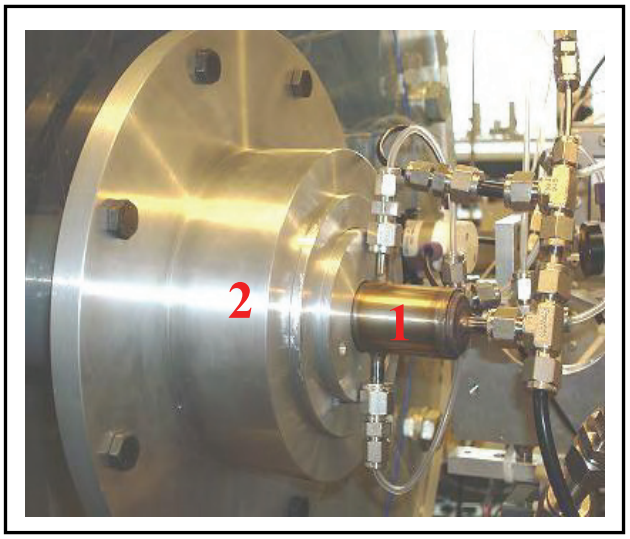

Figure 3.13 Single reactor adapted to the chamber 1:single reactor ; 2: adaptor unit for different reactors

3.3 Calibration Procedures

The sensitivity of the DUALER instrument relies both on the efficiency of the conversion of radicals into NO_2 at the reactor, i.e., the chain length (CL), and on the performance of the NO_2 detector. The calibration procedure must therefore comprise regular CL and NO_2 calibrations.

The calibration procedures of the DUALER are similar to those for the IUP-PERCA ground based instrument (Reichert et al., [2003]).The only difference is that the instrumentation of the calibration experiments is installed inside the presssure chamber as explained in the previous sections.

3.3.1 NO_2 Calibrations

The NO_2 response of the detectors is calibrated regularly by adding different mixing ratios from calibrated gas cylinders. The response of the detector to NO_2 is quadratic and 2 molecules of NO_2 are believed to be involved in the chemiluminescent reaction with luminol. (Wendel et al., 1983; Cantrell et al., 1993 a). However responses are linear to a very good approximation above 3-5 ppb in the absence of NO in the detector. (Kelly et al., 1990; Clemitshaw et al., 1997).

CO has no measurable effect on the detector response up to 10%. In contrast the NO_2 sensitivity decreases by a factor of approximately 2 in the presence of 3 ppm NO and becomes non-linear below about 25 ppb NO_2 (Hastie et al., 1991; Clemitshaw et al., 1997). To ensure that all measurements and calibrations are made in the linear region, an offset flow of NO_2 above 25 ppb is added continuously to the detectors. A NO_2 calibration of the detectors of IUP-UB DUALER is shown exemplary in Figure 3.14.

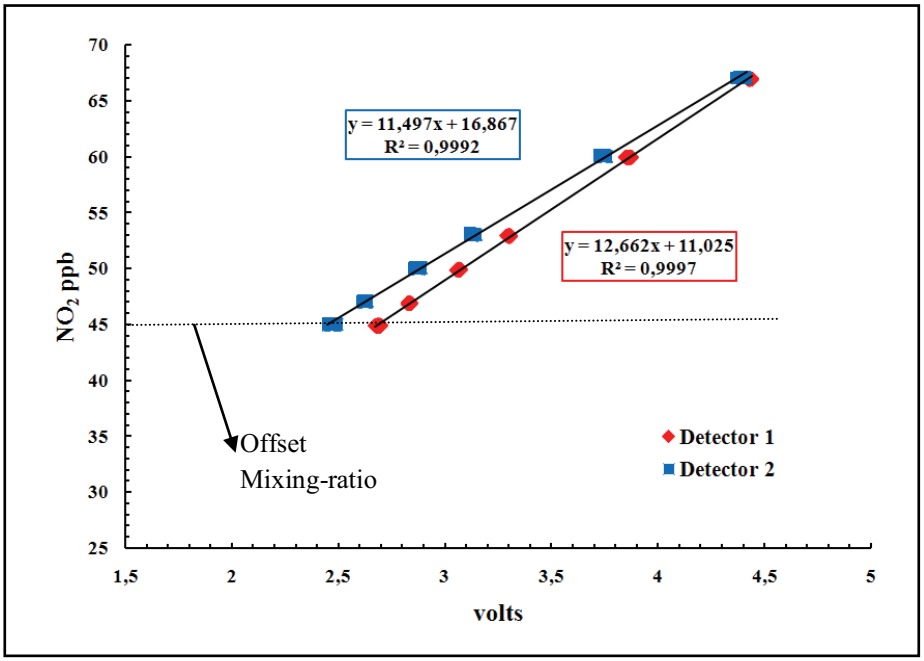

Figure 3.14 NO_2 detector response of two detectors of DUALER

3.3.2 Chain Length Determination: HO_2 calibration

The HO_2 calibration of the DUALER is based on the production of radicals from the UV photolysis of H_2O at 184.9 nm (Shultz et al., 1995). A known water-air mixture is photolysed by reaction (3.1) with a low-pressure Hg-Lamp which intensity is attenuated by varying the N_2O/N_2 ratio in the absorption cell (see section 3.2.1)

$$H_2O + h\nu(\lambda = 184.9nm) \rightarrow H + OH \tag{3.1}$$

The H atoms react with oxygen that has a known mixing ratio in the sample gas;

$$H + O_2 + M \rightarrow HO_2 + M \tag{1.42}$$

The OH from reaction (3.1) reacts with CO that is added continuously to the photolysis cell to convert all the products of the photolysis of H_2O to HO_2. Instead of CO, CH_4 can be added to the photolysis cell to get the same mixing ratios of HO_2 as CH_3O_2;

$$CO + OH \xrightarrow{O_2} HO_2 + CO_2 \tag{1.26}$$

$$CH_4 + OH \rightarrow CH_3O + H_2O \tag{1.28}$$

$$CH_3O + O_2 + M \rightarrow CH_3O_2 + M \tag{1.29}$$

At the same time the photolysis of oxygen leads to ozone production,

$$O_2 + h\nu(\lambda = 184,9\,nm) \rightarrow O(^3P) + O(^3P) \tag{3.2}$$

$$O_2 + O(^3P) \rightarrow O_3 \tag{1.16}$$

The change of the concentrations of HO_2 and O_3 can be expressed like this;

$$\frac{\partial HO_2}{\partial t} = 2 * \Theta^{184.9nm} * \sigma_{H_2O}^{184.9nm} * [H_2O] \tag{3.3}$$

$$\frac{\partial O_3}{\partial t} = 2 * \Theta^{184.9nm} * \sigma_{O_2}^{184.9nm} * [O_2] \tag{3.4}$$

The photon flux $\Theta^{184.9nm}$ is the same for equation (3.3) and (3.4). As there is neither HO_2 nor O_3 at the beginning of the photolysis, after integration over time of photolysis, it can be written:

$$[HO_2] = \frac{\sigma_{H_2O}^{184.9nm} * [H_2O]}{\sigma_{O_2}^{184.9nm} * [O_2]} * [O_3] \tag{3.5}$$

Provided that the H_2O and O_3 mixing ratios are known the HO_2 mixing ratios can be calculated using the equation (3.5). The absorption cross section for H_2O at 184.9 nm is used

as $7.14*10^{-20}$ cm^2 $molecule^{-1}$ (Cantrell et al., 1997; Hofzumahaus et al., 1997). The water mixing ratio is calculated from the measurements of a dew point sensor. The mixing ratio of the oxygen is known from the specifications of a standard gas cylinder of synthetic air. The absorption cross section of oxygen and the ozone mixing ratio are determined experimentally for each calibration condition.

3.3.2.1 Determination of effective absorption cross section of oxygen

The O_2 absorption spectrum in the Schumann-Runge bands is highly structured near the 184.9 nm (Yoshino et al., 1983; Lanzendorf et al., 1997), (Figure 3.15). As the emission spectrum of the mercury lamp, which is a function of O_2 column, differs according to the operation conditions, temperature, time and position of the lamp (Creasey et al., 2000), the effective absorption cross section of O_2 might vary significantly according to the features of the experimental set up and must be determined for each set up (Hofzumahaus et al.,1997).

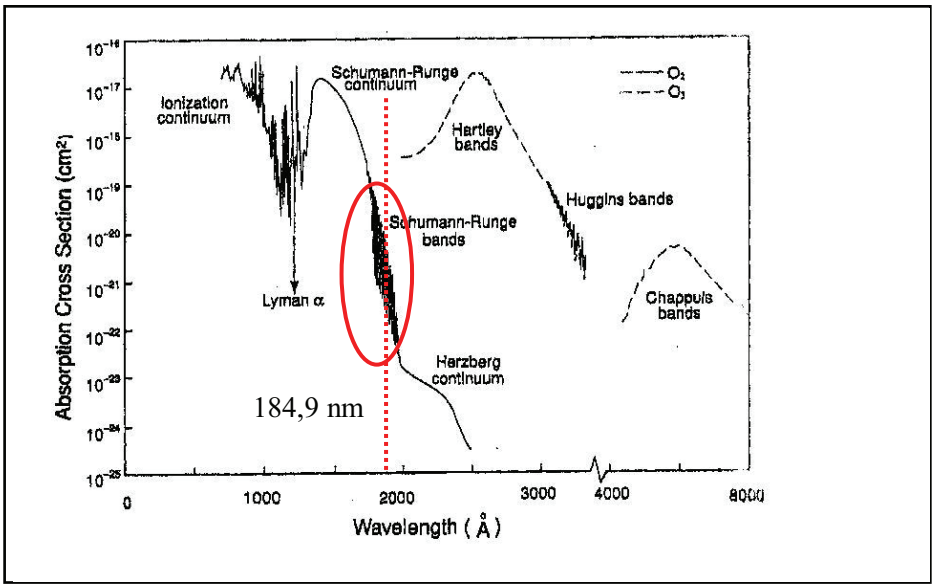

Figure 3.15 Absorption Cross section of ozone and molecular oxygen in the ultraviolet spectral region (Brasseur and Solomon [1986], Vigroux [1953], and Griggs [1968]).The absorption features around 184,9 nm is highlighted in red.

For the determination of the effective absorption cross section different concentrations of oxygen are generated by mixing of N_2 and synthetic air, through the photolysis zone. The apparent absorption cross section is determined for different oxygen columns using the Beer-Lambert law:

$$\sigma_{O_2,app}(x) = (1/x) * \ln(I_0 / I(x)) \tag{3.6}$$

This apparent absorption cross section results from the integration of the effective absorption cross section through an oxygen column x. The dependency of the effective cross section on the oxygen column can be expressed as following;

$$\int_0^x \sigma_{O_2\,eff}(x)dx = \ln(I_0 / I(x)) = x * \sigma_{O_2\,app}(x) \tag{3.7}$$

$$\sigma_{O_2\,eff}(x) = \frac{d[\ln(I_0 / I(x))]}{dx} = -d[\ln(x)]/dx \tag{3.8}$$

$$\sigma_{O_2\,eff}(x) = \frac{d[x * \sigma_{O_2\,app}(x)]}{dx} \tag{3.9}$$

$$\sigma_{O_2\,eff}(x) = \sigma_{O_2\,app}(x) + \frac{d[\sigma_{O_2\,app}(x)]}{dx} * x \tag{3.10}$$

In the equations (3.6), (3.7), (3.8), (3.9), (3.10) x is the oxygen column, I_0 is the incident light intensity measured when only N_2 is in photolysis zone and I(x) is the light intensity measured after the interaction of the incident light with the oxygen column. The $\sigma_{O_2app}(x)$ and $\sigma_{O_2\,eff}(x)$ can only be equal when the slope ($\frac{d[\sigma_{O_2\,app}(x)]}{dx}$) of the plot in Figure 3.16 is zero (Creasey et al.2000). The decrease of σ_{O_2app} and $\sigma_{O_2\,eff}$ with the oxygen column determined during this work at 1000 ± 10 mbar is depicted in Figure 3.16.
The variation of the O_2 effective cross section with pressure is investigated within the present work (see section 6.1.2)

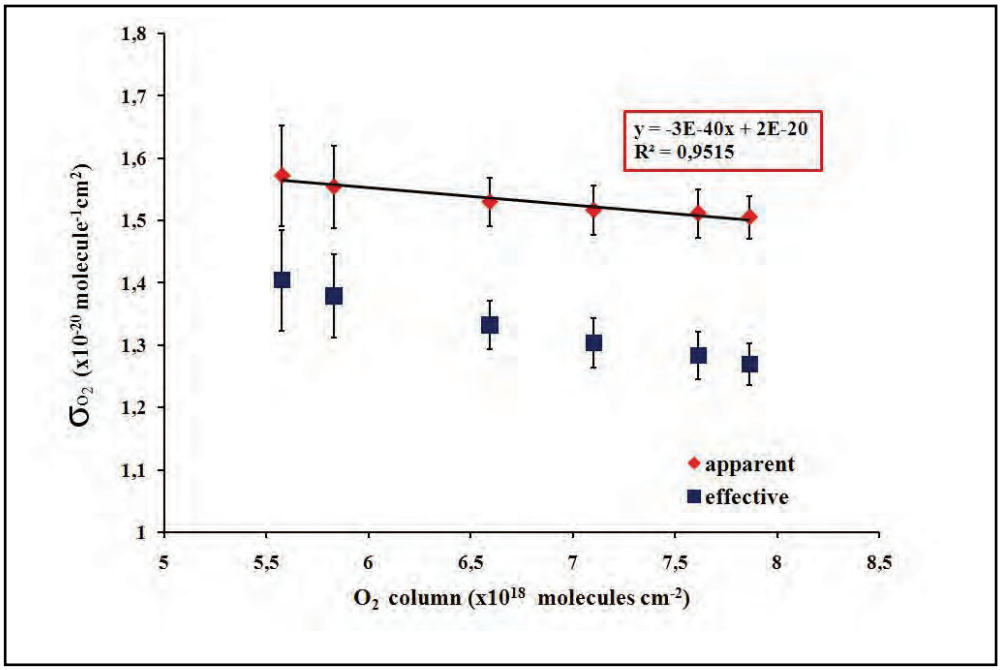

Figure 3.16 Variation of O_2 the absorption cross section with oxygen column at 184.9 nm. ($d[\sigma_{O_2\,app}(x)]/dx = 3E\text{-}40$) determined experimentally for the IUP-UB source at 1000 mbar.

3.3.2.2 Determination of the ozone production of the radical source

During the HO_2 calibration, direct measurement of the small O_3 variations (0,2-0,7 ppb) between single points of the HO_2 calibration from the background signal of the NO_2 luminol detector would require high accuracy. The determination of the ozone mixing ratio has therefore to be carried out separately. By accurately measuring the light emitted through the photolysis zone using a photomultiplier, the corresponding amount of O_3 produced can be calculated. The ratio between produced ozone and a reference ozone mixing ratio, i.e the maximum ozone mixing ratio produced $[O_3]_{max}$ has to be equal to the ratio between the intensity of light and a reference light intensity, i.e. the light intensity detected at maximum production of ozone I_{max},

$$\frac{O_{3\ detected}}{O_{3\ max}} = \frac{I_{detected}}{I_{max}} \tag{3.11}$$

The plot in figure 3.17 shows the linear relationship between ozone and light intensity ratios determined experimentally for the IUP radical source within this work. The reference measurements are always done at maximum possible ozone mixing ratio, since the accuracy of the NO_2 detector is the best for these mixing ratios.

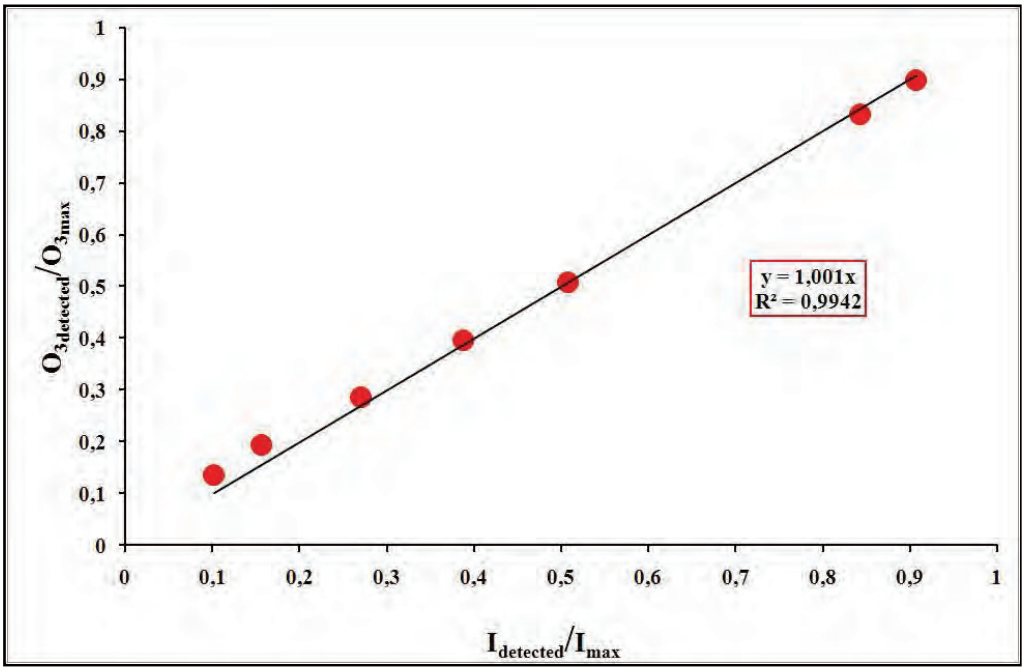

Figure 3.17 Experimental relationship between $\frac{O_{3_{detected}}}{O_{3_{max}}}$ and $\frac{I_{detected}}{I_{max}}$ ratios.

Consequently, at each HO_2 calibration point the ozone mixing ratios produced can be calculated from;

$$O_3 = O_{3\ max} * \frac{I_{detected}}{I_{max}} \tag{3.12}$$

3.4 Error Analysis

The uncertainty of the DUALER measurements is directly related to the uncertainties of the calibration procedures. The aim of the calibrations is to determine accurately the chain length. The error of the CL depends on the error of NO_2 detector response and the error of the $[HO_2]$ production procedure.

$$CL = \frac{[\Delta NO_2]}{[HO_2]} \tag{3.13}$$

ΔNO_2 is the difference between the background and amplification response of the detector in mixing ratio. HO_2 is the amount of radicals produced during the calibration and calculated according to equation (3.5) (see section 3.3.2). The error propagation of the chain length can be expressed like:

$$\sigma_{CL}^2 = \sigma_{[\Delta NO_2]}^2 \left(\frac{\partial CL}{\partial [\Delta NO_2]} \right)^2 + \sigma_{[HO_2]}^2 \left(\frac{\partial CL}{\partial [HO_2]} \right)^2 \tag{3.14}$$

Thus:

$$\frac{\sigma_{CL}}{CL} = \sqrt{\frac{\sigma_{[\Delta NO_2]}^2}{[\Delta NO_2]^2} + \frac{\sigma_{[HO_2]}^2}{[HO_2]^2}} \tag{3.15}$$

The relative error of the CL can be determined from the relative error of ΔNO_2 and the relative error of HO_2 by using the equation (3.15).

The determination of the ΔNO_2 uncertainty requires the uncertainty in the detector sensitivity and the uncertainty in the difference (ΔV) between background and signal mode. As $[NO_2] = a \times V + b$ and V is the detector response in volts:

$$\Delta NO_2 = a * V_{signal} + b - a * V_{background} + b = a * (V_{signal} - V_{background}) = a * \Delta V \tag{3.16}$$

The error propagation of $[\Delta NO_2]$ can be written as;

$$\frac{\sigma_{[\Delta NO_2]}}{[\Delta NO_2]} = \sqrt{\left(\frac{\sigma_{\Delta V}}{\Delta V} \right)^2 + \left(\frac{\sigma_a}{a} \right)^2} \tag{3.17}$$

$\sigma_{\Delta V}$ is a result of the standard deviations of the detector response as a voltage. The σ_a is the error of the regression line obtained with the least square fit method (Appendix 1). σ_a depends on the error in the concentration of the NO_2 gas cylinder, the error in the flows used to obtain different NO_2 dilutions during the calibration, and the error of the response of the detector as voltage. The relative error of the difference of the modes as voltage is 0,2 %; for

the regression slope "a" the relative error is around 3 % and depends strongly on the stability of the NO_2 offset response during the calibration (Appendix1). The relative error of $[\Delta NO_2]$ varies consequently within 3%.

According to equation (3.5) the determination of the relative error of the HO_2 concentrations Eq (3.18) depends on the uncertainties in mixing ratio of water in the sample gas, the determination of the effective absorption cross section and of the ozone mixing ratios.

$$\frac{\sigma_{HO_2}}{[HO_2]} = \sqrt{\left(\frac{\sigma_{\sigma_{O_2}^{184.9nm}}}{\sigma_{O_2}^{184.9nm}}\right)^2 + \left(\frac{\sigma_{\sigma_{H_2O}^{184.9nm}}}{\sigma_{H_2O}^{184.9nm}}\right)^2 + \left(\frac{\sigma_{[H_2O]}}{[H_2O]}\right)^2 + \left(\frac{\sigma_{[O_3]}}{[O_3]}\right)^2} \qquad (3.18)$$

Instrumental precision of the dew point sensor is $\pm 2°C$ in the interval that the calibrations are performed. According to this value the mixing ratios calculated from the dew point temperature have a relative error of 5%-6%.

Determination of the O_2 effective absorption cross section which depends on the experimental set up (see section 3.3.2.1), used for the present investigation has a relative error around 5%. The relative error of the O_2 effective absorption cross section experimentally determined within this work in a calibration series is plotted exemplary in Figure 3.18.

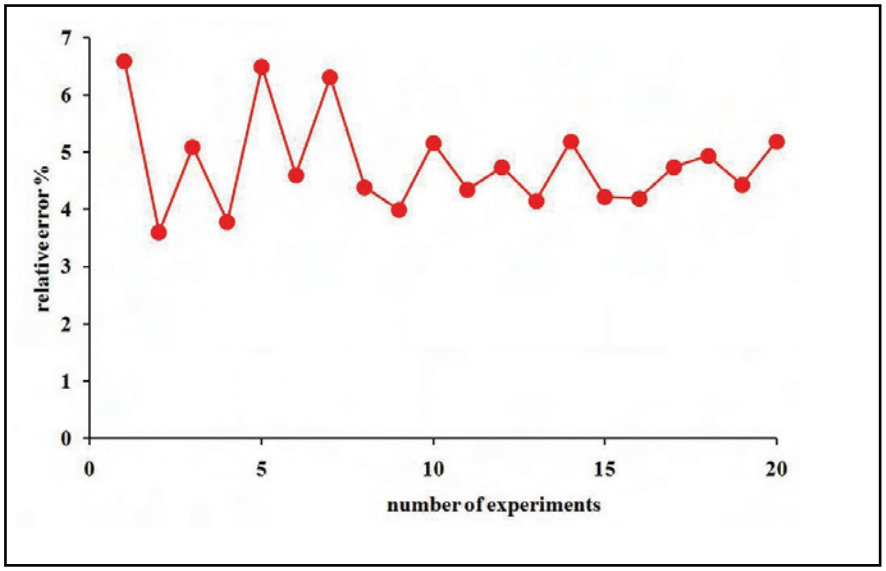

Figure 3.18 Relative error of $\sigma_{O_2 eff}$ determination determined within this work.

The accuracy of the determination of the ozone depends on the NO_2 detection, the lamp operation conditions and the instrumental error of the photomultiplier. The error propagation results in:

$$\frac{\sigma_{[O_3]}}{[O_3]} = \sqrt{\left(\frac{\sigma_a}{a}\right)^2 + \left(\frac{\sigma_{\Delta V_{[O_3]max}}}{\Delta V_{[O_3]max}}\right)^2 + \left(\frac{\sigma_{I_{max}}}{I_{max}}\right)^2 + \left(\frac{\sigma_{I_{detected}}}{I_{detected}}\right)^2} \qquad (3.19)$$

The equation (3.19) is calculated replacing $O_{3\ max}$ in equation (3.12) by ($a * \Delta V_{[O_3]max}$) of; where $\Delta V_{[O_3]max}$ is the response difference in voltage of the NO_2 detector, at maximum ozone production and at no ozone production. The contribution of all the error sources leads to a relative error is around 3% for the ozone mixing ratios.

The water absorption cross section is taken from the literature value $(7{,}14 \pm 0.1) \times 10^{-20}$ (Cantrell et al., 1997).

All these relative errors results in a 10-15% relative error for $[HO_2]$ determination.

As a consequence, the relative error of the CL varies between 10% and 16% for the calibrations performed within this work.

3.5 Installation and operation of DUALER at DLR-Falcon

The DUALER was installed on board the DLR-Falcon for the international measurement campaign AMMA.

The DLR-Falcon is a scientific research aircraft (Figure 3.19) that is operated by German Aerospace Centre (DLR). The mechanical and aerodynamically robustness of DLR-Falcon make it an ideal research aircraft even under extreme situations like thunderstorm research, or measurements in contrail of other aircrafts. The following table summarises the technical features of DLR-Falcon. (http://www.dlr.de/fb/op)

Overall length	17,2 m
Wingspan	16,3 m
Number of seats	2+10
Max takeoff weight	13,2 t
Engines	Garret TFE 731-
Max altitude	13,9 km
Initial climb altitude	11,9 km
Max range	3700 km
Max endurance	5:30 h
Max Payload	(with max fuel) 1.1 t
Max fuel	4,0 t
Max speed	917 km/h
Min clean speed	296 km/h

Table 3.1 Technical features of DLR-Falcon aircraft

Figure 3.19 DLR-Falcon during the AMMA campaign in the comparison flight on 16.08.2006. The position of the DUALER inlet is highlighted.

The inlet of the DUALER is installed through the aircraft wall with a special adaptor supplied by the DLR (Figure 3.20).

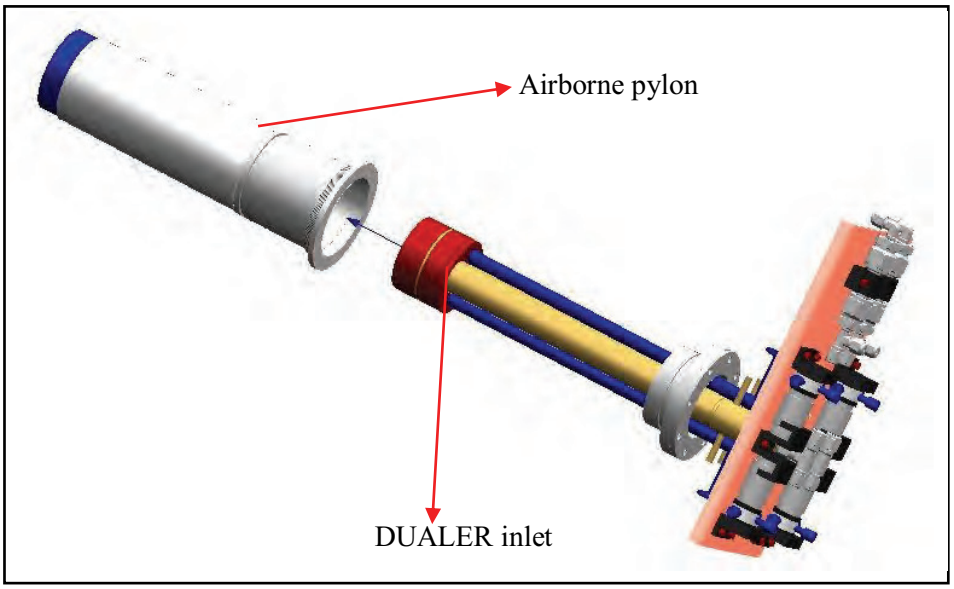

Figure 3.20 Airborne adaptor for the DUALER inlet

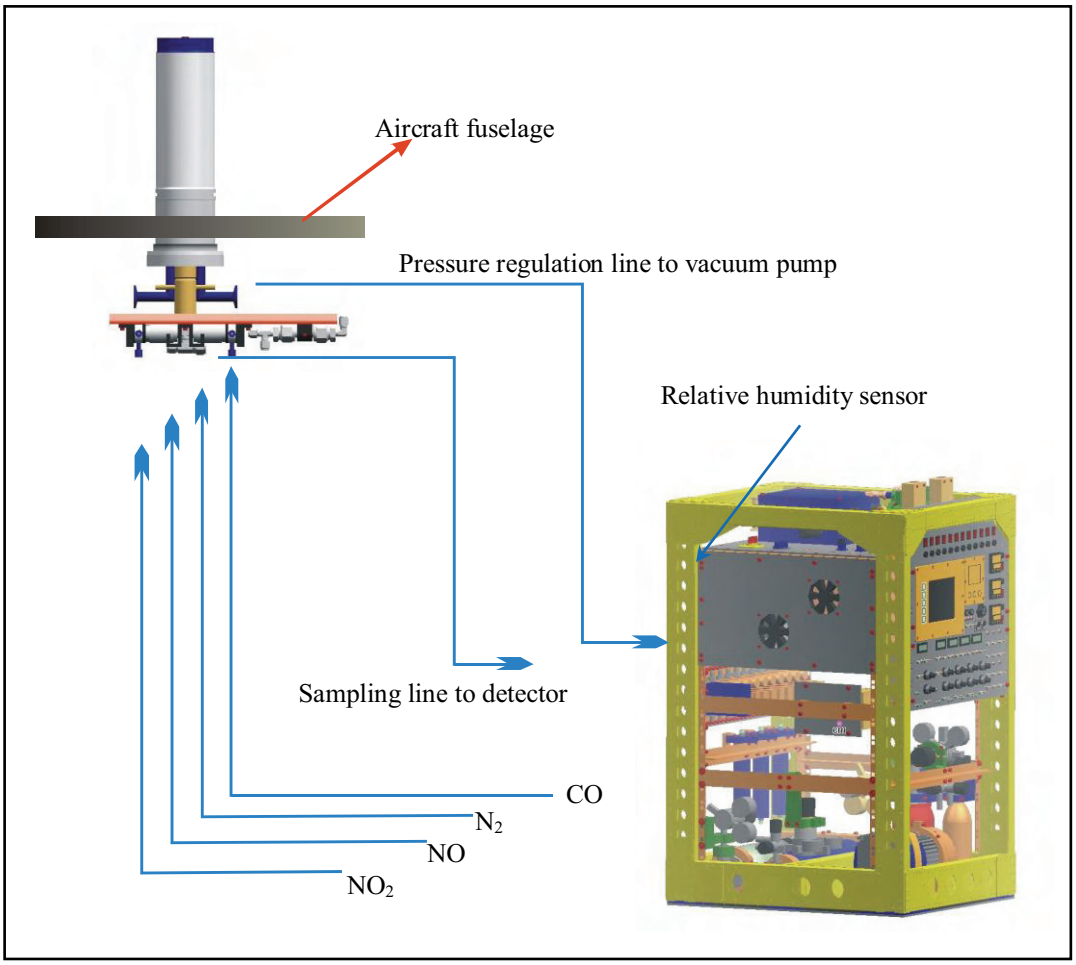

Figure 3.21 Schematic representation of the DUALER deployment onboard of DLR-Falcon.

The gas supply and the pressure regulation of the DUALER are operated with the rack (see Figure 3.21). Due to the safety restrictions in the total volume of CO allowed on board the DLR-Falcon 7.4 % CO and 3 ppm NO were added to a sampling flow rate at each reactor of 0,5 $sLmin^{-1}$. A $NO_{2\ offset}$ of 20 ppb was added to the detectors in order to assure their linear response at low ambient O_3 mixing ratios. The DUALER pressure was kept at 200 mbar to avoid the signal instabilities with changing the flight levels during the measurements.

4 Modelling Studies

The modelling study of this work aims to simulate the amplification factor for different pressure conditions, wall losses and different concentrations of the reagent gasses (CO and NO) of the PERCA. A chemical box model was developed within this work based on the fourth order Runge-Kutta (RK4) numerical analysis method by programming with Matlab 7.0.

4.1 Fourth order Runge-Kutta method

The differential equations representing the production and consumption rates of the reactions can be solved by differencing the equation by numerical solutions. The fourth order Runge-Kutta method simulates the accuracy of the Taylor series method of order N=4 (Mathews, J.H., Fink, K.K., 2004). The method is based on computing y_{k+1} as follows for $\frac{dy(t)}{dt} = f(t, y(t)) \;\; y(0) = y_0$;

$$y_{i+1} = y_i + w_1 k_1 + w_2 k_2 + w_3 k_3 + w_4 k_4 \tag{4.1}$$

Where k_1, k_2, k_3, and k_4 have the form;

$$\begin{aligned} k_1 &= \Delta t\, f(t_i, y_i) \\ k_2 &= \Delta t\, f(t_i + a_1 \Delta t, y_i + b_1 k_1) \\ k_3 &= \Delta t\, f(t_i + a_2 \Delta t, y_i + b_2 k_1 + b_3 k_2) \\ k_4 &= \Delta t\, f(t_i + a_3 \Delta t, y_i + b_4 k_1 + b_5 k_2 + b_6 k_3) \end{aligned} \tag{4.2}$$

by matching the coefficients with those of the Taylor series method of order N=4 , Runge and Kutta (Carl Runge and Martin Wilhelm Kutta) were able to obtain a system of equations;

$$k_1 = \Delta t\, f(t_i, y_i) \tag{4.3}$$

$$k_2 = \Delta t f(t_i + \frac{1}{2}\Delta t, y_i + \frac{1}{2} k_1) \tag{4.4}$$

$$k_3 = \Delta t f(t_i + \frac{1}{2}\Delta t, y_i + \frac{1}{2} k_2) \tag{4.5}$$

$$k_4 = \Delta t f(t_i + \Delta t, y_i + k_3) \tag{4.6}$$

$$y_{i+1} = y_i + \frac{1}{6}(k_1 + 2k_2 + 2k_3 + k_4) \tag{4.7}$$

In the modelling algorithm, the change of the concentration of the molecules are calculated with the use of the equations (4.3),(4.4),(4.5),(4.6),(4.7).

The implementation of this numerical method for the reaction kinetics of a molecule 'A' can be written like this;

$$C + B \rightarrow A \tag{4.8}$$

$$\frac{d[A]}{dt} = k_{BC}[B][C] \qquad k_{BC} : \text{rate constant of the reaction} \tag{4.9}$$

$$\frac{d[B]}{dt} = -k_{BC}[B][C] \tag{4.10}$$

$$\frac{d[C]}{dt} = -k_{BC}[B][C] \tag{4.11}$$

$\frac{d[A]}{dt} = F(t,\ A(B(t),C(t),k_{BC}))$, $\frac{d[B]}{dt} = Z(t,\ B(B(t),C(t),\ k_{BC}))$, $\frac{d[C]}{dt} = Z(t,C(C(t),B(t),\ k_{BC}))$;

Initial value of the concentrations are A_0, B_0, C_0.

$$A1 = \Delta t\, F(B_0, C_0, k_{BC}) \qquad B1 = \Delta t\, Z(B_0, C_0, k_{BC}) \qquad C1 = \Delta t\, Z(B_0, C_0, k_{BC})$$
$$A2 = \Delta t\, F(B_0 + 0,5 * B1, C_0 + 0,5 * C1, k_{BC})$$
$$B2 = \Delta t\, Z(B_0 + 0,5 * B1, C_0 + 0,5 * C1, k_{BC})$$
$$C2 = \Delta t\, Z(B_0 + 0,5 * B1, C_0 + 0,5 * C1, k_{BC})$$
$$A3 = \Delta t\, F(B_0 + 0,5 * B2, C_0 + 0,5 * C2, k_{BC})$$
$$B3 = \Delta t\, Z(B_0 + 0,5 * B2, C_0 + 0,5 * C2, k_{BC})$$
$$C3 = \Delta t\, Z(B_0 + 0,5 * B2, C_0 + 0,5 * C2, k_{BC})$$
$$A4 = \Delta t\, F(B_0 + B3, C_0 + C2, k_{BC})$$
$$B4 = \Delta t\, Z(B_0 + B3, C_0 + C3, k_{BC})$$
$$C4 = \Delta t\, Z(B_0 + B3, C_0 + C3, k_{BC})$$

$$A_1 = (A1 + 2 * A2 + 2 * A3 + A4) / 6$$
$$B_1 = (B1 + 2 * B2 + 2 * B3 + A4) / 6$$
$$C_1 = (C1 + 2 * C2 + 2 * C3 + C4) / 6$$

The change of each concentration by time can be calculated in the same manner with the determination of $A_{1....n}$, $B_{1....n}$,and $C_{1....n}$. The algorithm code of the program is in Appendix 2.

4.2 Description of the chemical box model

The model simulates the amplification and terminating reactions in the PERCA technique and determines the CL at constant temperature and for different pressure values and mixing ratios of NO and CO. The medium for the simulations is considered as a closed box with a volume V.

The chemical reactions and the rate constants of the reactions used for the simulations are in Table.4.1 presented.

Reaction	**Low pressure limit** $k_0(T) = k_0^{300}(T/300)^{-n}$		**High-pressure limit** $k_\infty(T) = k_\infty^{300}(T/300)^{-m}$		**Rate constants for Bimolecular reactions at 298 K**
	k_0^{300}	**n**	k_∞^{300}	**m**	
$NO + OH \xrightarrow{M} HONO$	7,1E-31	2,6	3,6E-11	0,1	
$NO_2 + OH \xrightarrow{M} HONO_2$	2E-30	3	2,5E-11	0	
$NO_2 + HO_2 \xrightarrow{M} HO_2NO_2$	1,8 E-31	3,2	4,7 E-12	1,4	
$HO_2NO_2 \xrightarrow{M} NO_2 + HO_2$	$k = k_{NO_2+HO_2} / 2{,}1E-27 * \exp(10900/T)$				
$OH + OH \xrightarrow{M} H_2O_2$	6,9 E-31	1	2,6 E-11	0	
$CO + OH \xrightarrow{O_2} CO_2 + HO_2$					(1,5E-13)x(1+0,6 P)
$NO + HO_2 \rightarrow OH + NO_2$					8,1 E-12
$HO_2 + HO_2 \xrightarrow{M} H_2O_2 + O_2$					(4,9E-32)*[M]
$OH + HONO \rightarrow H_2O + NO_2$					4,5E-12
$H_2O_2 + OH \rightarrow HO_2 + H_2O$					1,7E-12
$HO_2 + OH \rightarrow O_2 + H_2O$					1,1E-12
$CH_3O_2 + HO_2 \rightarrow CH_3OOH + O_2$					5,2E-12
$CH_3O_2 + NO \rightarrow CH_3O + NO_2$					7,7E-12
$CH_3O + O_2 \rightarrow CH_2O + HO_2$					1,9E-15
$CH_3O + NO \xrightarrow{M} CH_3ONO$	1,4E-29	3,8	3,6E-11	0,6	
$HO_2 + walls \rightarrow non-radical\ products$					1,5

Table 4.1 Reaction scheme used to model the CL. The rate coefficients are in of cm^3 $molecule^{-1}s^{-1}$ except for the first order heterogeneous wall loss of HO_2 and the unimolecular decomposition of H_2O_2 which are in s^{-1}.

In Table 4.1 the termolecular reaction rate coefficients are calculated according to the following Tore expression that is explained in section 1.3 in detail.

$$k_r(M,T) = \frac{k_0(T)[M]k_\infty(T)}{k_0(T)[M] + k_\infty(T)} F(M, k_\infty(T), k_0(T)) \qquad (1.67)$$

The decay of HO_2 and the production of NO_2 are the main equations, which are the combination of the intermediate decay and production equations of the other molecules. The decay of HO_2 and production of NO_2 can be expressed like this;

$$\begin{aligned}\frac{d[HO_2]}{dt} = &-k_{NO+HO_2}[HO_2][NO] + k_{CO+OH}[CO][OH] - k_{wall}[HO_2] \\ &- k_{NO_2}[NO_2][HO_2] - k_{HO_2+HO_2}[HO_2][HO_2] - k_{OH+HO_2}[OH][HO_2] \\ &+ k_{OH+H_2O_2}[H_2O_2][OH] - k_{CH_3O_2+HO_2}[HO_2][CH_3O_2] + k_{HO_2NO_2}[HO_2NO_2] \\ &+ k_{CH_3O+O_2}[CH_3O][O_2]\end{aligned} \tag{4.12}$$

$$\begin{aligned}\frac{dNO_2}{dt} = &\, k_{NO+HO_2}[HO_2][NO_2] - k_{OH+NO_2}[OH][NO_2] - k_{NO_2+HO_2}[NO_2][HO_2] \\ &+ k_{HONO+OH}[OH][HONO] + k_{HO_2NO_2}[HO_2][NO_2] + k_{CH_3O_2+NO}[CH_3O_2][NO]\end{aligned} \tag{4.13}$$

The initial value of HO_2 is an input of the algorithm. The production of NO_2 is calculated by the differencing of the equations by RK4. The production of NO_2 results from the competition between amplification reactions (1.18),(1.26) and termination reactions (1.81),(1.74),(1.82),(1.83),(1.50),(1.84) ,i.e the wall losses and chemical losses of HO_2 and OH. The CL in the program is obtained dividing the NO_2 produced by the initial HO_2 value. The reactions rates used for this work are from JPL publication 02-25.

In order to check the performance of the model some simulations were compared for the same conditions with a previous study by Clemitshaw et al., 1997 that uses FACSIMILE/CHECKMAT program (Curtis and Sweetenham, (1988)) . Figure 4.1 , 4.2, 4.3 compares the results which show a very good agreement.

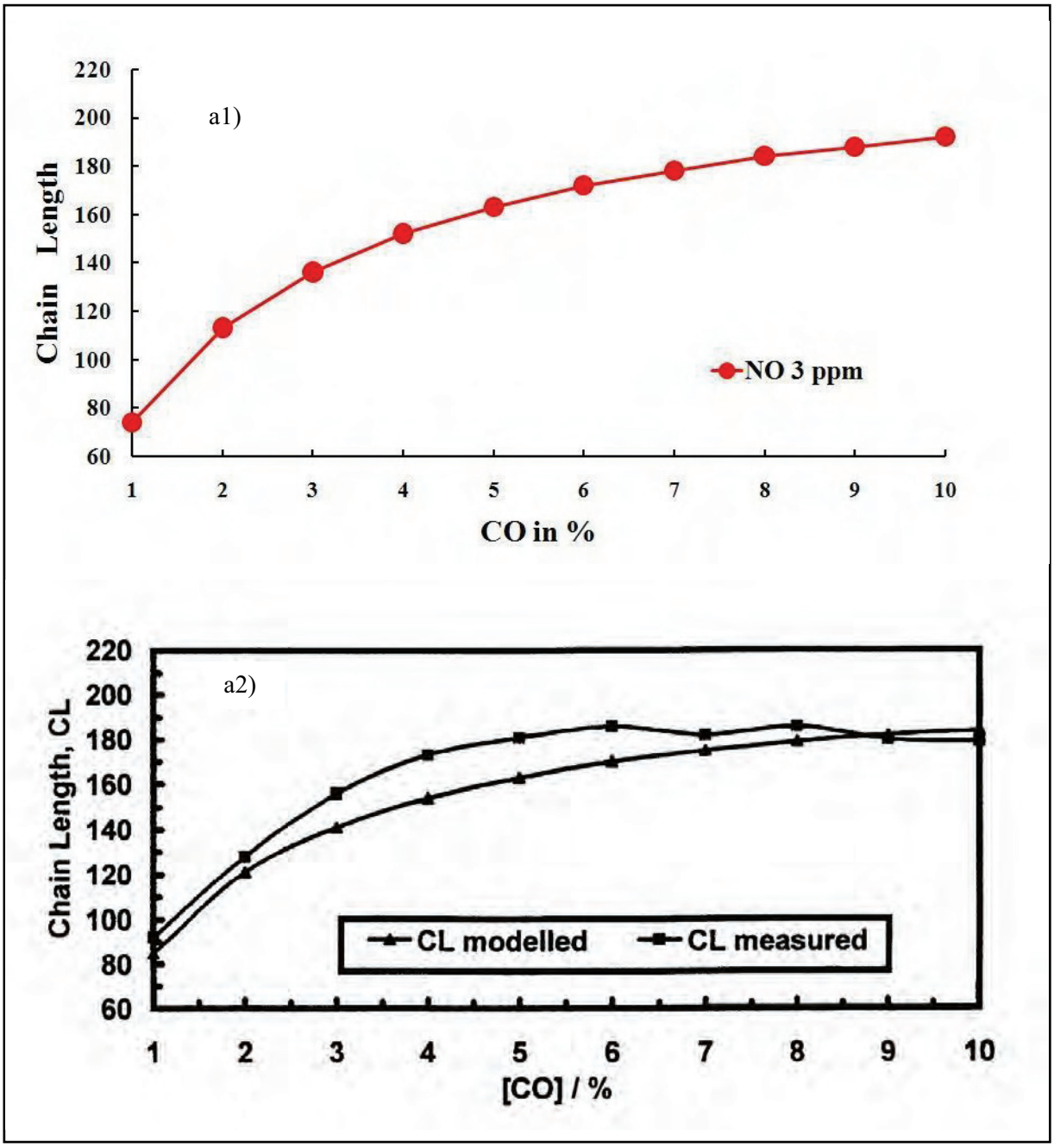

Figure 4.1 Variation of CL with CO mixing ratio at 3 ppm NO and with 50 ppt CH_3O_2 initial mixing ratio.
a1) CL simulation of this work.
a2) CL simulation and measurement of Clemitshaw et al., (1997).

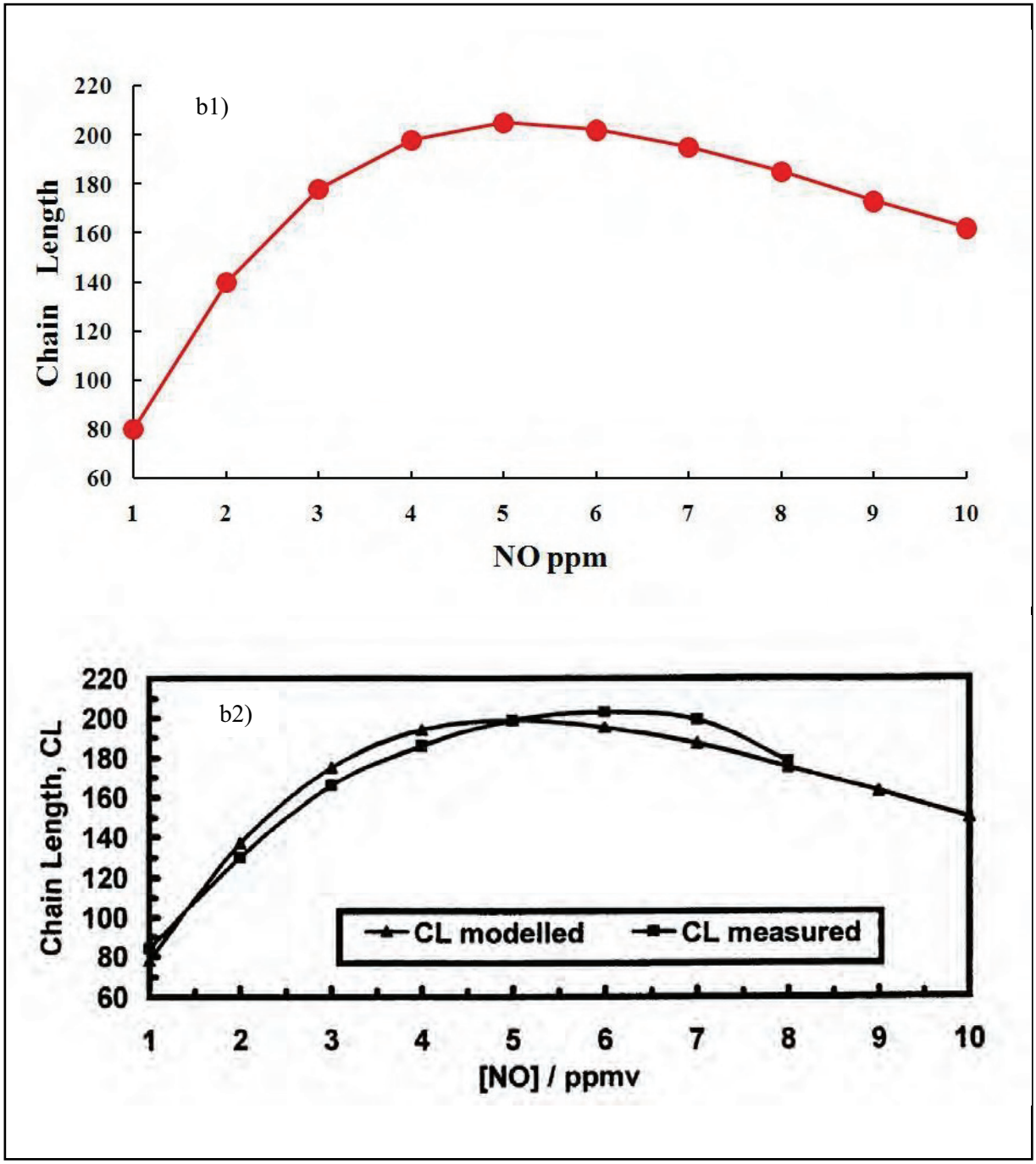

Figure 4.2 Variation of CL with NO mixing ratio at 7 % CO and 50 ppt CH_3O_2 initial mixing ratio.
b1) CL simulation of this work.
b2) CL simulation and measurement of Clemitshaw et al., (1997)

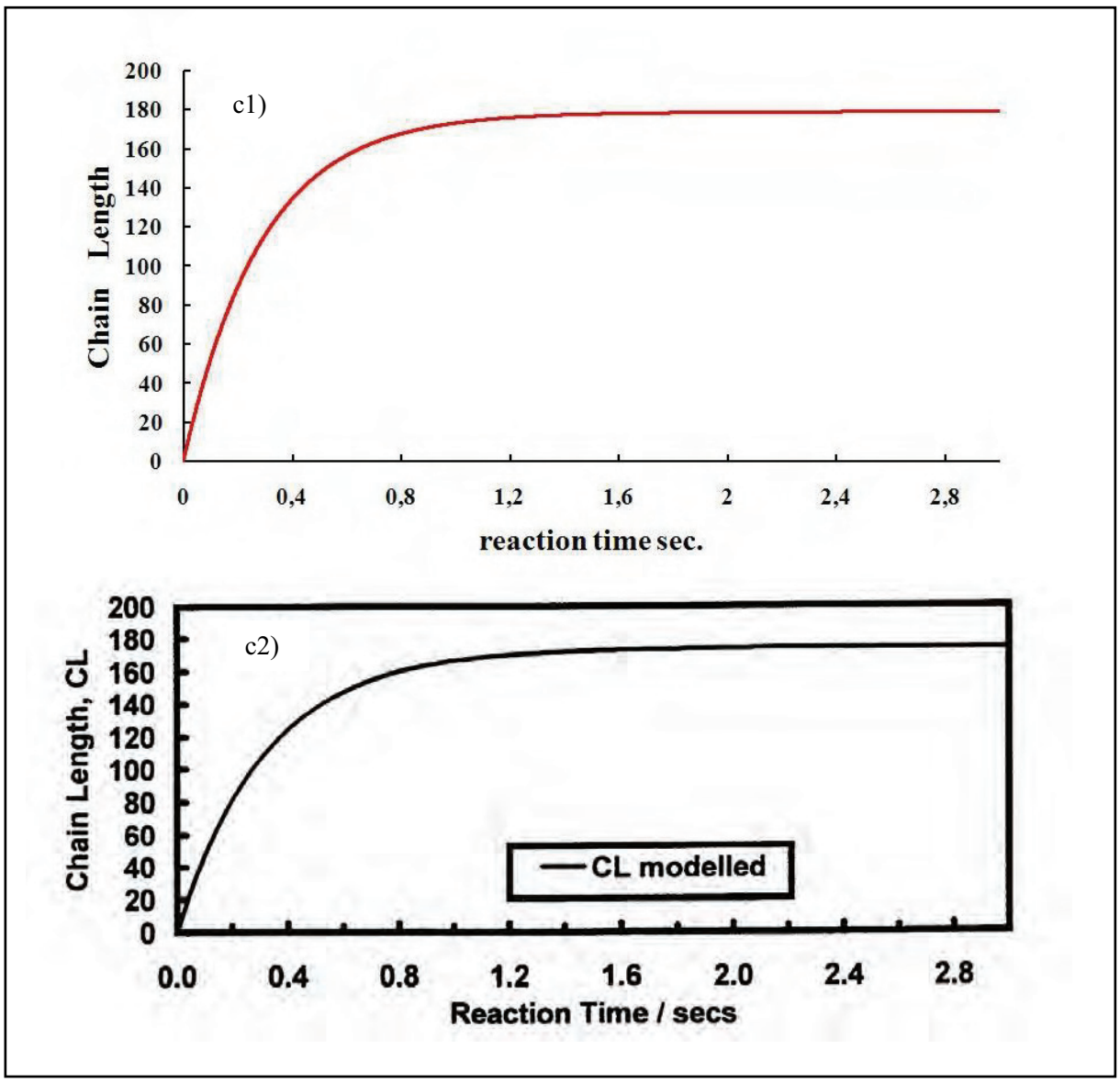

Figure 4.3 Time evaluation of CL at NO 3 ppm and CO 7 % and 50 ppt CH_3O_2 with initial mixing ratio.
c1) CL simulation of this work.
c2) CL simulation of Clemitshaw et al., (1997)

5 Measurement Campaign AMMA SOP2

As presented in the introduction of the present work, the West African Monsoon (WAM) is believed to be critical for global atmospheric chemistry. Information about the chemical composition over West Africa is up to date extremely limited. Therefore research studies oriented at different scientific disciplines are still required to improve the understanding of the WAM.

Figure 5.1 Region of interest of the special observation period SOP2 in West Africa

In this context the international project AMMA (African Monsoon Multidisciplinary Analysis) has been proposed with main following scientific objectives:

- Research in the processes influencing African monsoon dynamics and its variability: weather systems, mesoscale convective systems, easterly waves and tropical cyclones.

- Investigation of the surface conditions strongly affecting the nature of WAM and its variability. This aims to evaluate the impact of the evolution of land cover features in the hydrological cycle of the region, and the relation between food, water sources and health

- Research of the aerosols and mineral dust sources and composition in Africa to minimise the uncertainties of the aerosols impact on weather and climate

- Investigation of the tropical African region as significant source of natural and anthropogenic precursors of key greenhouse gases and atmospheric aerosols.

Among the atmospheric chemistry research within the AMMA project, a particularly important motivation is to gain deeper information about the perturbation of the emissions of West Africa in the regional and global radiative forcing and oxidizing capacity of the atmosphere. The present work is a part of this research area with the focus on peroxy radical measurements playing an essential role in the photochemical activity of the atmosphere.

The AMMA project is divided in the so called special observation periods (SOP), focusing on the characterisation of different phases within the African monsoon (pre monsoon, monsoon and post monsoon periods).

The IUP-UB participated in the SOP2 which aimed the research of multiple scale interactions, between surface conditions, synoptic environment and the convective system, specially focusing on the transport of trace gases.

During SOP2 airborne measurements from 5 scientific aircrafts (DLR-Falcon, French-Flacon, Geophysica, F-ATR 42, UK-BAe 146) were operating for atmospheric measurements. The DLR-Falcon and Geophysica were located at Ouagdougou military airport in Burkina Faso (12.15°N 1.30°W) while the rest of the aircrafts were located in Niamey airport. The map of the region of interest for the measurements can be seen in Figure 5.1.

The airborne measurements took place between 1 and 18 August 2006. During this time 8 flight measurements were conducted by DLR-Falcon team from Ouadougou to investigate the role of the MCS and WAM on aerosol and trace gas mobilization and transport. The flight tracks were planned according to the MCS monitoring and trajectory tracer calculations.

The flight tracks and satellite MCS images (http://amma.iug.fuw.edu.pl/en/flights/list/) are summarised in Figure 5.2 and Figure 5.3 .

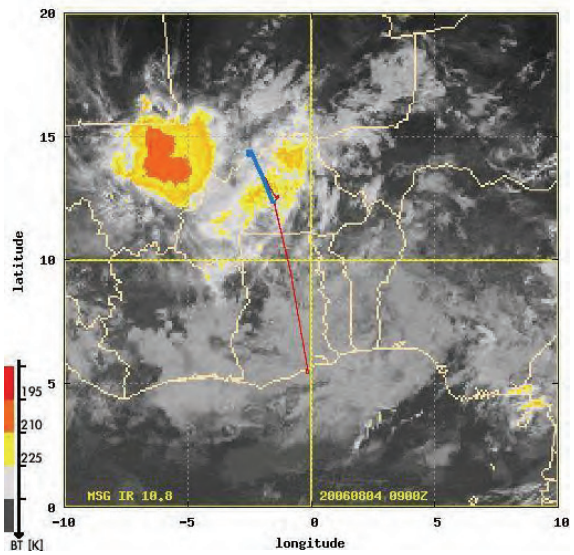

4.August.2006
Objective: investigation of the large scale impact of WAM on trace gas and aerosol budgets in the upper.

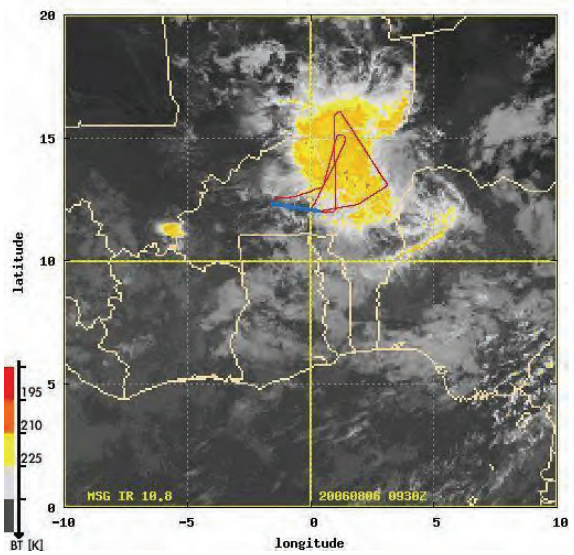

6.August.2006
Objective: investigation of the outflow of MCS over Mali.

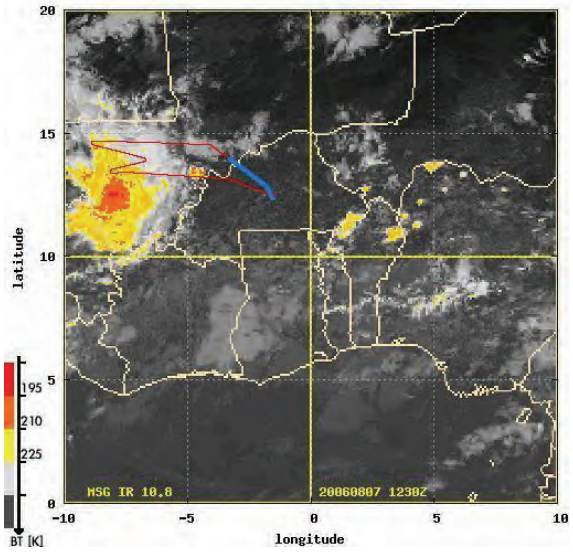

7.August.2006
Objective: investigation of MCS over Guinea.

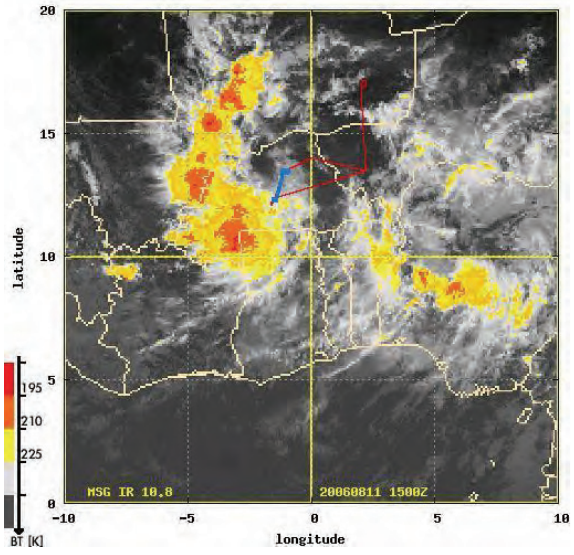

11.August.2006
Objective: Investigation of the outflow of MCS over Mali.

Figure 5.2 Flight tracks of DLR-Falcon during SOP2_AMMA and MCS images.

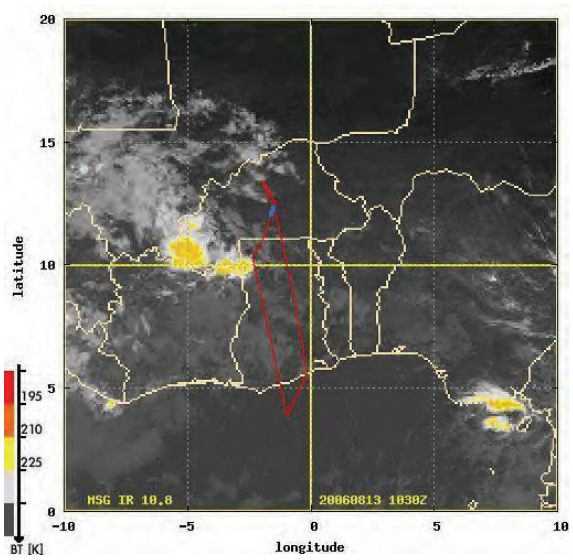

13.August.2006
Objective: Large scale impact of WAM on trace gas and aerosol budgets in the upper troposphere.

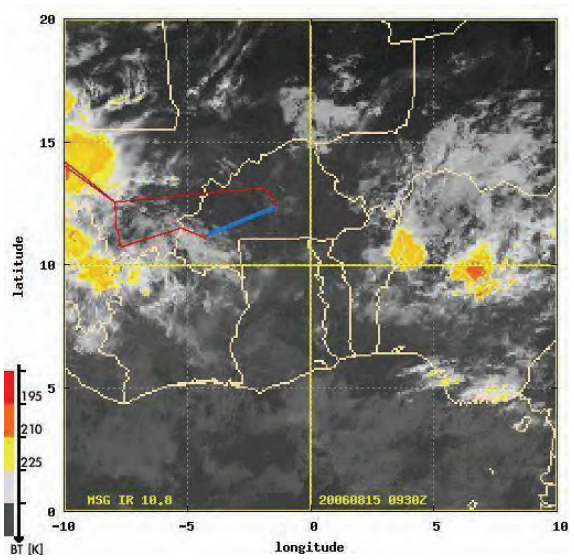

15.August.2006, Flight 1
Objective: Investigation of the MCS outflow over Senegal.

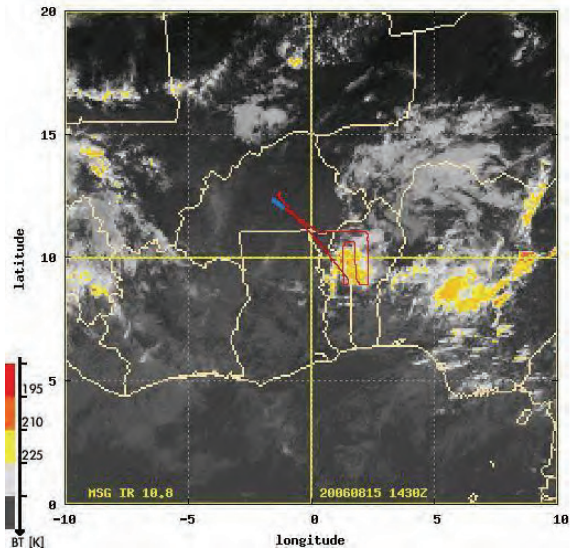

15.August.2006, Flight 2
Objective: Investigation of local convection over Benin

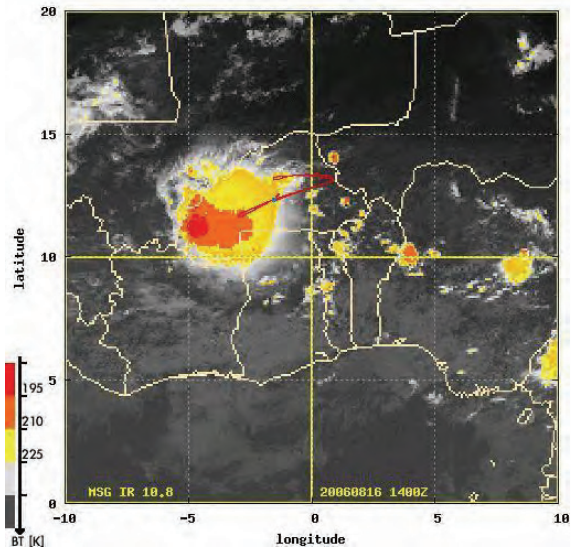

16.August.2006
Intercomparison exercise between UK-BAe140 and DLR-Falcon.

Figure 5.3 Flight tracks of DLR-Falcon during SOP2_AMMA and MCS images.

5.1 Overview of the IUP-UB contribution to the AMMA project

As mentioned in the introduction, the present work focus on the improvement of the PERCA technique by developing a DUALER instrument (Dual channel Airborne peroxy radical chemical amplifiER) for airborne measurements and on the analysis of the peroxy radical measurements carried out during the AMMA measurement campaign on board the research aircraft DLR-Falcon.

The DUALER instrument was deployed and functioning in all the DLR-Falcon flights carried out during the SOP2. The results are described and interpreted in chapter 6. The following text intends to give an overview about the experimental drawbacks affecting the quality of the measurements obtained.

First of all, it is important to note that the DUALER is maintained during the flights at a constant pressure, lower than the ambient, and the corresponding eCL is determined in the laboratory. This is the consequence of the decreases in NO_2 detector sensitivity and CL with decreasing the pressure (see section 6.1). In order to cover the range the pressure levels during the flights but still keeping a reasonable detection limit, 200 mbar was the pressure selected for the AMMA campaign. It was empirically observed that the effective regulation of the pressure required a pressure gradient $\Delta P = P_{ambient} - P_{DUALER}$ of approximately 70 mbar. Otherwise instabilities in the instrument response lead to meaningless results. Generally, the addition of gases was switched off for ambient pressures lower than 250 mbar to save the limited CO available on board due to safety regulations. This fact limits somewhat the amount of RO_2^* data available especially during the flights for the characterisation of the MCS outflow which were often carried out at altitudes corresponding to pressure levels lower than 250 mbar.

Another important restriction influencing the quality of the measurements was the short time flown at some pressure levels. This specially affects the vertical profiles of trace gases taken by the DLR-Falcon. Generally the aircraft remained at each single pressure level only for a few minutes leading to poor statistics of the RO_2^* measurement signals, especially in the case of unexpected variations of concentrations.

The methodology used for the analysis of data, the error analysis and the interpretation of the data obtained are presented in detail in Chapter 6.

6 Results and Discussion

In this chapter the main results obtained within this work are presented and discussed. The chapter consist of two parts:

Section 6.1 focuses on the series of experiments performed to characterise and optimize the DUALER described in Chapter 3. Main objective is the investigation of the effect of pressure in the instrument performance. The box model described in Chapter 4 is used to simulate chemical and physical processes taking place in the reactors to enrich the interpretation of the experimental results which have been partly submitted for publication (Kartal, et al.,2009).

Section 6.2 presents the result of measurements obtained during the AMMA measurement campaign at West Africa in 2006. The methodology developed to analyse the peroxy radical data is discussed in detail. The last part of this section focuses on the interpretation of the measurements obtained during of intense convection and biomass burning. Some of these data have been published within this work (Andrés Hernández, Kartal et al., 2009).

6.1 Laboratory Characterization and Optimization of the DUALER

The characterization of the effect of the pressure variations in the NO_2 detector sensitivity, CL parameter and the general performance of the instrument is an important issue in the characterization procedure of an airborne PERCA. For this purpose, the pressure chamber is described in Chapter 3 was implemented in the calibration procedure of DUALER and a series of experiments were carried out.

6.1.1 Pressure dependency of the NO_2 detector sensitivity

In order to investigate the pressure dependency of the NO_2 detector response a single reactor was installed in the pressure chamber (see section 3.2.2).The pressure in the chamber was varied between 200-1000mbar and NO_2 calibrations were performed at different pressures. The calibrations are carried out with the same source of NO_2 (10 ppm NO_2 in synthetic air) and the offset mixing ratio of the NO_2 detector is the same for all sensitivity determinations. The results of the calibration series is presented in Figure 6.1. The detector sensitivity is defined as S=1/a being $[NO_2]$= ax+b and x the detector signal in volts (see section 3.3.1).

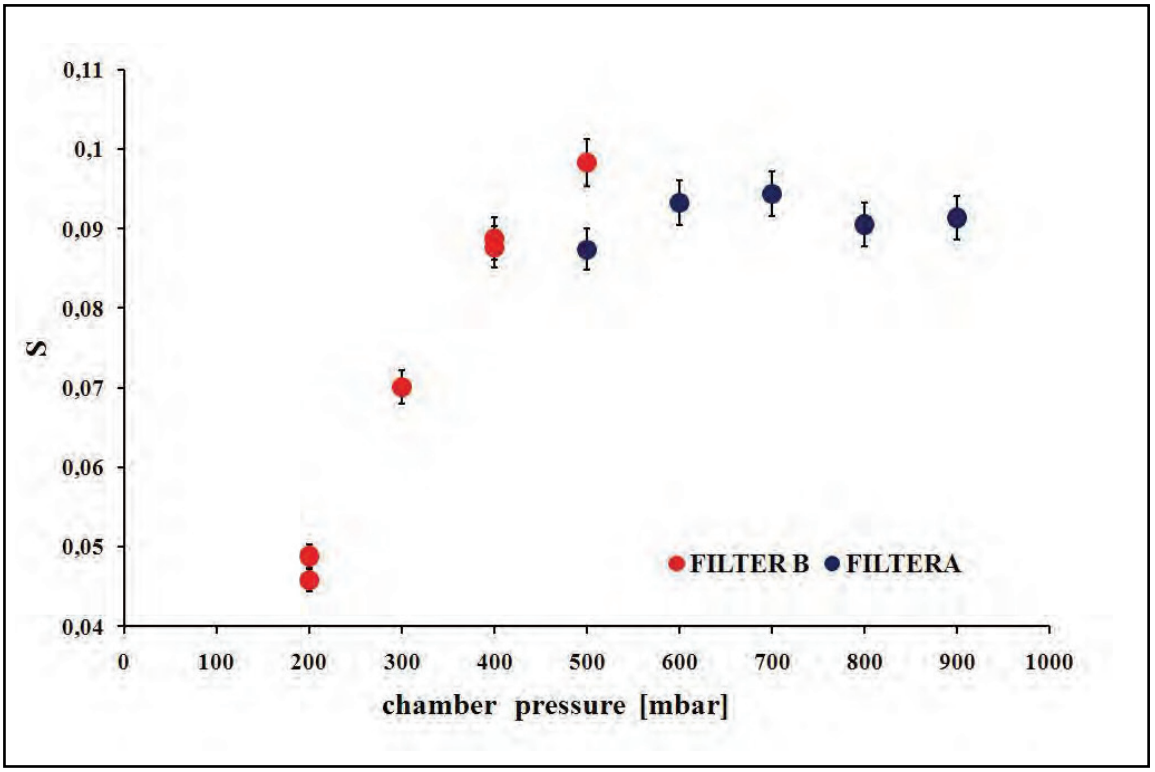

Figure 6.1 Variation of the detector sensitivity (S) with pressure. S=1/a being $[NO_2]$= ax +b and x the detector signal in volts.

After each pressure change the measurement system requires a time for the stabilization of the detector signal. Between the pressures 500 mbar and 900 mbar the sensitivity values remain within the error bars. Due to the observed decrease in the sensitivity as a consequence of filter ageing, the filter paper was replaced at 500 mbar to continue with the experimental series. As expected, the sensitivity of the detector improves after changing the filter. From 500 to 200 mbar the decrease in the pressure is associated to significant decrease in the sensitivity down to 45-50% at 200 mbar.

The decrease in sensitivity can be attributed to:

- decrease of the absolute number of NO_2 molecules per volume that reacts with luminol, which can be critical below 500 mbar,
- low retention time of the NO_2 molecules in the detector due to the higher volume associated to the constant mass flow at each pressure value, leading to a deterioration in the efficiency of the reaction with luminol.
- drying out of luminol on the filter paper more efficient higher volume flows. As a consequence the surface contact for reaction diminishes and consequently the efficiency of the reaction decreases.

It can be therefore concluded, that the sensitivity changes of the NO_2 detector and the time required for the stabilization of the detector response after each pressure change indicate the necessity to keep the instrument at a constant pressure to get a stable response during airborne measurements.

6.1.2 Pressure dependency of the chain length

The experimental set up used to determine the pressure dependency of the NO_2 detector sensitivity is also used to determine the chain lengths for different pressures.

In the determination procedure of CL the oxygen column dependency of the effective absorption cross section has to be considered. The oxygen column dependency of the effective absorption cross section due to the large gradient of oxygen absorption cross section with wavelength (see Figure 3.15) and extended spectral signature of the lamp around 184,9 nm, are the likely reasons for decreasing absorption cross sections with increasing O_2 columns (Creasey et al., 2000). Pressure variations lead to a variation in the O_2 columns. Therefore, for each pressure level investigated within this work, the apparent oxygen absorption cross section was determined for different O_2 columns, to obtain the dependency of the apparent oxygen cross section on the O_2 column. The experimental set-up and the determination of the value of effective oxygen absorption cross section for each pressure in the chamber is explained in detail in section 3.3.2.1. The effective O_2 absorption cross section determined over the whole presssure range are depicted in Figure 6.2.

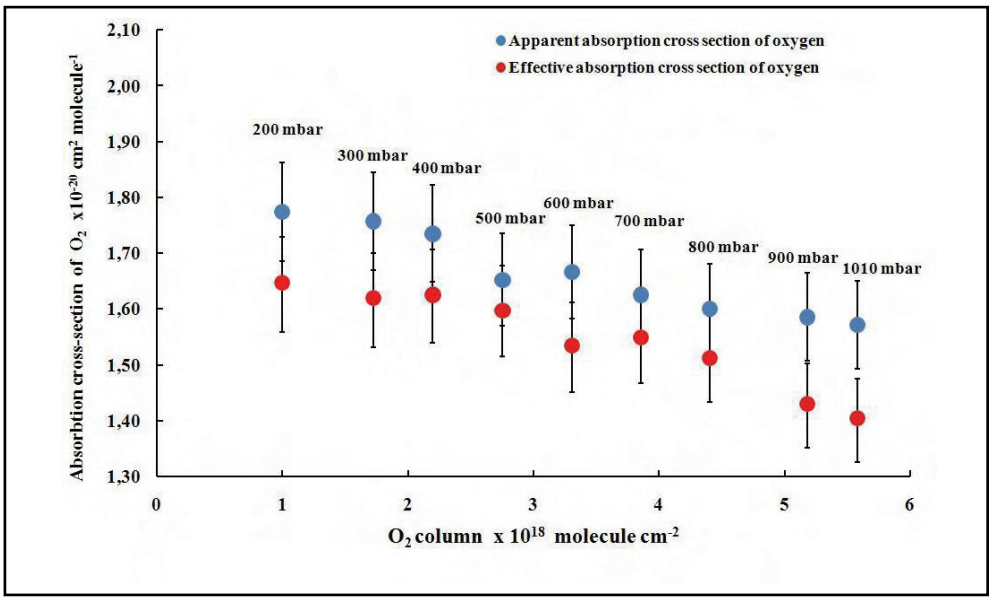

Figure 6.2 Effective and apparent O_2 absorption cross sections for each pressure in the chamber

The absorption cross section of water is constant over the whole oxygen column as a consequence of the linearity of the absorption amount of the light by water molecules at wavelength 184,9 nm. The oxygen mixing ratio is constant (known from the specifications of the gas cylinder) and the water mixing ratio is calculated from the dew point sensor measurements at all pressure levels.

The ozone production of the HO_2 source is determined as explained in section 3.3.2.2. The amount of HO_2 produced in HO_2 source was calculated accurately with these values. The CL obtained at the pressures between 200-100 mbar are presented in Figure 6.3.

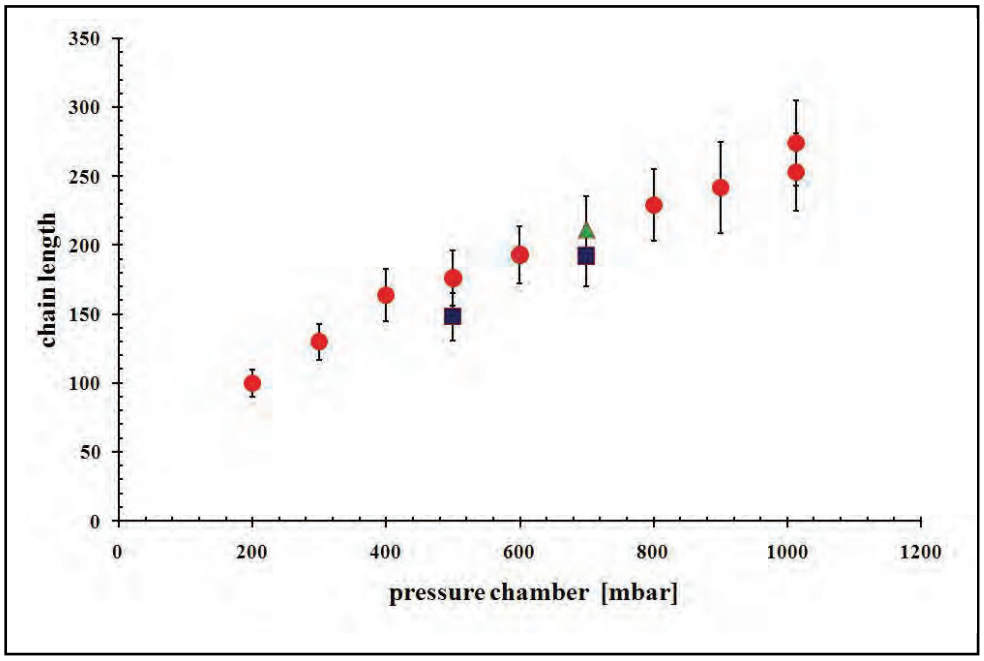

Figure 6.3 Variation of CL with pressure

The decrease of the pressure leads to a decrease in the CL which is expected by the consideration that the wall losses are gaining in importance as the molecular collusion probability decreases with decreasing the absolute number of molecules of the reagent gases CO and NO. The more important chemical losses from reactions (1.74), (1.82), (1.83) are pressure dependent and are slower with decreasing pressure. As a consequence, the effect of the wall losses in terminating the chain reaction is more significant.

In addition the reaction (1.26) in the amplification cycle is pressure dependent; as the pressure decreases the rate of the reaction decreases.

At 500 and 700 mbar no CO was added at the HO_2 source during the calibration (square data points in Figure 6.3). In this case the calibration unit is acting as a source of OH and HO_2 as the OH which is the photolysis product of H_2O is not converted completely to HO_2 in the source.

The chain lengths values for 500 mbar in Figure 6.3 are determined with and without addition CO in the source. The 15% chain length reduction, when the CO is not added to the source, is due to the losses of OH until reaching the amplification point of the reactor. The box model (see Chapter 4) is used to determine a wall loss rate for OH from the information of the chain length reduction. The calculate wall loss rate for OH is 9 s^{-1} which is 6 times higher than the HO_2 wall loss rate deduced from the measurements. This wall loss rate (9 s^{-1}) at 700 mbar leads in the model to 33% OH loss that is accompanied with 16% CL reduction (see Figure 6.4).

If the value CL value obtained by no CO addition in the source is recalculated with this 16% reduction, the result is 228. Considering the trend of the decrease of CL with pressure, the correction for CL at 700 mbar as 210 (see Figure 6.3) has high confidence level and as the error of CL determination is between 10-16% ,the corrected value covers the model result (CL=228), whose determination procedure is according to the experimental results.

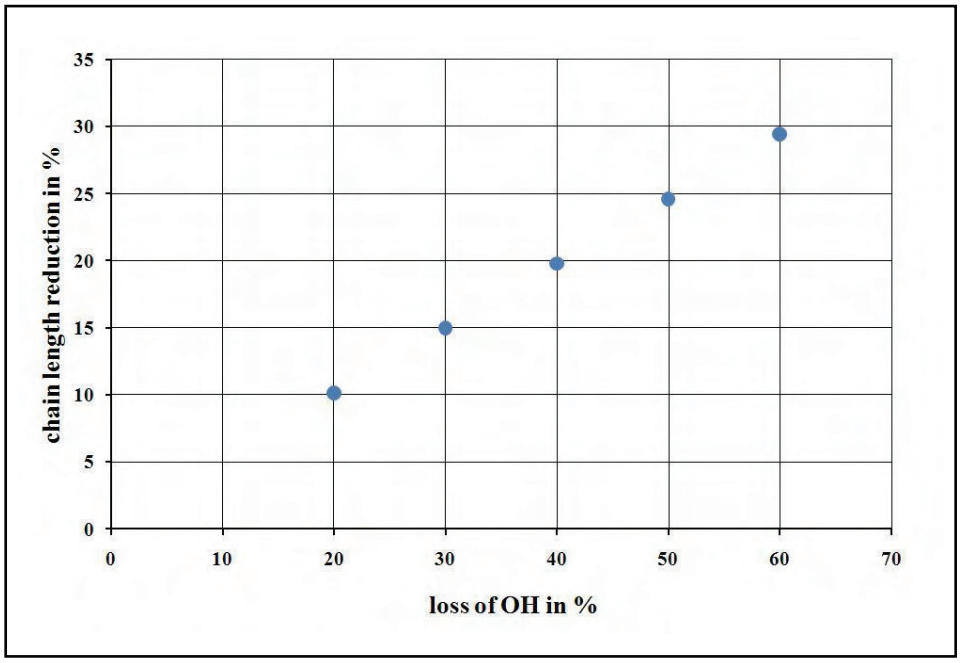

Figure 6.4 Effect of OH loss in the CL when CO is not added at the radical source at 700 mbar.

The total effect of physical and chemical reactions at different pressures has been studied with the help of the box model presented in Chapter 4. The box model was used to simulate the CL values for different pressures by considering the pressure dependency of the reactions.

The wall losses are not calculated by the model but adjusted according to the experimental CL obtained at 1000 mbar. The corresponding $k_{wall\ HO_2} = 1{,}5\ s^{-1}$ is kept constant all over the pressure range.

In Figure 6.5 the CL experimental and simulated are compared.

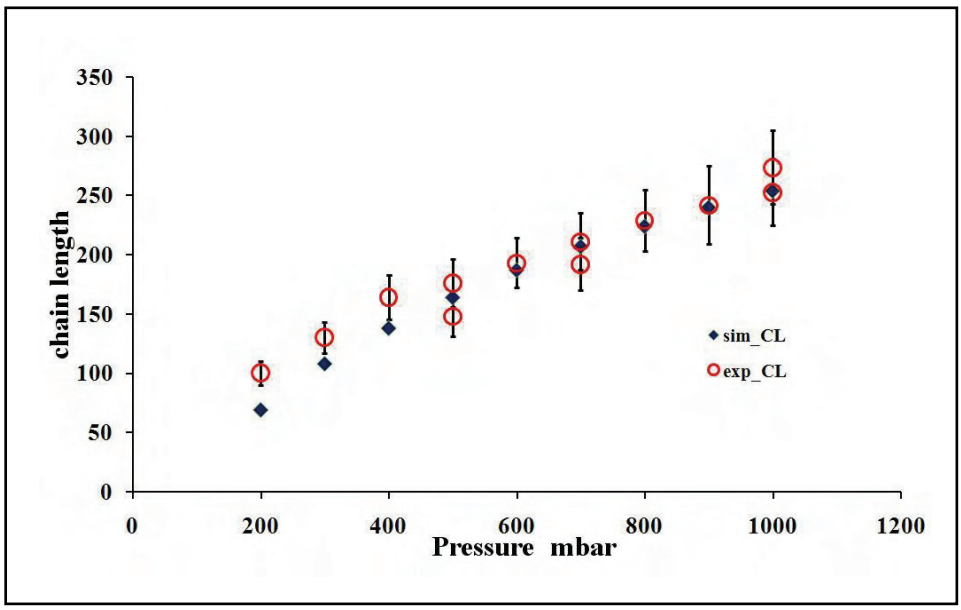

Figure 6.5 Experimental and simulated CL with constant wall loss rate 1.5 s^{-1} at pressures between 200-1000 mbar.

The simulated CL in Figure 6.5 agrees very well with the experimental results above 600 mbar, between 200-500 mbar the experimental values are higher than the simulated CL. This can be attributed to a decrease of the wall losses at lower pressures as a consequence of lower retention time before reaching the addition gasses (see section 6.1.4).

If the wall loss rate is set to zero the chain length increases with decreasing pressure due to the lower efficiency of the pressure dependent chemical losses. The simulated chain length evolution with time at zero wall losses at 1000 mbar and 200 mbar is presented in Figure 6.6.

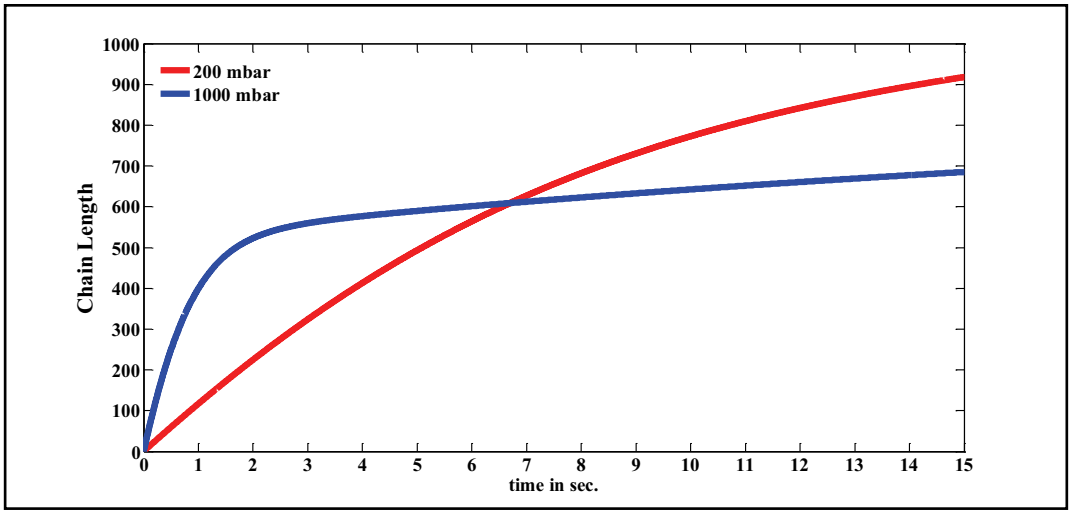

Figure 6.6 Temporal evolution of chain length for k_{wall}=0 s^{-1} at 200 and 1000 mbar.

As shown in Figure 6.6, the chain length is completed in a shorter time at 1000 mbar than at 200 mbar due to the decreasing rates of the chemical losses at the lower pressure.

In Figure 6.7 the wall losses rate in the reactor is set to 1,5 s^{-1} for both pressures and the retention times of the sample gas according to the experimental operation marked at the plot.

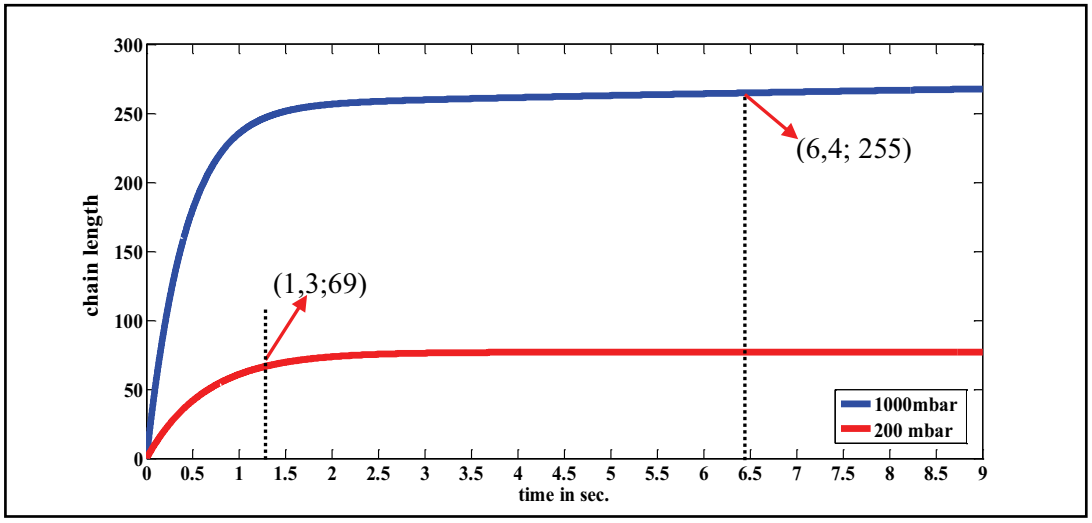

Figure 6.7 Chain length temporal evolution at 200 and 1000 mbar for k_{wall}= 1,5 s^{-1}

According to the simulation at 1000 mbar the retention time in the reactor is enough for completing the chain reactions, but if the k_{wall} is considered to be constant all over the pressure ranges, at 200 mbar the chain reaction is not completed in the reactor, it could be increase around 8% if the retention time were 1,8 instead of 1,3 sec. This result indicates the convenience to increase the retention time in the reactor when measuring at low pressures, in order to optimize the CL value.

In summary, the experimental results obtained imply that the airborne measurements should be performed with a measurement system kept at a constant pressure to gain a stable response of the detectors and a constant CL.

As mentioned in section 3.1, these results were the motivation and bases for the design of a DUALER system kept at constant pressure for the measurement of peroxy radicals at airborne platforms.

6.1.3 Characterization of the effect of pressure variations for the DUALER

In order to characterize the CL and detector sensitivity variation with the pressure, the DUALER inlet was installed in the pressure chamber (see section 3.2.2).

The DUALER pre-reactor nozzle is kept at constant pressure (200 and 300 mbar) while the pressure in the chamber is varied between 1000 and 300 mbar. The reagent gases (CO,NO), whose mixing ratio variations influence the chain length (see section 1.4.4.2) are adjusted to the values used for flight measurements (CO 7,4%, NO 3ppm).

The experimental configuration is shown schematically in Figure 6.8.

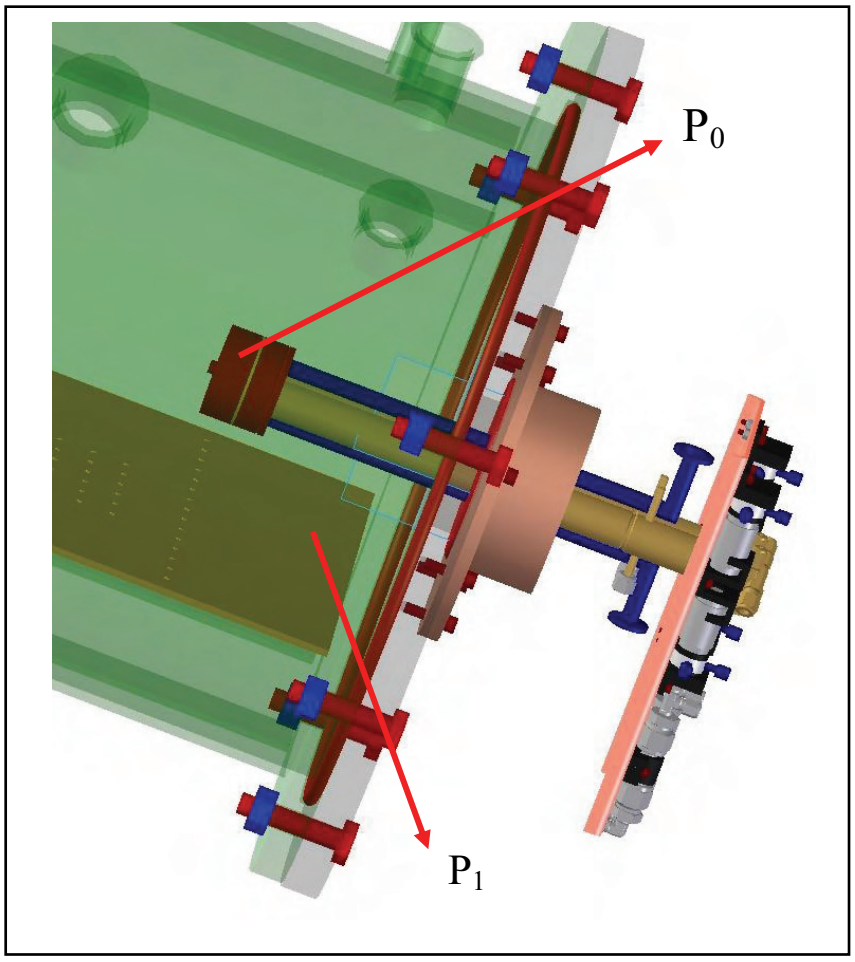

Figure 6.8 Schematic representation of the set up for the calibration of the DUALER. P_0=constant, P_1 variable.

6.1.3.1 Pressure dependency of NO_2 detector sensitivity of DUALER

Each DUALER reactor is connected to a detector. The NO_2 sensitivity can be different for each detector due to the mechanical properties and the flow differences of the luminol through the filter papers installed in the reactor (see section 3.2.2 and Figure 3.5). The NO_2 calibrations are performed by keeping the pressure at DUALER at 200 mbar.

The NO_2 sensitivity results for a calibration series are presented in Figure 6.9.

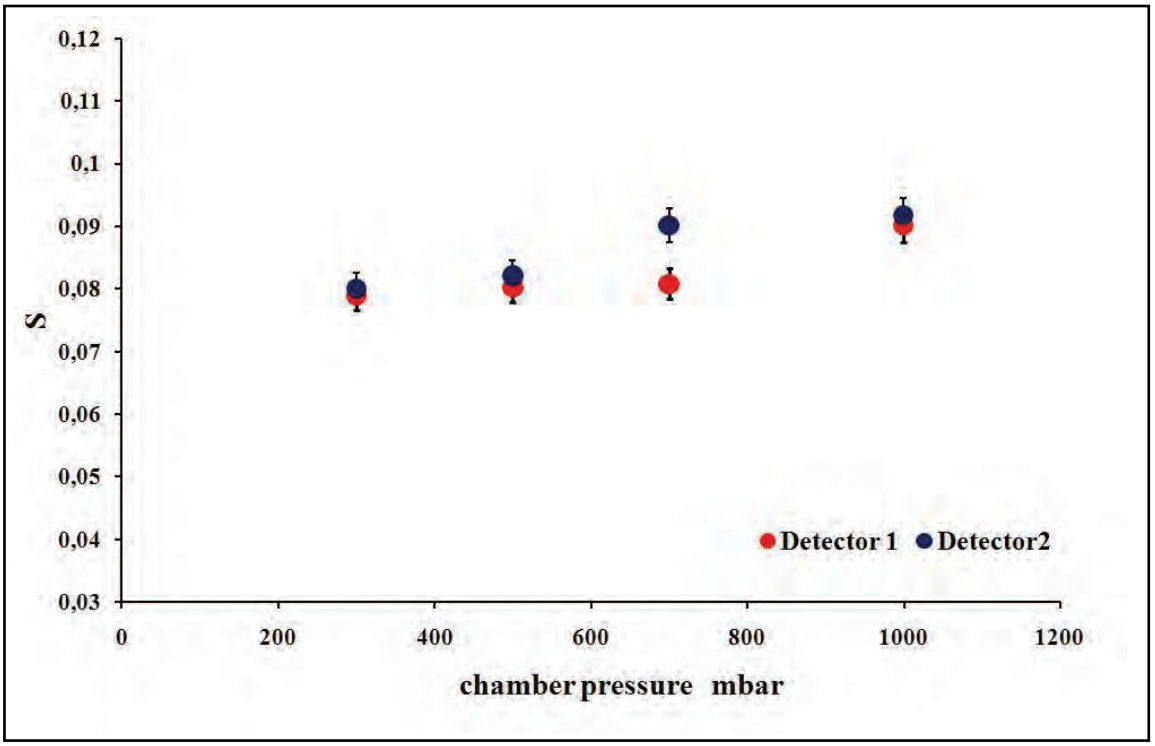

Figure 6.9 Variation of NO_2 detector sensitivity when keeping the DUALER pre-reactor nozzle at 200 mbar. S=1/a ; being $[NO_2]$=ax+b and x the signal of detectors in volts.

The sensitivity of the detectors remains constant when the measurement system is kept at constant pressure. The sensitivity drop around 10% that is seen in both detectors are reasonable as the time between measurement points is around 20 hours, and the older the filter ,the less sensitive is the detector.

In addition, it is important to note that the stabilization time required by the system after the pressure changes in the chamber is much shorter than in the case of not regulated system presented in section 6.1.1.

In Figure 6.10 the sensitivity changes with the pressure for DUALER detector and for a non regulated system are compared. There is a clear improvement in the stability of the detector response when the pressure of the instrument is kept constant as in the DUALER.

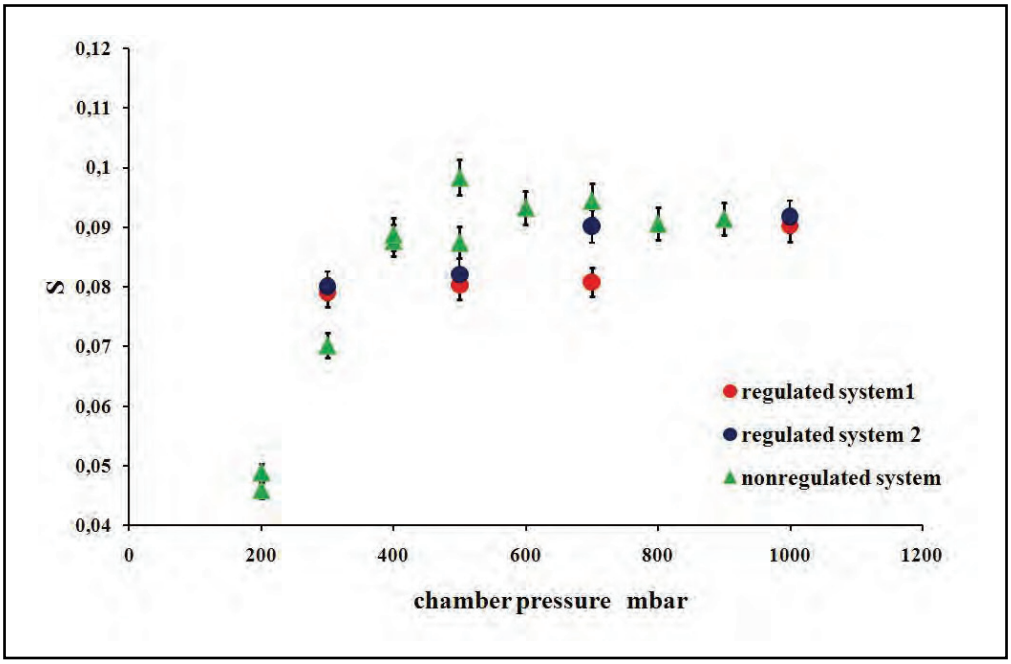

Figure 6.10 Comparison of the NO_2 detector sensitivities of a pressure regulated and a non regulated systems.

6.1.3.2 The characterization of CL of DUALER reactors

The CL of DUALER is expected to be lower than the CL of a single reactor as explained in section 6.1.2 due to the losses occurring in the pre-reactor nozzle. The pre-reactor nozzle of DUALER partly acts as a trap for the HO_2 produced at the calibration source. HO_2 entering the pre-reactor nozzle is partly lost due to the wall losses and radical-radical reaction (1.50) before they reach the addition point at the reactors where the amplification and conversion take place. Consequently, the amplification cycle in the reactors produces NO_2 corresponding to a lower mixing ratio (see Figure 6.11). As the chain length is calculated according to the known amount mixing ratio of HO_2 entering the pre-reactor nozzle, the CL for DUALER called effective chain length (eCL), is lower than the CL determined at 200 and 300 mbar in section 6.1.2.

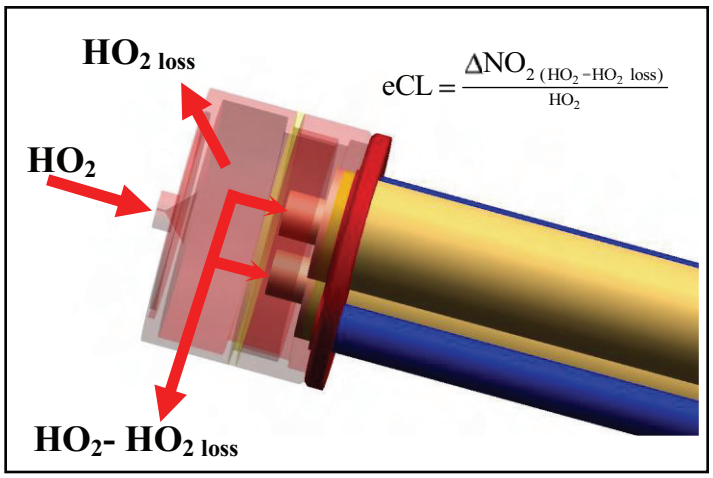

Figure 6.11 Schematic description HO_2 losses at the pre-reactor nozzle.

The eCL for the DUALER is obtained by performing the same operation conditions (see section 3.5) of the flight measurements are presented in Figure 6.12 and Figure 6.13.

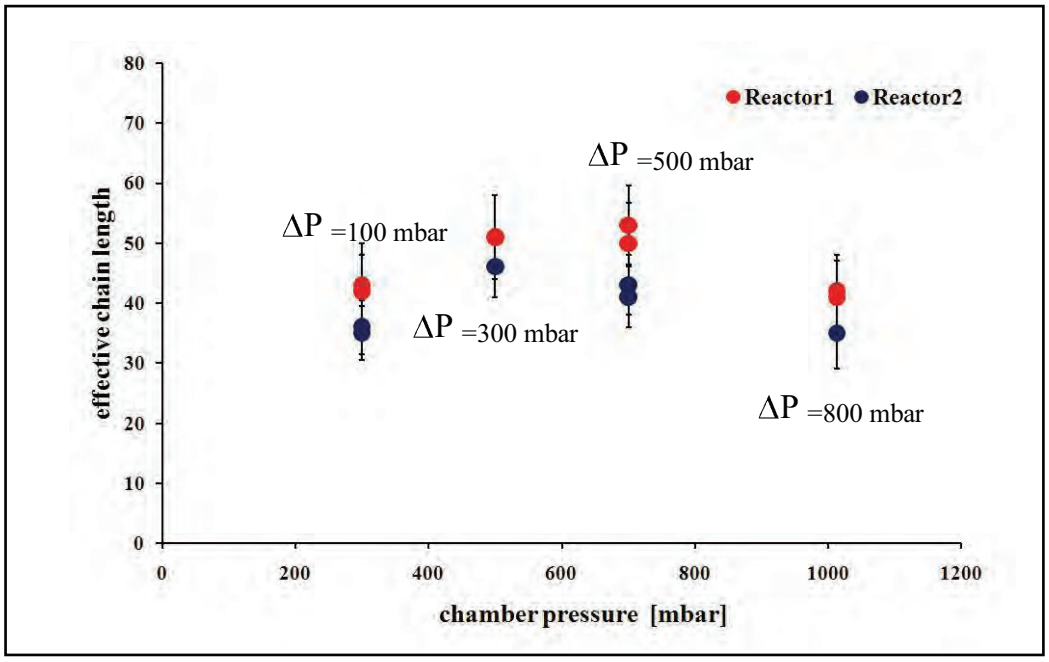

Figure 6.12 Variation of eCL with the ambient pressure. The DUALER is kept at 200 mbar. $\Delta P = P_1 - P_0$ (see Figure 6.11)

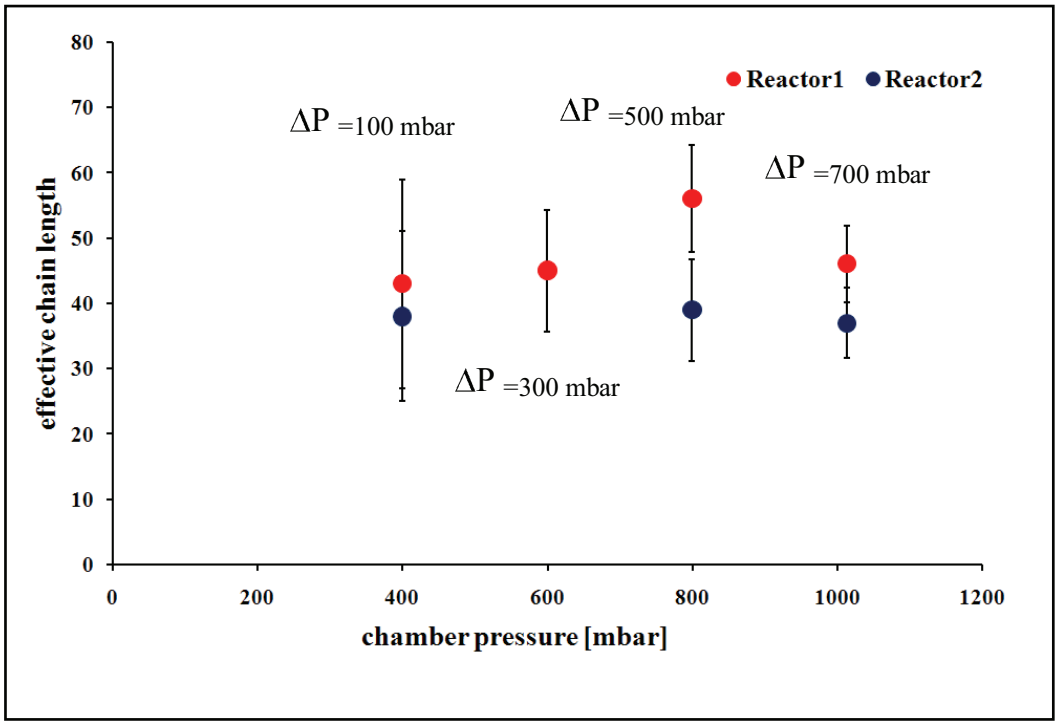

Figure 6.13 Variation of eCL with the ambient pressure. The DUALER is kept at 300 mbar. $\Delta P = P_1 - P_0$ (see Figure 6.11)

The eCLs in Figure 6.12 and Figure 6.13 is obtained as the DUALER pressure is regulated at 200 mbar and 300 mbar.

It should be noted that the reactors of DUALER have slightly different eCL although they are supposed to be identical. This might be due to slight differences of the geometrical and surface properties of the reactors and detectors.

The eCL for different pressures at Figure 6.12 present a slight curvature with a maximum around 600 mbar. At different chamber pressures, the DUALER is at 200 mbar, for each change of the pressure in the chamber, the ΔP changes. The slight curvature can be attributed to the ΔP changes. If ΔP is high, the entrance velocity of the calibration gas is high, leading to turbulences at the entrance of the DUALER inlet, which can cause radical losses. As ΔP decreases the entrance velocity is lower, leading to higher retention time at the entrance of DUALER inlet, which can also cause radical losses. The curvature can be explained as the result of the competition of both effects which seems to reach a kind of compensation at the intermediate pressures.

The eCL values presented in Figure 6.13 are obtained when the DUALER is kept at 300 mbar. The larger error bars of the eCL are related to instabilities in the luminol flows of the NO_2 detectors (see section 3.1.1). There is no significant difference between the eCL values obtained by keeping the DUALER at 200 and at 300 mbar.

6.1.4 Characterization of the of the DUALER pre-reactor nozzle

The DUALER consists of two reactors which are the same as the reactor installed in the chamber in Figure 3.13. In order to gain more information about the processes occurring in the pre-reactor nozzle, a series of experiments were carried out with the DUALER without regulating the pressure. The CL obtained, defined as eCL^*(eCL^*: eCL when the DUALER is not regulated) were compared with the CL obtained for a single reactor in section 6.1.2. The Figure 6.14 shows schematically the experimental configurations whose results are compared.

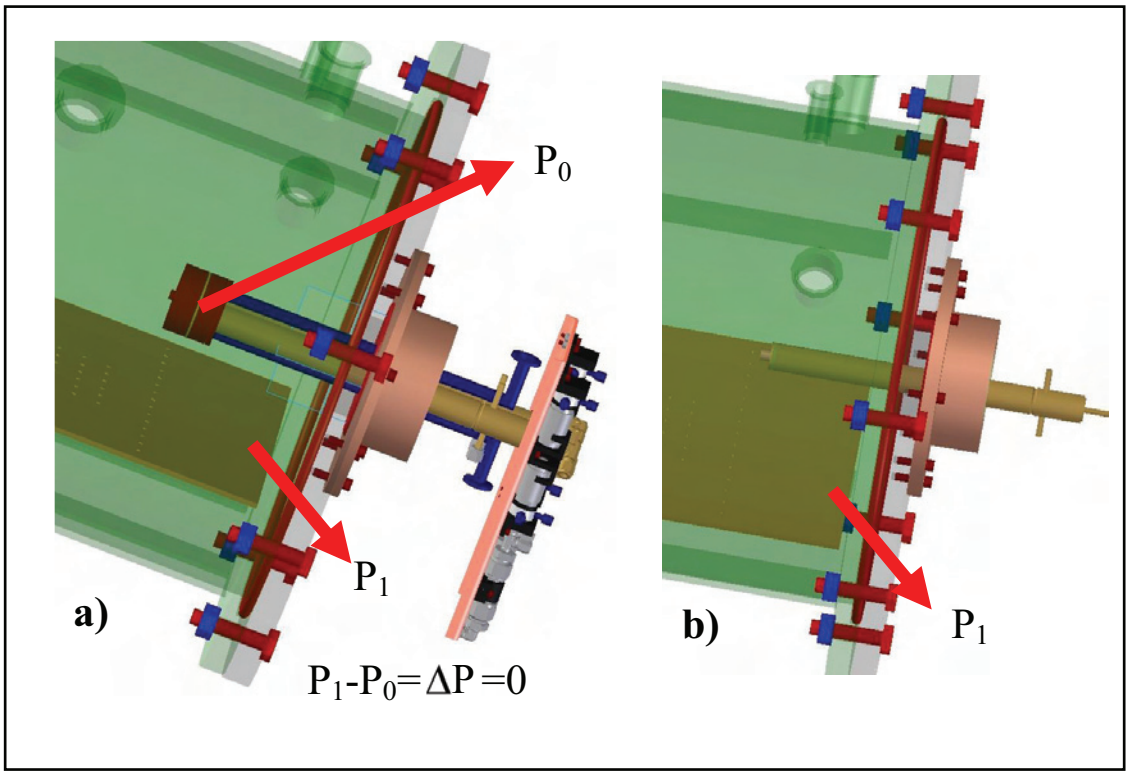

Figure 6.14 Experimental set up used to investigate the losses at the pre-reactor nozzle.
a) DUALER, b) single reactor.

Figure 6.15 shows the eCL* values obtained for the DUALER at different ambient pressure

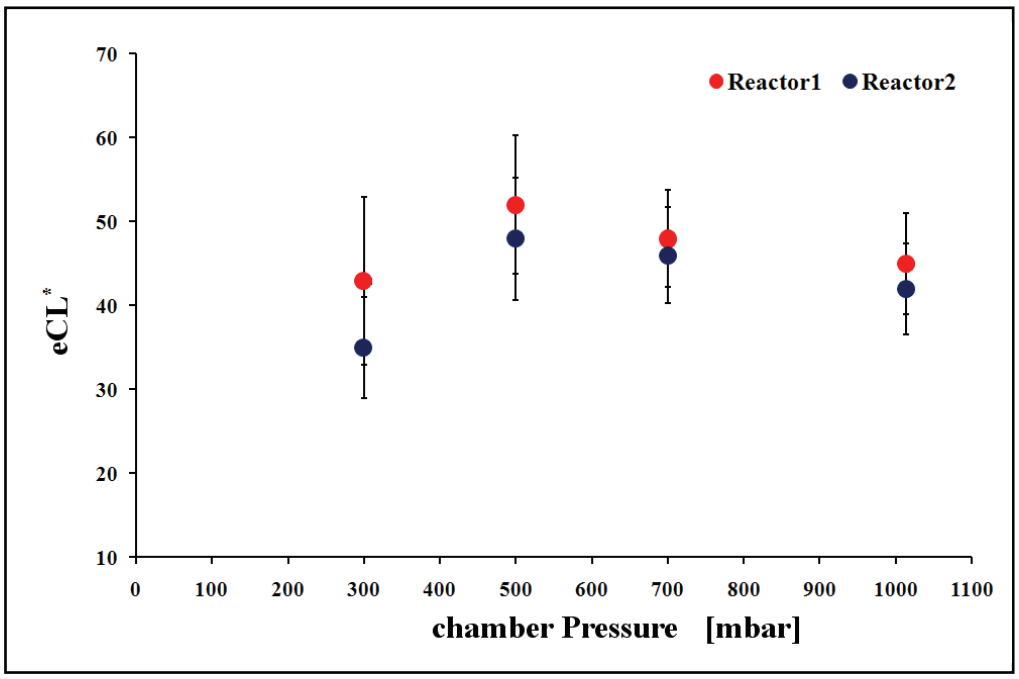

Figure 6.15 Effective chain length of DUALER without pressure regulation (eCL*).

The eCL* results presented in Figure 6.15 is used to obtain the ratio eCL*/CL. The results can be seen in Table 6.1.With increasing pressure the ratio of eCL*/CL is decreasing. This is due to the low retention time of molecules in the pre-reactor nozzle at low pressures leading to less wall losses. As the P increases the volume flow decreases and the retention time and the associated wall losses increase. The retention time can be defined as t*:

$$t^* = \frac{\text{pre} - \text{reactor nozzle volume}}{\text{volume flow}} \tag{6.1}$$

The DUALER eCL* experimental results (Figure 6.15) and the CL_{single} experimental results (Figure 6.3) for a single reactor of DUALER at the corresponding pressure are listed in Table 6.1.

Pressure	CL_{single}	ΔCL_{single}	eCL*	ΔeCL^*	eCL^*/CL_{single}	t* sec.
300 mbar	130	12	43	10	0,33	0,49
500 mbar	176	20	52	8,25	0,295	0,81
700 mbar	210	24	48	5,8	0,228	1,14
1000 mbar	253	28	45	6	0,177	1,65

Table 6.1 The experimental results for the single reactor and non-regulated DUALER set up

The ratio of $\frac{eCL^*}{CL}$ is inversely proportional to the retention time of the molecules in the pre-reactor nozzle. Thus:

$$\frac{eCL^*}{CL} \alpha \frac{1}{t_{retention}} \qquad (6.2)$$

In Figure 6.16 the $\frac{eCL^*}{CL}$ experimental values versus t^* are depicted.

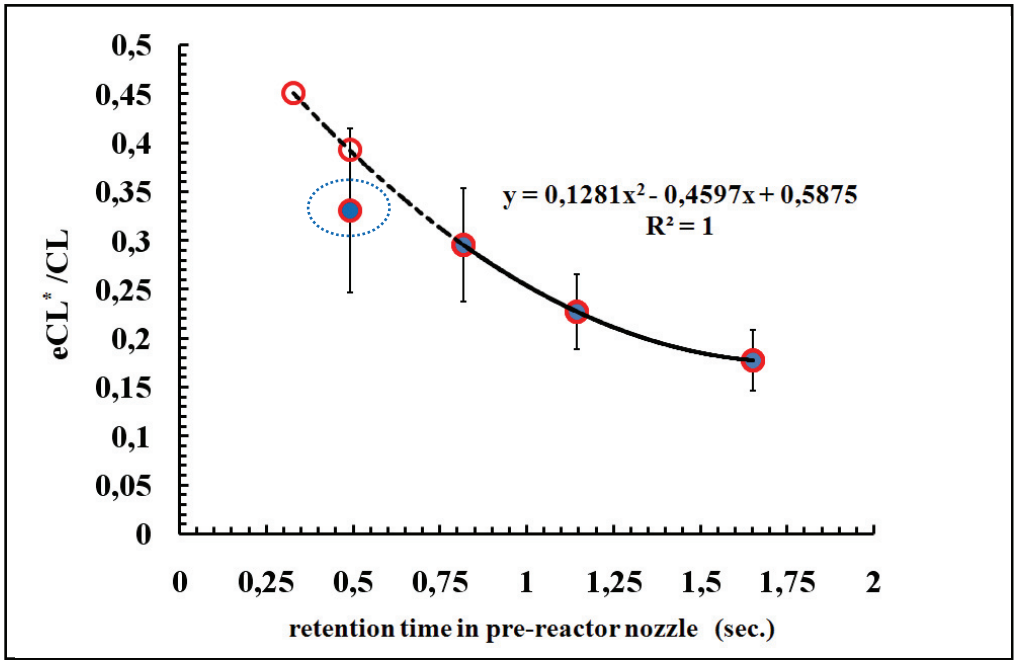

Figure 6.16 eCL^*/CL ratios versus retention time in the pre-reactor nozzle (filled circles are experimental results, empty circles are obtained by the extrapolation of the fit line).

The highlighted data in Figure 6.16 is the ratio of CL and eCL^* determined at 300 mbar, which has larger error due to the luminol flow effects on the response of the NO_2 detectors (Figure 6.15).

The correlation curve in Figure 6.16 enables the estimation of eCL^* at a particular pressure, if the t^* and the CL of the single reactor at these conditions are known. The values for $\frac{eCL^*}{CL}$ at 200 and 300 mbar are extrapolated from the correlation curve. The eCL^* value so obtained for 300 mbar is within the error bar of the eCL^* determined experimentally for this pressure. The eCL^* obtained with the same manner for 200 mbar agree very reasonably with the eCL determined experimentally when DUALER is kept at 200 mbar. (Figure 6.12 and Table 6.2)

Pressure mbar	CL_{single} experimental	ΔCL_{single}	eCL* and eCL experimental	ΔeCL	eCL^*/CL_{single} calculated	eCL^* calculated	t^* sec.
300	130	12	**eCL* =43**	9	0,39	**51**	0,49
200	100	10	**eCL =43**	7	0,45	**45**	0,32

Table 6.2 Comparison of experimental eCL and with calculated eCL^*.

If the losses occurring in the pre-reactor nozzle are exactly known and considered in the calculation of CL, the CL in the single reactor and in the DUALER reactors should be the same. Therefore;

$$\frac{\Delta NO_{2\ DUALER}}{HO_2 - HO_2^{loss}} = \frac{\Delta NO_{2\ SINGLE}}{HO_2} = CL_{SINGLE} = CL_{DUALER} \tag{6.3}$$

Followed by;

$$\frac{\Delta NO_{2\ SINGLE}}{HO_2}\ \frac{HO_2 - HO_2^{loss}}{\Delta NO_{2\ DUALER}} = 1 \tag{6.4}$$

Since the $\Delta NO_{2\ DUALER}$ corresponds to the conversion and amplification entering the reactor after the losses in the pre-reactor nozzle, the $eCL^*/CL < 1$ is always valid and according to the definition of eCL^*;

$$\frac{eCL^*}{CL} = \frac{\dfrac{\Delta NO_{2\ DUALER}}{HO_2}}{\dfrac{\Delta NO_{2\ SINGLE}}{HO_2}} = \frac{\Delta NO_{2\ DUALER}}{\Delta NO_{2\ SINGLE}} \tag{6.5}$$

Finally combining the equations (6.4) and (6.5) the following equation can be written;

$$\frac{HO_2^{loss}}{HO_2} = 1 - \frac{eCL^*}{CL} \tag{6.6}$$

The equation (6.6) enables to calculate HO_2^{loss} in the pre-reactor nozzle with the knowledge of the CL for the single reactor and DUALER eCL which are obtained without regulating the pressure at pre-reactor nozzle of the inlet. The loss percentage for each eCL^* of DUALER compared with CL of the single reactor is presented in Figure 6.17.

In Figure 6.17 it can be clearly seen that at lower pressures due to the lower retention time in the pre-reactor nozzle the wall losses are lower in percentage. As expected the reduction of the chain length is lower at lower pressures which is at 200 mbar 55% and at 1000 mbar 82%. If the CL for single reactor between 200 and 1000 mbar for all the pressures were equal, according to these losses the eCL would continuously increase starting from 1000 mbar.

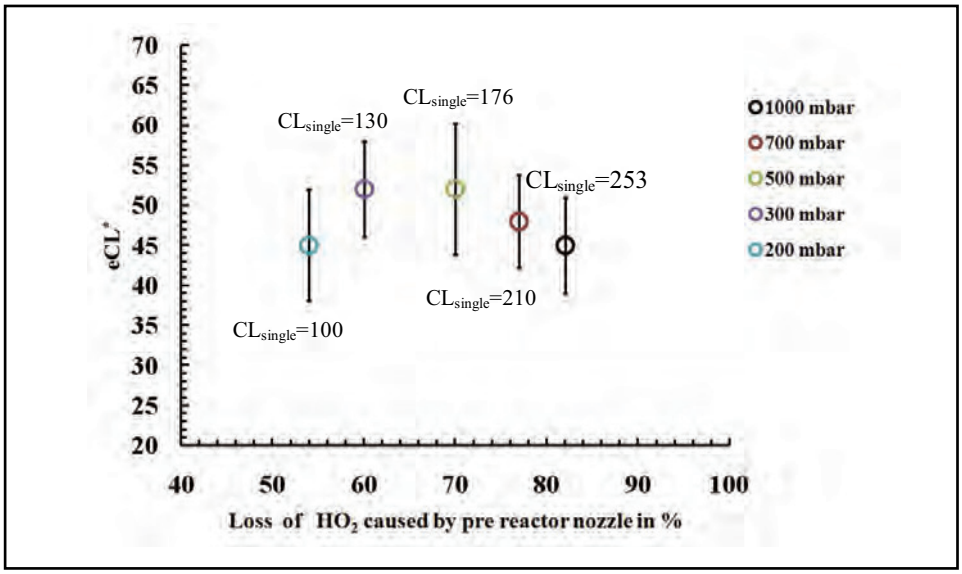

Figure 6.17 HO_2 losses in % at pre-reactor nozzle calculated by Eq (6.6) versus eCL*

The Figure 6.18 shows simulated results obtained with the box model (see Chapter 4) when implementing a radical trap before chemistry initiates. The HO_2 losses are varied between 50 and 90 % and the corresponding eCL^* are calculated. The experimental eCL^* are also depicted for comparison.

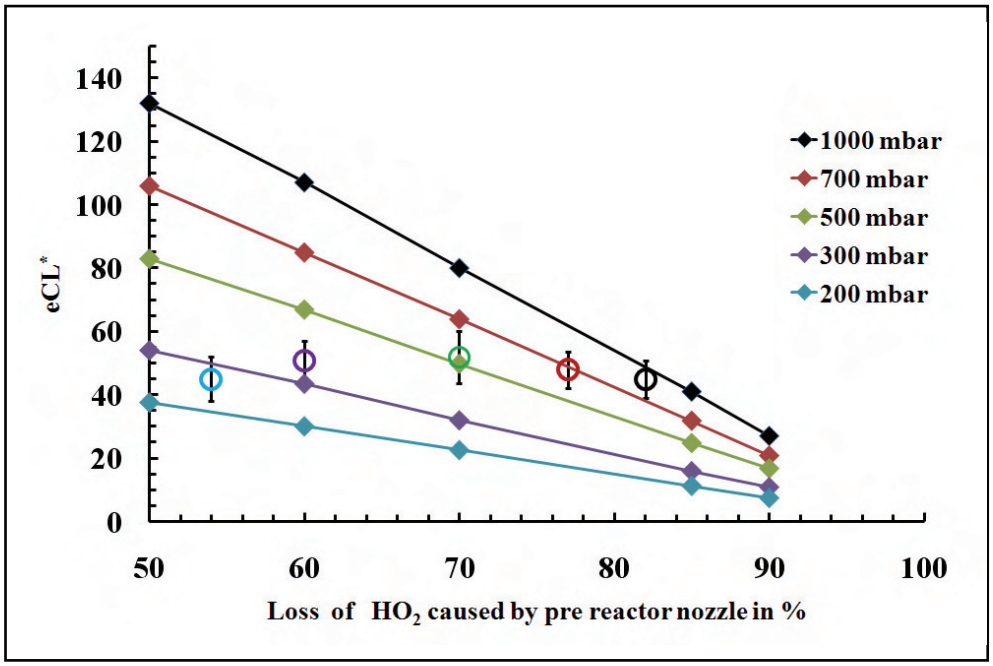

Figure 6.18 The eCL^* and loss percentage comparison of the experimental values (empty circles) and simulated values.

As can be seen in Figure 6.18, there is a good agreement between the values of the losses HO_2 associated to the corresponding eCL^* calculated from the experimental values and simulated by the model.

The losses in the pre-reactor are the result of the wall losses and radical-radical losses (1.50). According to simulations the contribution of the radical-radical losses at 1000 mbar to the total loss is 0,19% at 200 mbar and 0,23% at 1000 mbar. The total HO_2 loss is therefore dominated by the wall losses which can be differently affected by the turbulences.

As the wall losses are dominating the loss process in the following calculations it is assumed that only wall losses are occurring in the pre-reactor nozzle. The HO_2 entering the reactors after wall losses occurring in the pre-reactor nozzle in the time t^* can be expressed like:

$$HO_2(t^*) = HO_{2\ initial} e^{-k_{wall} \cdot t^*} \tag{6.7}$$

The $HO_2(t^*)$ can be calculated from the experimental data by using the equation (6.6) by HO_2 intial value. After the calculation of the $HO_2(t^*)$, the k_{wall} can be determined as following;

$$k_{wall} = \frac{1}{t^*} \ln\left(\frac{HO_{2\ initial}}{HO_2(t^*)}\right) \tag{6.8}$$

The k_{wall} loss rate calculated by the equations (6.6), (6.7), (6.8) for different pressures are plotted in Figure 6.19.

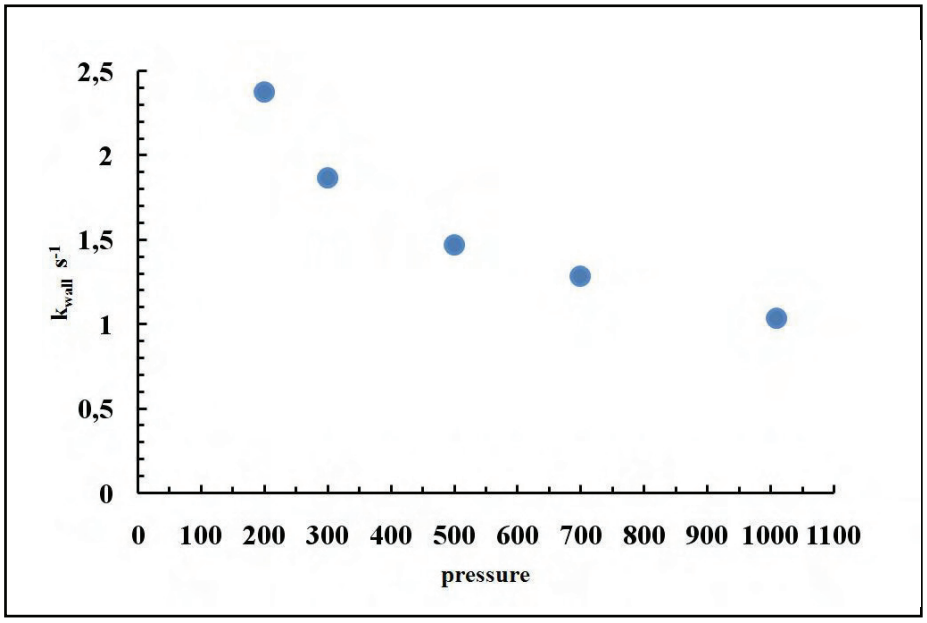

Figure 6.19 Calculated k_{wall} loss rates for each pressure level from the experimental data.

According to Figure 6.19 the wall loss rate is increases with decreasing pressure. The wall loss rate can be estimated by using a set of equations. (Hayman, 1997). The rate coefficient of wall loss is given by

$$k_{wall} = c\frac{S}{V} \tag{6.9}$$

Where S is the surface area,V, the volume and c is a constant. The constant is given by

$$c = Sh\frac{D}{d} \tag{6.10}$$

Where Sh is the Sherwood number (dimonsionless), D, the diffusion coefficient (cm^2 s^{-1})and and d the diameter of the flow tube (cm). The Sherwood number is related to the Reynolds (Re) and Schmidt (Sc) numbers.

$$Sh = 1.85\left(\frac{ReScd}{L}\right)^{1/3} \tag{6.11}$$

where L is the length of the flow tube (cm),.The Reynolds and Schmidt numbers are defined as;

$$Re = \frac{\rho v d}{\eta} \quad ; \quad Sc = \frac{\eta}{\rho D} \tag{6.12}$$

ρ, ν, η the density, velocity (cm s^{-1}), and viscosity (gr cm^{-1} s^{-1}) of the gas.

The equation (6.9) can be expressed as following by combining the equations (6.10), (6.11) (6.12) as :

$$k_{wall} = 1.85\left(\frac{\nu^{1/3}D^{2/3}}{d^{1/3}L^{1/3}}\right)\left(\frac{S}{V}\right) \tag{6.13}$$

In the experimental configuration the S and V, d , L are constant, so the wall loss rate can be rewritten with a constant T of unit $cm^{-5/3}$:

$$k_{wall} = 1.85\ T\ \ \nu^{1/3}D^{2/3} \tag{6.14}$$

The diffusion constant formula;

$$D = \frac{1}{3}\cdot\lambda\cdot\bar{c} \tag{6.15}$$

The mean free path λ decreases as the pressure is increased, so D decreases with increasing pressure and as a result gas molecules diffuse more slowly. The mean speed $\bar{c}$ is directly proportional with temperature which is constant for the experimental set up.

The diffusion coefficient D increases with decreasing pressure and the velocity of the gas sample in the experimental set up increases with decreasing pressure. By equation (6.14) it can be concluded that the wall loss rates are increasing with decreasing pressure. The k_{wall} rates obtained from the experimental data (Figure 6.19) agree with the Eq(6.14).

As the pressure is lower in the pre-reactor nozzle, where no conversion and amplification of HO_2 occurs, the wall loss rate is higher (Figure 6.19) but the retention time is lower. As a consequence the loss percentage is lower at lower pressures as plotted in Figure 6.17.

Concerning the comparison with the CL in the single reactors, the knowledge of the wall loss rate at pre-reactor nozzle can be used to estimate the losses occurring at the single reactor before reaching the amplification reactions (see section 6.1.2). The critical point for wall losses is the surface volume ratio S/V of the entrance of the reactors in Eq (6.13).

While the pre-reactor nozzle has a entrance orifice of 1mm. diameter and 5mm length (S/V ratio of 3,84 mm^{-1}), the single reactor has an entrance with 10 mm diameter and 14 mm length leading to a S/V ratio of 0,4 mm^{-1}. As the S/V ratio of pre-reactor orifice is 9,5 times greater than the single reactor orifice the CL reduction is much less than 4% at 200 and 6% at 1000 mbar. The k_{wall} loss rate within the reactor itself cannot be estimated in the way explained above, and the consideration of the competition with the chemical amplification and terminating reactions is necessary. In the present work the loss rate for the reactors was adjusted according to the experimental results (Figure 6.5).

6.1.5 Determination of eCL with CH_3O_2 and HO_2 mixture

As mentioned in section 1.4.4.2 the wall losses of the peroxy radicals having larger organic chain R are expected to be lower than the HO_2 wall losses.

For this reason a series of calibration experiments were performed with a mixture of CH_3O_2 and HO_2. The mixture of CH_3O_2 and HO_2 is obtained by addition of CH_4 instead of CO in calibration gas explained in detail section 3.3.2. The calibration gas mixing ratio of RO_2^* is consists of 50% CH_3O_2 and 50% HO_2. The obtained results of this experiment by regulating the pressure at pre-reactor nozzle at 300 mbar and in the chamber between 400-1000 mbar are presented in Figure 6.20 .

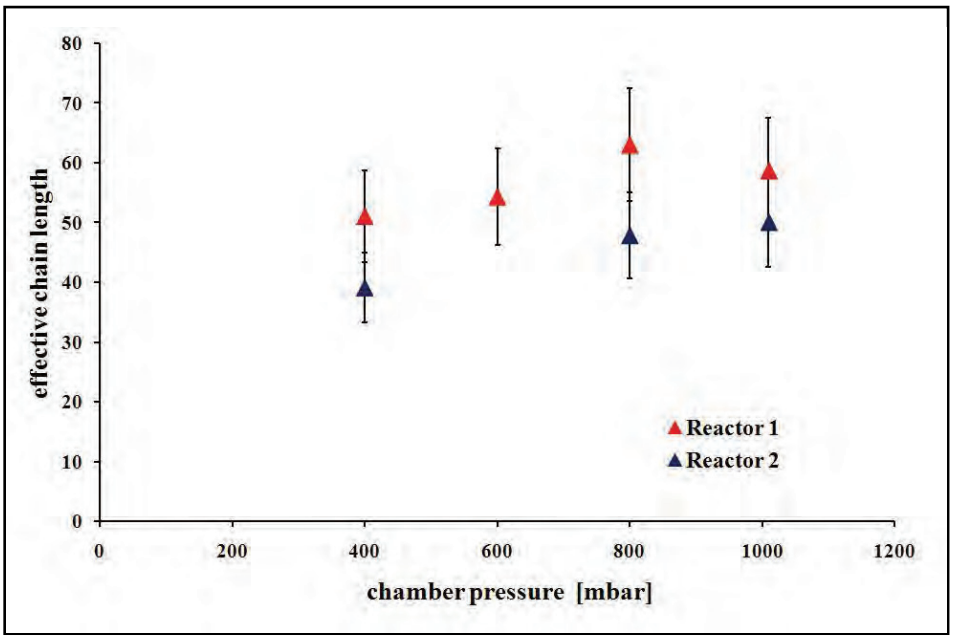

Figure 6.20 eCL obtained for DUALER at 300 mbar for a sample mixture of 50% CH_3O_2 and 50% HO_2 .

The eCLs in Figure 6.20 are higher than the values obtained when the calibration gas contains only HO_2. This is due to the lower wall loses of CH_3O_2 than HO_2 occurring in the pre-reactor nozzle. The eCL is 50± 7,5 for CH_3O_2 and HO_2 mixture from the experimental data in Figure 6.20 and can be used as an experimental reference for determining the loss percentage of the CH_3O_2 at the pre reactor-nozzle. The HO_2 loss in the pre-reactor nozzle at 300 mbar is taken from the series of experiments with the 100% HO_2 sample (see Figure 6.17) and the box model is accordingly modified. The experimental and simulated results are presented in Figure 6.21.

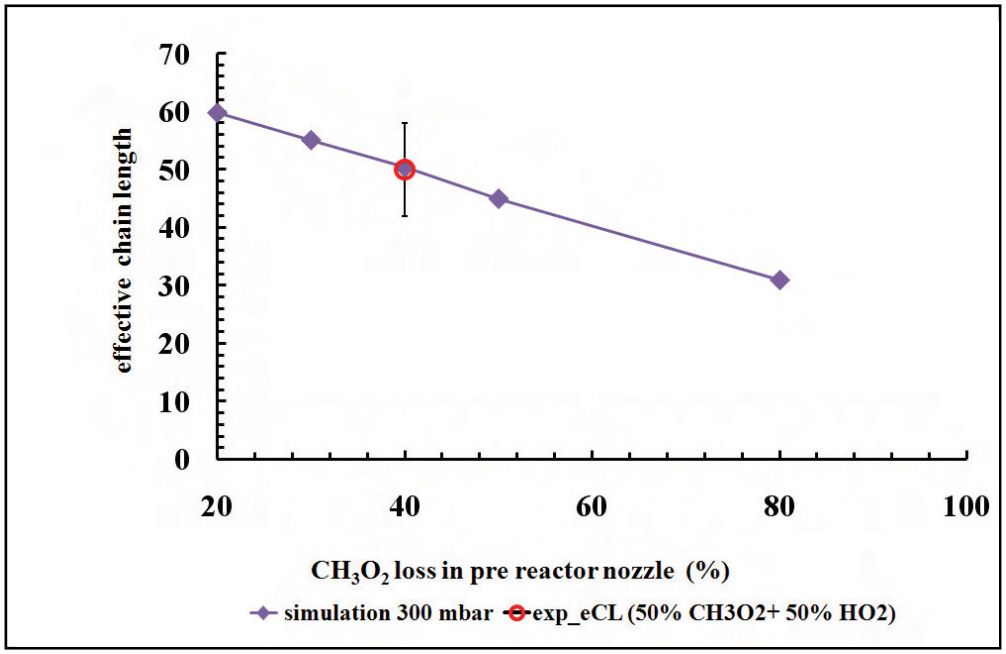

Figure 6.21 Loss percentage of CH_3O_2 in the pre-reactor nozzle and eCL at 300mbar. The the loss of HO_2 at pre-reactor nozzle is 60%.

According to the comparison between experimental and simulated data, at 300 mbar about 40% of the CH_3O_2 radicals are lost at the pre-reactor nozzle before entering the reactors, which implies the CH_3O_2 wall losses are around 30% less than the HO_2 wall losses.

The ratios between eCL obtained for pure HO_2 and for a mixture 50% HO_2 and 50% CH_3O_2 when the DUALER kept at 300 mbar and the pressure chamber between 400-1000mbar, are presented in Figure 6.22.

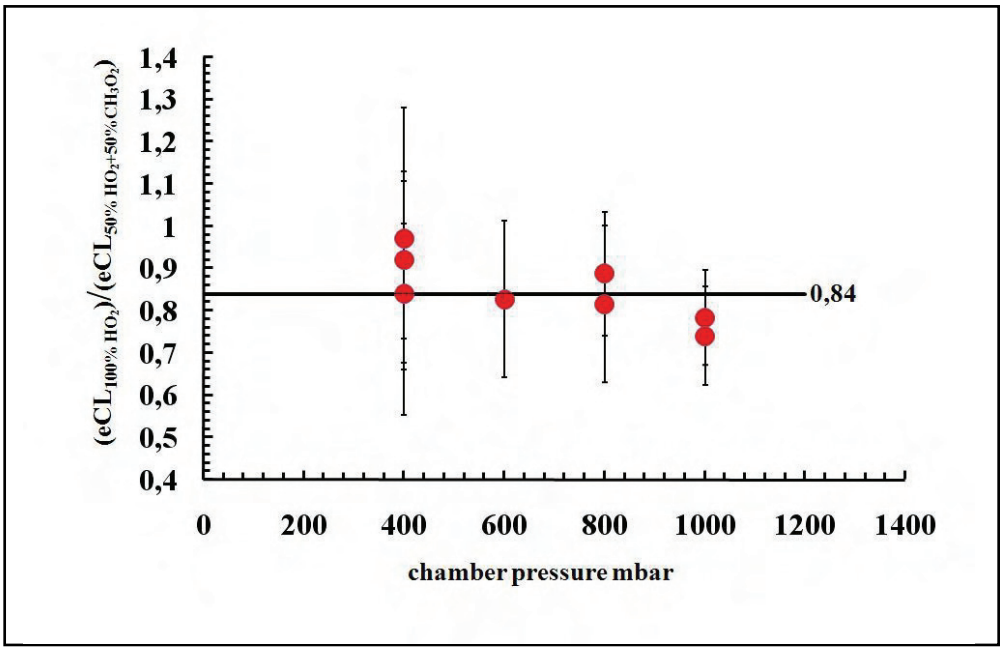

Figure 6.22 The eCL ratios determined for the calibration air containing 100% HO_2 and 50% CH_3O_2 , 50% HO_2 with pressure. 0,84 is the mean of all ratios.

The ratios of eCLs obtained at when the chamber is 400 mbar have larger error bars than ratios at higher chamber pressures due to the NO_2 detector response.

According to the loss % of CH_3O_2 and HO_2 loss calculated, the eCL was simulated at 300 mbar for radical mixtures containing different proportions of CH_3O_2 and HO_2. This enables the estimation of the error in RO_2^* determination in ambient measurements, which is associated to the assumption that all sampled peroxy radicals have the same wall losses. As can be seen in Figure 6.23 the eCL varies between 43 and 60 corresponding to pure HO_2 and pure CH_3O_2. According to these CH_3O_2 in the air sampled may increase the uncertainty of the RO_2^* determination with a relative error contribution to the total error below 25% and most likely between 8- 14%.

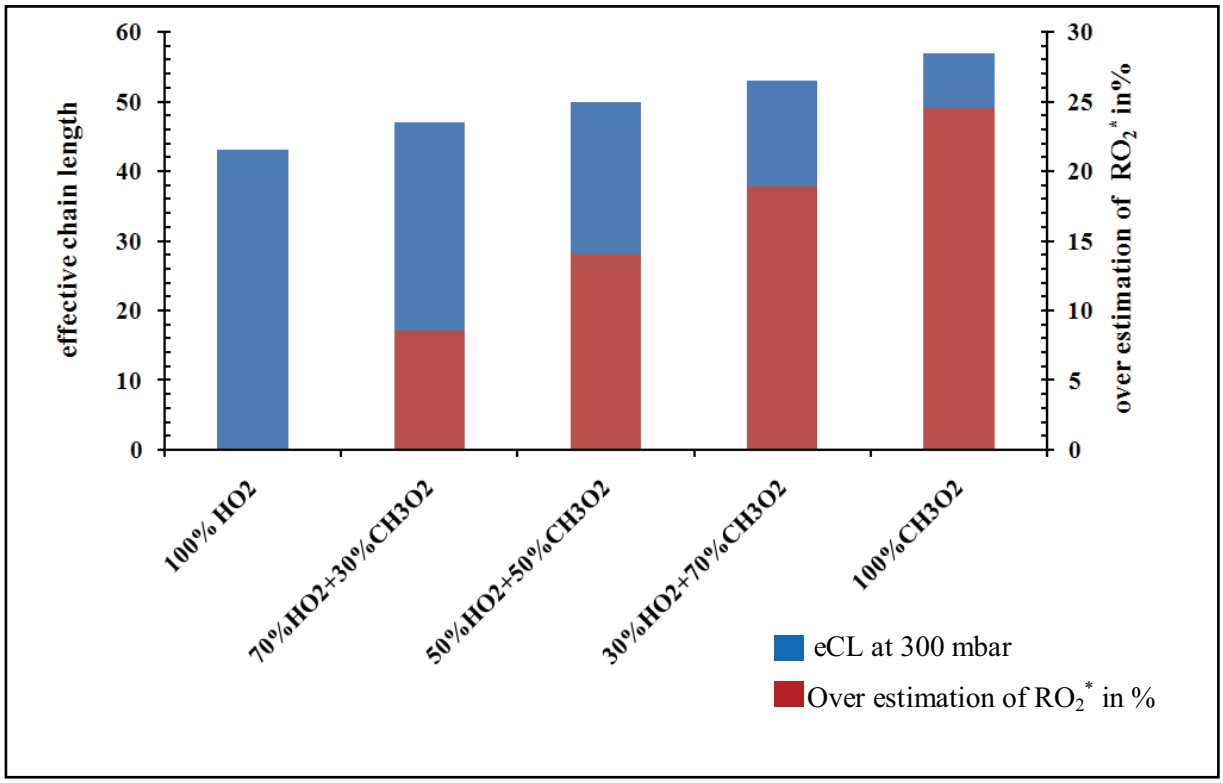

Figure 6.23 eCL values simulated for different mixtures of CH_3O_2 and HO_2 and the over estimation of the RO_2^* with the assumption that all sampled peroxy radicals have the same wall losses.

6.1.6 Application of laboratory experiment results

The characterization of the luminol detectors pointed out that the sensitivity is decreasing with decreasing pressure. The observations at changing the pressures rapidly affect the luminol flow to the filter paper that is related directly with the sensitivity of the detectors. By keeping the pressure constant at the measurement system by regulation enabled to achieve a constant sensitivity as the ambient pressure changes (see Figure 6.10).

The eCL represented in Figure 6.12 , 6.13 are obtained at the same operation conditions at the AMMA field campaign. The higher eCL values for 500 and 700 mbar at Figure 6.12 and the interpretation of this results (see section 6.1.3) requires the quantification of eCL according to ΔP ($\Delta P = P_{ambient} - P_{DUALER}$). The eCL result obtained for 200 mbar and 300 mbar are plotted against ΔP in figure 6.24.

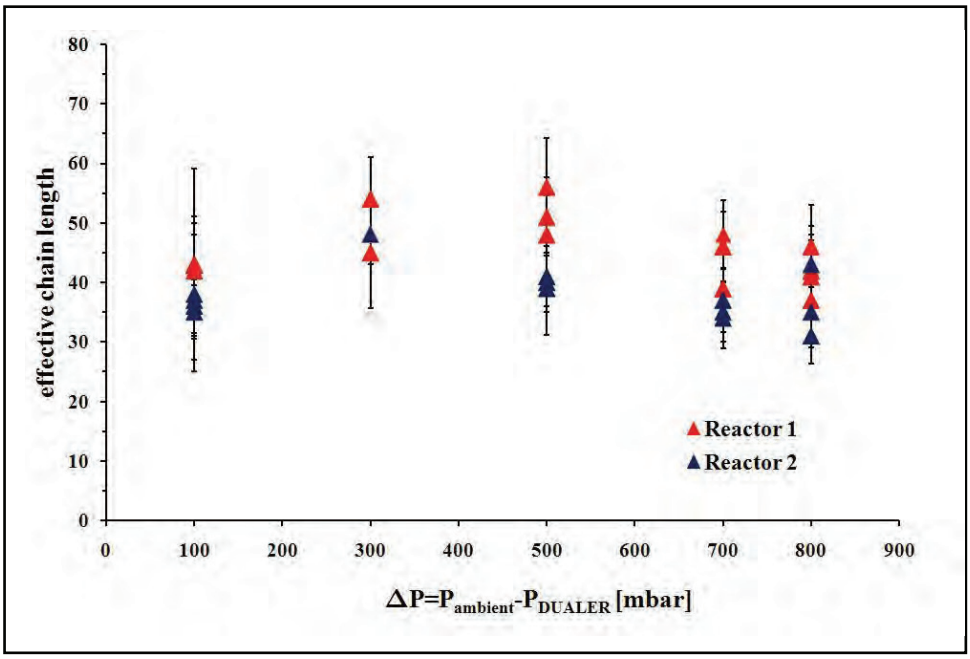

Figure 6.24 The eCL values versus ΔP (ΔP =Chamber pressure –DUALER$_{pressure}$)

Most of the flights during AMMA was under $\Delta P <$ 500 mbar. As it can be seen in Figure 6.24 the eCL variation presents a curvature which is at 500 mbar at maximum. The effect of ΔP is explained in section 6.1.4. These results imply that the performance of the instrument during airborne measurements is expected to be at the best for ΔP around 500 mbar.

6.2 Analysis of airborne measurements during AMMA 2006

An overview of the AMMA measurement campaign has been given in Chapter 5. The IUP-UB DUALER was deployed on the DLR-Falcon located in Burkina Faso for the measurement of peroxy radicals during the African monsoon period in August 2006.

The measurement conditions in Africa both during the preparation and measurement periods were often experimentally quite challenging and disrupt significantly the performance of the instruments. Regarding the measurement of peroxy radicals, following issues played an important role in the data quality.

First of all, during the AMMA flight preparation periods in Ouagadougou there were frequent and unavoidable interruptions in the gas flows and power supply previous to the flights which led to detector instabilities constraining the usefulness and representativeness of the calibrations.

In addition, changes in the NO_2 concentration of the gas cylinder built in the DUALER (1 ppm NO_2 in synthetic air) were observed along the day. These are attributed to the high temperature and humidity conditions prior to the flight which possibly led to variable NO_2 wall losses related to the formation of HNO_3 in the pressure regulator and the gas tubing in spite of lengthy flushing of the gas lines. As a consequence, the in-flight calibrations had to be supplemented by NO_2 calibrations of the detectors with external cylinders before and after the measurement flight.

During the flight, the effect of short-term instabilities in the luminol flow can be an important issue for the data analysis previous to the interpretation. The flow instabilities lead to short-term and not simultaneous variations in the sensitivities of the detectors which might introduce uncertainties in the determination of ΔNO_2, i.e., $NO_{2amplification}$–$NO_{2background}$, as it involves the signal of both single detectors.

To overcome most of these issues a mathematical method based on the ozone concentrations measured simultaneously on board the DLR- Falcon was developed for the interpretation of results (see Section 6.2.1). This procedure enables the monitoring of potential changes in the sensitivity of the detectors and the calculation of effective calibration parameters. In addition, the next sections describe the relative humidity effect in the airborne measurements, the error analysis for the determination of RO_2^*. Last section focuses on analysis of the measurements.

6.2.1 Determination of effective calibration parameters for monitoring detector sensitivities

As mentioned in the previous section, a methodology based on the comparison variation between the ozone mixing ratios measured by the ozone monitor at DLR-Falcon and the background signal of both detectors of the DUALER was developed to monitor potential changes in the sensitivity of the detectors during the flight.

The principal assumption of the method is that the signal of the NO_2 detectors in the background modus, i.e., when no conversion of radicals is taking place (see section 1.4.4.) corresponds to the measurement of ambient O_3. As NO 3ppm is added to the reactors, the ambient ozone is converted one to one into NO_2. Variations of NO_2 and other gases potentially contributing to the background signal have a negligible effect in general.

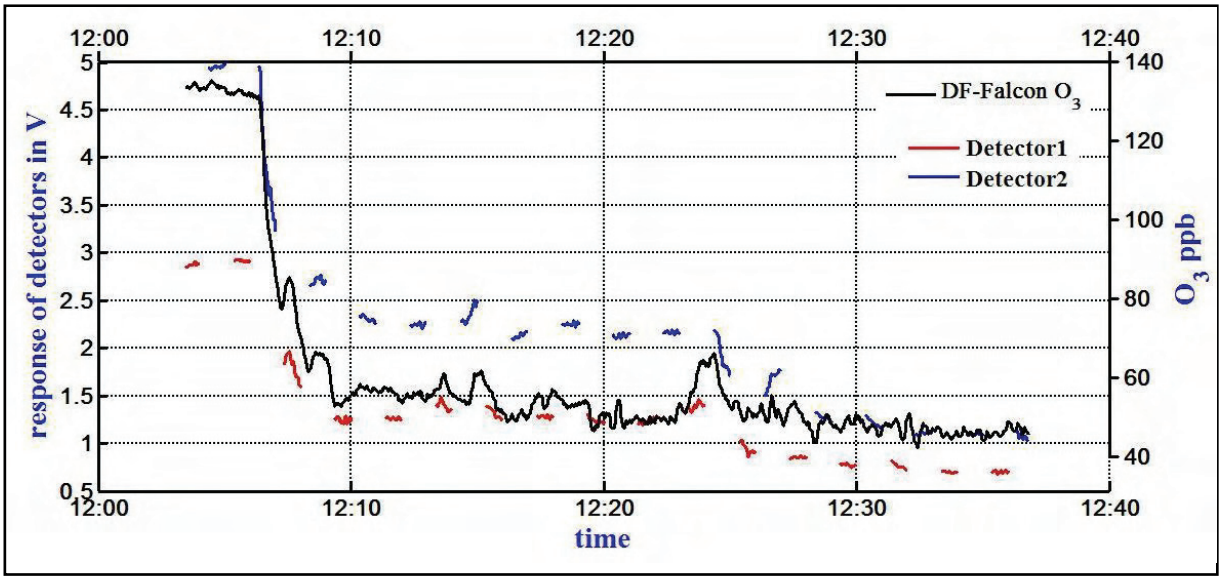

Figure 6.25 Comparison of the variation of ozone and raw voltage signals of the DUALER detectors during a AMMA flight.

In the Figure 6.25 is exemplary depicted the comparison of the O_3 and NO_2 detector background signals obtained in one of the flights performed during the AMMA campaign. As can be seen in Figure 6.25 the detectors have different sensitivities but they follow the changes of ozone mixing ratios very well.

The idea of the method is to calculate a sensitivity array for a response value (X_k in volts,k=1…n) at a *k* second of the interval by comparing the X_k value and the corresponding ozone mixing ratio with the rest of the values of a time interval, as shown schematically in Figure 6.26. As the detector response is linear, the ratio of the difference of ozone mixing ratio and the difference of the response as voltage for the corresponding mixing ratios should be constant. For this, the data of each flight are divided in time intervals, which are variably selected, in order to optimally consider the main O_3 features in the comparison. Generally each time interval corresponds to the measurement within a pressure level during the flight.

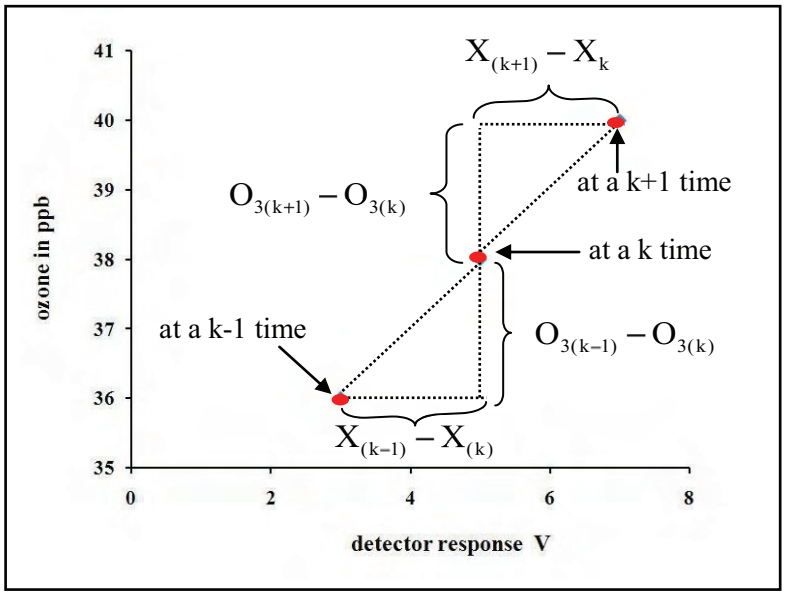

Figure 6.26 Principle for the comparison between the response of the NO_2 detectors and the measured ozone mixing ratios.

The comparison of the ozone mixing ratios and detector responses at a *k* time and *k+1* and *k-1* can be expressed mathematically as:

$$O_{3(k)} - O_{3(k+1)} = (a_k * X_{(k)} + b_1) - (a_k * X_{(k+1)} + b_1) = a_k * (X_{(k)} - X_{(k+1)})$$

$$a_k = \frac{O_{3(k)} - O_{3(k+1)}}{X_{(k)} - X_{(k+1)}} \qquad (6.16)$$

In an analogous manner, an array with n-1 elements is obtained for each point measured at the time k, being n the number of measurement points within a selected time interval. An array of the linear parameter of '*a*' can be obtained by comparing the reference response X_k at a k time with the whole responses in the time interval:

$$\begin{bmatrix} a_{k(1)} \\ a_{k(2)} \\ . \\ . \\ a_{k(k-1)} \\ a_{k(k+1)} \\ . \\ . \\ a_{k(n)} \end{bmatrix} = \frac{\left(\begin{bmatrix} O_{3(1)} \\ O_{3(2)} \\ . \\ . \\ O_{3(k-1)} \\ O_{3(k+1)} \\ . \\ . \\ O_{3(n)} \end{bmatrix}_{(n-1)x1} - \left[O_{3(k)} \right] \right)}{\left(\begin{bmatrix} X_{(1)} \\ X_{(2)} \\ . \\ . \\ X_{(k-1)} \\ X_{(k+1)} \\ . \\ . \\ X_{(n)} \end{bmatrix}_{(n-1)x1} - \left[X_{(k)} \right] \right)} = \frac{\left(\begin{bmatrix} O_{3(1)} - O_{3(k)} \\ O_{3(2)} - O_{3(k)} \\ . \\ . \\ O_{3(k-1)} - O_{3(k)} \\ O_{3(k+1)} - O_{3(k)} \\ . \\ . \\ O_{3(n)} - O_{3(k)} \end{bmatrix} \right)}{\left(\begin{bmatrix} X_{(1)} - X_{(k)} \\ X_{(2)} - X_{(k)} \\ . \\ . \\ X_{(k-1)} - X_{(k)} \\ X_{(k+1)} - X_{(k)} \\ . \\ . \\ X_{(n)} - X_{(k)} \end{bmatrix} \right)} = \begin{bmatrix} (O_{3(1)} - O_{3(k)}) / (X_{(1)} - X_{(k)}) \\ (O_{3(2)} - O_{3(k)}) / (X_{(2)} - X_{(k)}) \\ . \\ . \\ (O_{3(k-1)} - O_{3(k)}) / (X_{(k-1)} - X_{(k)}) \\ (O_{3(k+1)} - O_{3(k)}) / (X_{(k+1)} - X_{(k)}) \\ . \\ . \\ (O_{3(n)} - O_{3(k)}) / (X_{(n)} - X_{(k)}) \end{bmatrix} \tag{6.17}$$

Thus, a sensitivity array is attributed to each NO_2 measuring point of a luminol detector, being $S^*_{(k)} = 1 / a^*_{(k)}$ the mean value of the sensitivity of the detector at one point for a selected time interval.

$$a^*_{(k)} = \text{mean} \left(\begin{bmatrix} a_{(1)} \\ a_{(2)} \\ . \\ a_{(k-1)} \\ a_{(k+1)} \\ . \\ a_{(n)} \end{bmatrix}_{(n-1)x1} \right) \tag{6.18}$$

Conversely, the value b can be calculated for each measurement point as:

$$\left(\begin{bmatrix} O_{3(1)} \\ O_{3(2)} \\ . \\ . \\ O_{3(k)} \\ O_{3(k+1)} \\ . \\ . \\ O_{3(n)} \end{bmatrix}_{nx1}\right) - \left(\begin{bmatrix} a^*_{(1)} * X_{(1)} \\ a^*_{(2)} * X_{(2)} \\ . \\ . \\ a^*_{(k)} * X_{(k)} \\ a^*_{(k+1)} * X_{(k+1)} \\ . \\ . \\ a^*_{(n)} * X_{(n)} \end{bmatrix}_{nx1}\right) = \begin{bmatrix} b^*_{(1)} \\ b^*_{(2)} \\ . \\ . \\ b^*_{(k)} \\ b^*_{(k+1)} \\ . \\ . \\ b^*_{(n)} \end{bmatrix}_{nx1} \tag{6.19}$$

Therefore, a value of a^*_k and b^*_k are assigned to each detector signal. The variability of these parameters indicates the sensitivity variations of the detectors (see Figure 6.27 and Figure 6.28).

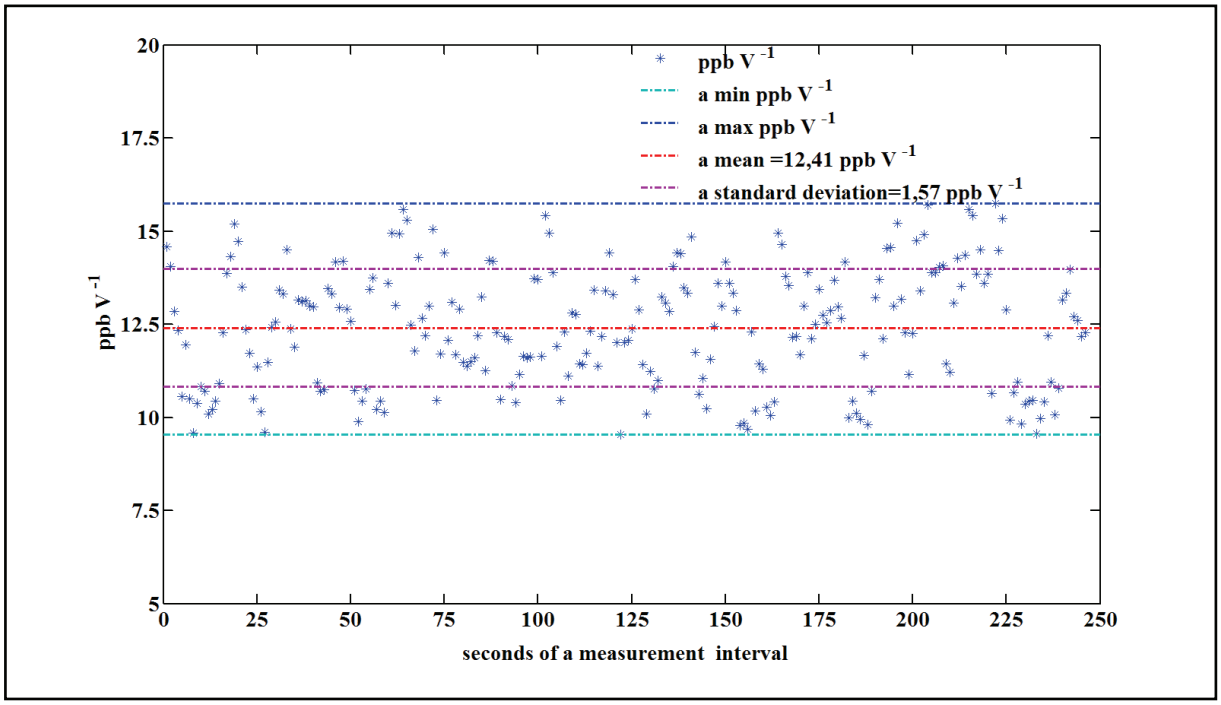

Figure 6.27 Example of variation of '*a*' during a measurement interval; $[NO_2]=aX+b$

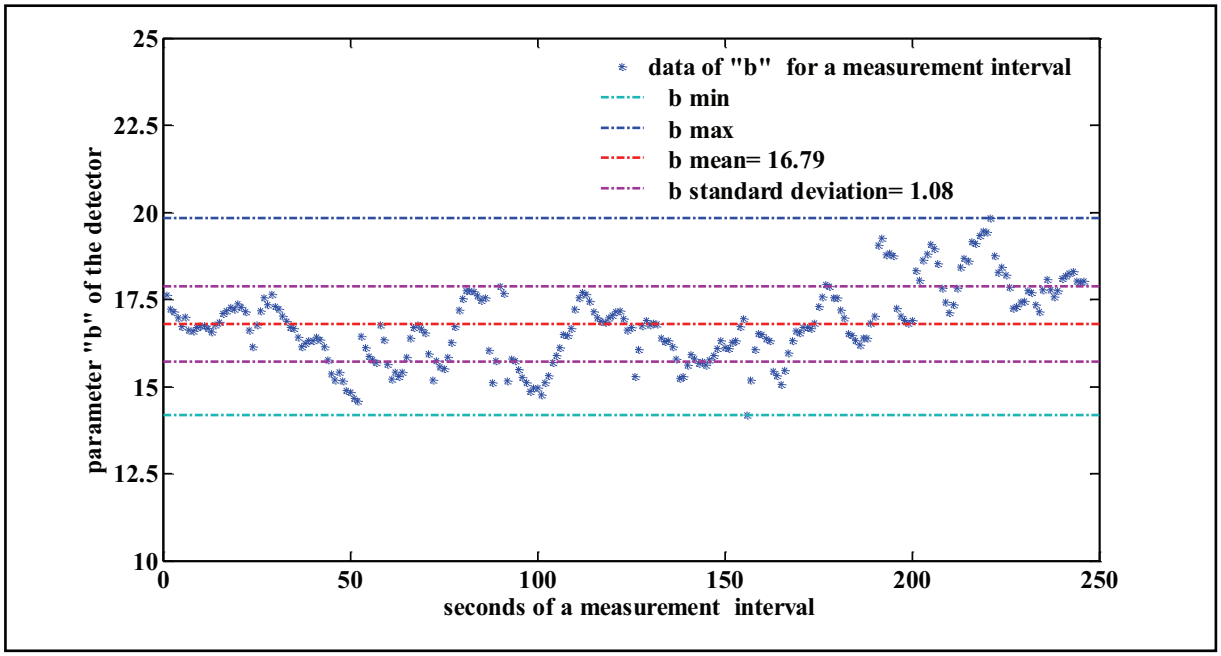

Figure 6.28 Example of variation of *'b'* during a measurement interval; $[NO_2]=aX+b$

In figure 6.27 and 6.28 the variation of the *a* parameter can be seen, most of the values are within 1σ. The length of the interval in the example is 4 minutes and generally depends on the stabilization of the detector. The A parameter, i.e., the mean of a is 12.41 $ppbV^{-1}$ and the standard deviation 1.57 $ppbV^{-1}$ which leads to a relative error 12.5%. In figure 6.27 the relative error of B is 6.5%.

The values obtained are defined as effective calibration parameters, these parameters are more adequate for the data processing of the airborne measurements than the calibration parameters obtained previous or after the flights as they consider potential in -flight variations of the sensitivity of the detectors.

The effective calibration parameters are further used to calculate the mixing ratios of the peroxy radicals at a time *k* within each time period selected:

$$\begin{aligned} NO_{2\,amplification.modus} &\Rightarrow A_{Det_1} * X_{1(1....k.....n)} + B_{Det_1}; \\ NO_{2\,background.modus} &\Rightarrow A_{Det_2} * X_{2(1....k.....n)} + B_{Det_2}; \\ \text{or} & \\ NO_{2\,amplification.modus} &\Rightarrow A_{Det_2} * X_{1(1....k.....n)} + B_{Det_2}; \\ NO_{2\,background.modus} &\Rightarrow A_{Det_1} * X_{2(1....k.....n)} + B_{Det_1}; \end{aligned} \qquad (6.20)$$

being,

$$A_{Det_1} = \text{mean}\left(\begin{bmatrix} a^*_{1(1)} \\ a^*_{1(2)} \\ . \\ a^*_{1(k)} \\ a^*_{1(k+1)} \\ . \\ a^*_{1(n)} \end{bmatrix}\right);\ B_{Det_1} = \text{mean}\left(\begin{bmatrix} b^*_{1(1)} \\ b^*_{1(2)} \\ . \\ b^*_{1(k)} \\ b^*_{1(k+1)} \\ . \\ b^*_{1(n)} \end{bmatrix}\right);$$

$$A_{Det_2} = \text{mean}\left(\begin{bmatrix} a^*_{2(1)} \\ a^*_{2(2)} \\ . \\ a^*_{2(k)} \\ a^*_{2(k+1)} \\ . \\ a^*_{2(n)} \end{bmatrix}\right);\ B_{Det_2} = \text{mean}\left(\begin{bmatrix} b^*_{2(1)} \\ b^*_{2(1)} \\ . \\ b^*_{2(k)} \\ b^*_{2(k+1)} \\ . \\ b^*_{2(n)} \end{bmatrix}\right);$$

$$\begin{aligned} RO^*_{2(reactor1)} &= \frac{\Delta NO_2}{eCL_{reactor1}} \Rightarrow \frac{A_{Det1} * X_{1(k)} - A_{Det2} * X_{2(k)} + (B_{Det1} - B_{Det2})}{eCL_{reactor1}} \\ RO^*_{2(reactor2)} &= \frac{\Delta NO_2}{eCL_{reactor2}} \Rightarrow \frac{A_{Det2} * X_{2(k)} - A_{Det1} * X_{1(k)} + (B_{Det2} - B_{Det1})}{eCL_{reactor2}} \end{aligned} \tag{6.21}$$

The corresponding eCL for the reactors are determined in the laboratory as presented in section 6.1.3.

6.2.2 Effect of relative humidity in the DUALER measurements during AMMA

The dependency of CL of PERCA technique on relative humidity (Mihele et al., [1999]; Reichert et al., [2003]) is explained in section 1.4.4.2. The relative humidity measurements taken by DUALER are not representative for the sampled air due the location of the relative humidity sensor in the instrument close to the detector (see section 3.5). During the flights the temperature of the reactors are measured and recorded manually. The corresponding relative humidity is recalculated by the use of the DLR-Falcon measurements.

During the AMMA measurements the reactors are at a higher temperature than the ambient temperatures, and the DUALER pressure is always lower than the ambient pressure ($T_{ambient}<T_{reactors}$; $P_{ambient}> P_{DUALER}$). At this situation the relative humidity inside the DUALER is expected to be lower than the ambient relative humidity. The relative humidity is defined as:

$$\text{RelativeHumidity} = \frac{P_{partial}}{P_{saturation}} \cdot 100 \tag{6.22}$$

The partial pressure of water vapour ($P_{partial}$) is the ratio between the mixing ratio of water vapour and the total pressure. As the mixing ratio of the water vapour is not changing in the sampled gas but the total DUALER pressure is less than ambient pressure, the $P_{partial}$ of water decreases in the DUALER.

The saturation pressure of the water vapour is a function of temperature and increases with increasing temperature. The saturation pressure of water vapour is increasing as the temperature at the DUALER is higher. As a result the relative humidity decreases in the DUALER.

To further quantify this situation a series of calculations are done. The temperatures measured for the reactors at the commonly flown pressure levels are compared with ambient temperatures, and a function is fitted (see Figure 6.29).

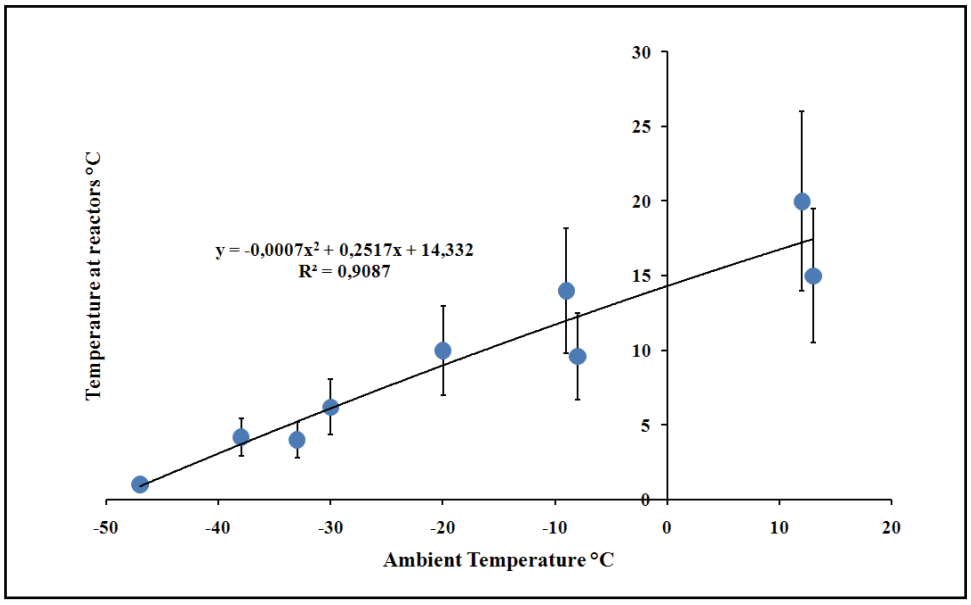

Figure 6.29 Measured reactor temperatures at different ambient temperatures corresponding to different pressure levels.

By using the fit function in Figure 6.29 the reactor temperatures are calculated on the basis of the ambient temperatures measured. To calculate the relative humidity in the DUALER by using the formula (6.22), the mixing ratio of water vapour in ambient air and the saturation vapour pressure for the reactors are required. For this the dew point, relative humidity, ambient pressure, and temperature measurements of the DLR-Falcon are used.

The ambient temperature measurements of DLR-Falcon are used to calculate the ambient saturation water vapour pressure with the formula (Laube and Höller, 1988) for the saturation vapour pressure over liquid water:

$$\begin{aligned}\log_{10} e_{sat\,w} = {} & 10,79574\cdot(1-T_t/T) - 5,028\cdot\log_{10}(T/T_t) \\ & + 1,50475\cdot10^{-4}\cdot(1-10^{(-8,2969\cdot(T/T_t-1))}) \\ & + 0,42873\cdot10^{-3}\cdot(10^{(4,76955(1-T_t/T))}-1) \\ & + 0,78614\end{aligned} \tag{6.23}$$

where T_t=273,16 K , $e_{sat\,w}$ is expressed in hPa, and 223K<T<373K,

and for the saturation vapour pressure over ice:

$$\begin{aligned}\log_{10} e_{sat,i} = {} & -9,09685\cdot(T_t/T-1) - 3,56654\cdot\log_{10}(T_t/T) \\ & + 0,87682\cdot(1-T/T_t) + 0,78614\end{aligned} \tag{6.24}$$

where T_t=273,16 K, $e_{sat\,i}$ is expressed in hPa, and 173K<T<273,15K.

Once the saturation water vapour pressure is calculated, the water vapour mixing ratio can be calculated like:

$$[H_2O] = \frac{RH_{DLR-Falcon} \cdot P_{saturation}}{P_{ambient}} \tag{6.25}$$

Where $P_{ambient}$ the ambient pressure, $RH_{DLR\text{-}Falcon}$ the relative humidity measured by DLR-Falcon sensor, and $P_{saturation}$, is the saturation water vapour pressure calculated by the formulas(6.23),(6.24) by using temperature measurements of DLR-Falcon.

As the mixing ratio is known, the saturation water vapour for the temperature of the reactors is calculated by the formula (6.23), the pressure in DUALER is constant (200 or 300mbar), the DUALER relative humidity can be calculated as following;

$$RH_{DUALER} = \frac{[H_2O] \cdot P_{DUALER}}{P_{saturation\ at\ DUALER}} = \frac{P_{partial\ DUALER}}{P_{saturation\ at\ DUALER}} \tag{6.26}$$

Figure 6.30 shows exemplary the variation of the calculated relative humidity of DUALER for a flight during AMMA and compares it with the relative humidity of DLR-Falcon measurements.

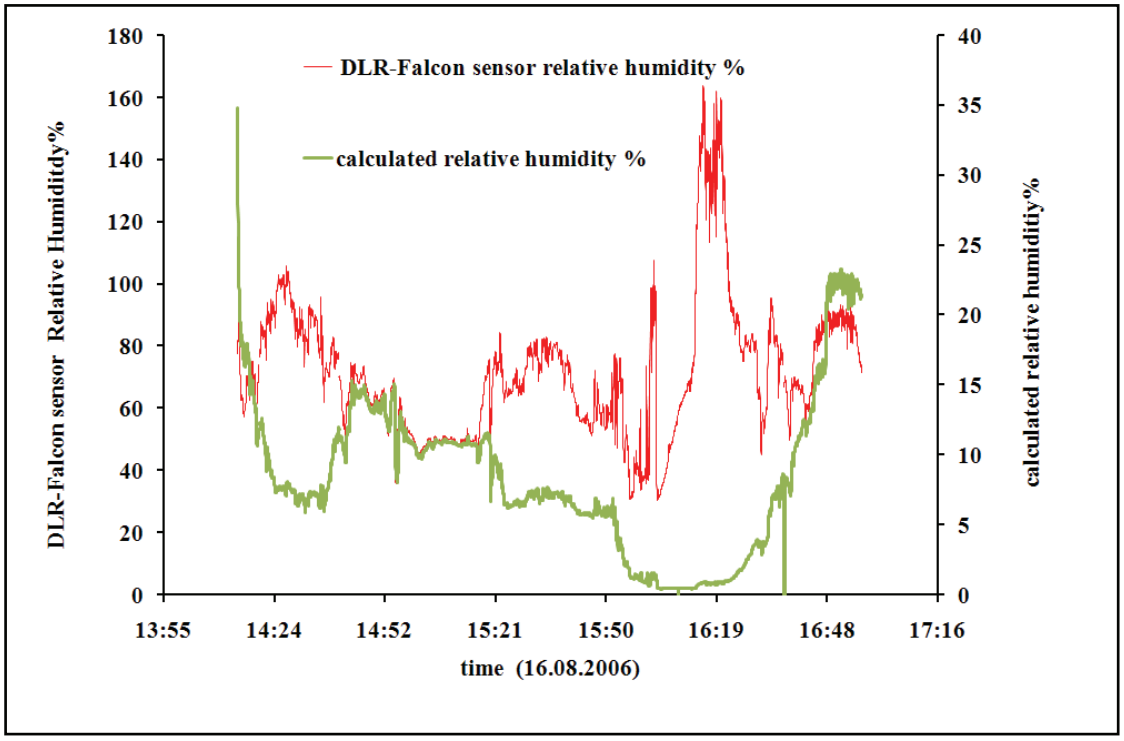

Figure 6.30 Comparison between ambient and DUALER relative humidity.

The differences in the relative humidity are caused by the smaller partial pressure of the water and/or the higher saturation water vapour in DUALER respect to the ambient. In some cases the reduction in the partial pressure of water is the dominating reason, in some cases the increase in the saturation water vapour pressure. For example, in Figure 6.30 around 14:24 hours, both factors are playing a significant role as shown in Figure 6.31 and Figure 6.32.

Around 16:19 hours the saturation water vapour pressure is the important factor as the difference of DUALER pressure and ambient pressure is lower. At the lower flight level around 16:48 hours the difference between the saturation water vapours of ambient and DUALER is lower. The partial pressure is the dominant factor. This is confirmed by the 4 times decrease in the relative humidity for a $P_{ambient}/P_{DUALER\ (200\ mbar)}$ ratio of 4.5 (see Figure 6.30, 6.31, 6.32).

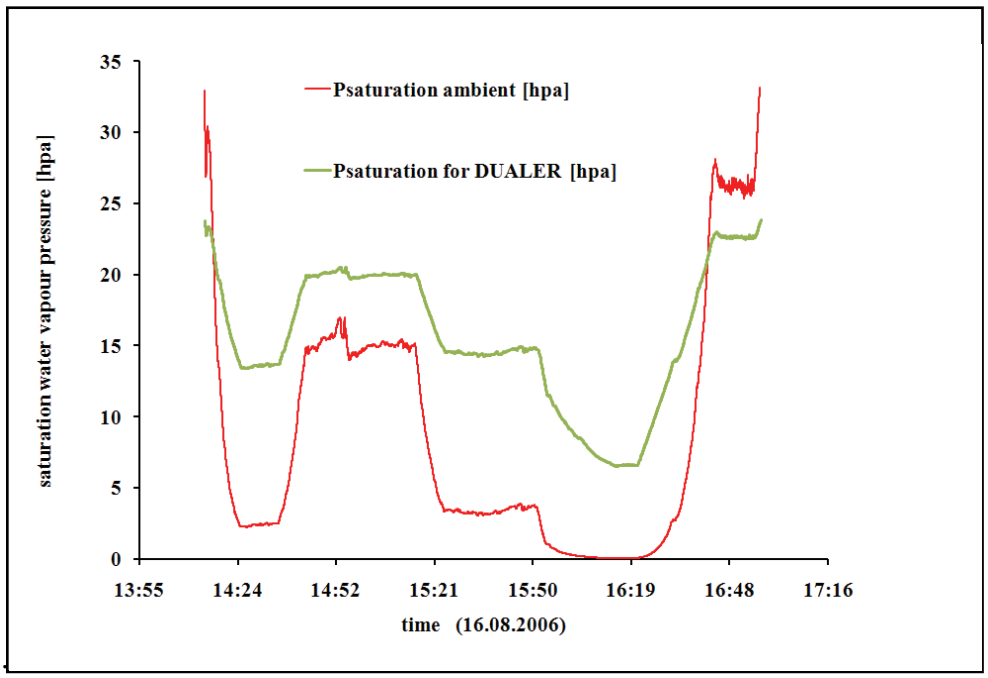

Figure 6.31 Comparison of calculated saturation water vapour pressures for DUALER and ambient.

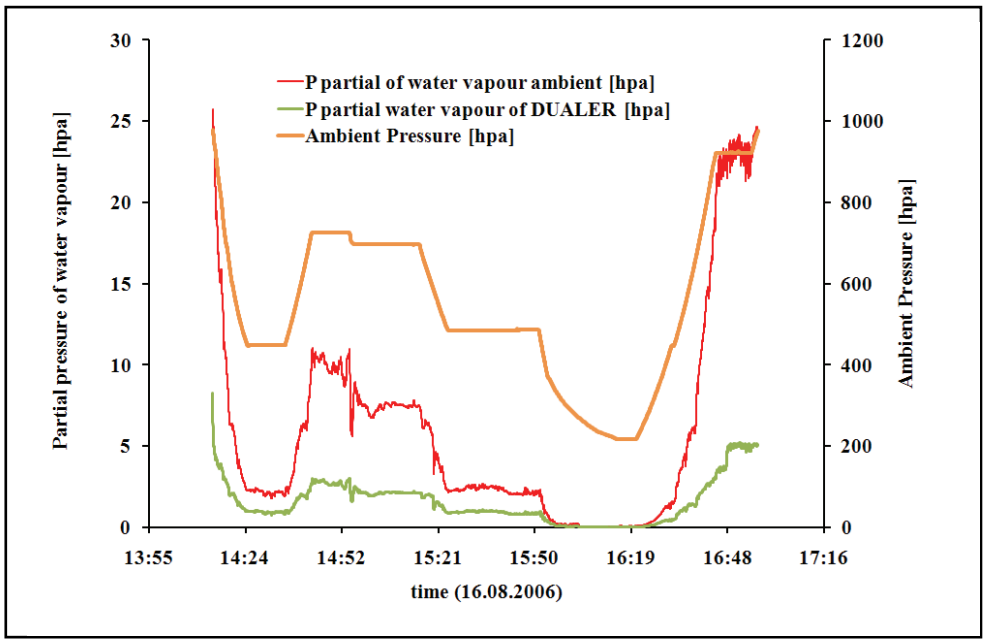

Figure 6.32 Comparison of calculated water vapour partial pressures for DUALER and ambient. The flight pressures are also depicted.

These results indicate that at pressures above 750 mbar the relative humidities in the DUALER are not significantly different to the RH used for the calibrations of the eCL in the laboratory and therefore no correction is necessary. This is the case of most of the flights performed during AMMA.

For flown altitudes below 750 mbar the RH at the DUALER remained generally between 10 and 15%. The influence of the relative humidity in the eCL has not been characterised within this work but estimated on the basis of the results from previous experiments with other reactors. In those, the reduction in the CL at relative humidity between 5% and 15% is around 10% (Reichert et al., 2003). As the DUALER is calibrated at RH between 3-6% this estimation is used in the calculation of the error associated to the corresponding measurements at higher pressures.

6.2.3 Error analysis of the airborne RO_2^* measurements

A main contribution to the error of the DUALER airborne measurements of RO_2^* is the error of the NO_2 detector response parameters determined with the mathematical method explained above. In addition, the error of eCL calculated by the experimental results in the laboratory must be taken into account (see section 3.4). As mentioned in 6.2.2 for measurements taken at pressures above 750 mbar the effect of the relative humidity in the eCL has a further contribution to the relative error around 10%.

As presented in the section 6.2.1, the RO_2^* mixing ratios are calculated from:

$$\begin{aligned} RO^*_{2(reactor1)} &= \frac{\Delta NO_2}{eCL_{reactor1}} \Rightarrow \frac{A_{Det1} * X_{1(k)} - A_{Det2} * X_{2(k)} + (B_{Det1} - B_{Det2})}{eCL_{reactor1}} \\ RO^*_{2(reactor2)} &= \frac{\Delta NO_2}{eCL_{reactor2}} \Rightarrow \frac{A_{Det2} * X_{2(k)} - A_{Det1} * X_{1(k)} + (B_{Det2} - B_{Det1})}{eCL_{reactor2}} \end{aligned} \tag{6.21}$$

The equation (6.21) can be expressed like this;

$$RO^*_2 = \frac{A_{Det1} * X_1}{eCL_1} - \frac{A_{Det2} * X_2}{eCL_1} + \frac{B_{Det2}}{eCL_1} - \frac{B_{Det1}}{eCL_1} \tag{6.27}$$

Thus;

$$\sigma_{RO^*_2} = \sqrt{\left(\sigma_{\frac{A_{Det1}*X_1}{eCL}}\right)^2 + \left(\sigma_{\frac{A_{Det2}*X_2}{eCL}}\right)^2 + \left(\sigma_{\frac{B_{Det2}}{eCL}}\right)^2 + \left(\sigma_{\frac{B_{Det1}}{eCL}}\right)^2} \tag{6.28}$$

For the general error calculations the error contribution from the detector parameters are assumed to be equal;

$$\sigma_{RO^*_2} = \sqrt{2\left(\left(\sigma_{\frac{A_{Det}*X}{eCL}}\right)^2 + \left(\sigma_{\frac{B_{Det}}{eCL}}\right)^2\right)} \tag{6.29}$$

To calculate the relative error of the RO_2^*, the relative error of the components of equation (6.29) ; $\frac{A_{Det}*X}{eCL}$ and $\frac{B_{Det}}{eCL}$ can be calculated as follows;

$$\frac{\sigma_{\frac{A_{Det}*X}{eCL}}}{\frac{A_{Det}*X}{eCL}} = \sqrt{\left(\frac{\sigma_{A_{Det}}}{A_{Det}}\right)^2 + \left(\frac{\sigma_x}{x}\right)^2 + \left(\frac{\sigma_{eCL}}{eCL}\right)^2} \tag{6.30}$$

$$\frac{\sigma_{\frac{B_{Det}}{eCL}}}{\frac{B_{Det}}{eCL}} = \sqrt{\left(\frac{\sigma_{B_{Det}}}{B_{Det}}\right)^2 + \left(\frac{\sigma_{eCL}}{eCL}\right)^2} \quad (6.31)$$

The relative error of eCL is 15% (see section 3.4), the relative error of the response of detectors as voltage is 1% , and the relative error of the response parameters (A_{Det} and B_{Det}) are between 10%-20% according the performance of the detectors during the AMMA measurements which depends on the luminol flow stability.

The method used to determine the response parameters considers a 5% uncertainty of the ozone mixing ratios, so the variations of the NO_2 detector parameters represent these uncertainties. As the laboratory experiments showed, the reproducibility of the sensitivity is within 99% measurements taken with the same filter and under the same pressure conditions and sensitivity do not change at different ambient pressures.

The principal contribution of error to the A_{det} and B_{det} is coming from deviations of ozone mixing ratios and from the luminol flow instabilities. The variation of the A_{Det} and B_{Det} parameters can exemplary be seen in Figure 6.33 to Figure 6.36 determined with the methodology described in section 6.2.1. For this particular case the relative error contributions of all these parameters can be used to calculate the relative error of the RO_2^* measurements as follows by using the equations(6.29), (6.30), (6.31):

$$\frac{\sigma_{RO_2^*}}{RO_2^*} \cdot 100 = \sqrt{2 * \left[((0.15)^2 + (0.01)^2 + (0.15)^2) + ((0.05)^2 + (0.15)^2) \right]} \cdot 100 \Rightarrow 37\% \quad (6.32)$$

The relative error of RO_2^* remain between 25% and 45% in the whole measurement period of AMMA. As the O_3 variability has a significant effect in the accuracy of the method, the error must be calculated separately for each time interval selected.

In addition, this method might be subject to a certain error in the case of malfunction of the O_3 instrument and/or sudden variations of background ambient gases other than O_3 oxidising NO or providing directly NO_2 to the DUALER. However, the analysis of the variations in ambient NO and NO_2 within the periods selected for analysis does not indicate to that these are significant source of error in the determination of the effective calibration parameters. Other potential source of additional uncertainty is the effect of aerosols and clouds in radical losses prior to the reactors. This error can only be qualitatively estimated by careful interpretation of the measurement conditions of each particular flight.

The error calculated in (6.32) corresponds to the RO_2^* measurements on 4 August 2006 at 315 mbar presented in Figure 6.37. It is flown through a convection zone as indicated by the NO and NO_y variability. The presence of clouds introduces an additional source of radical variability to this complex local chemistry. However, the general smooth O_3 variations minimize the error associated to the RO_2^* validation algorithm.

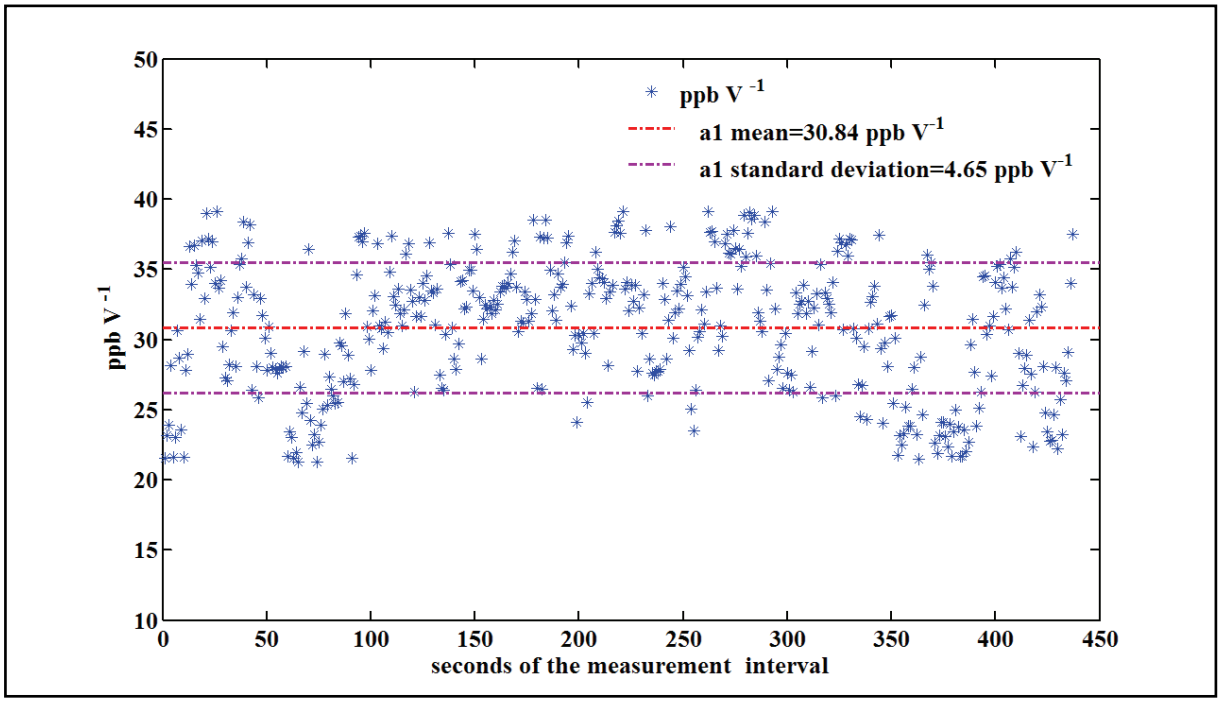

Figure 6.33 Exemplary plot for the variation of the *a* parameter for the detector1 of the DUALER

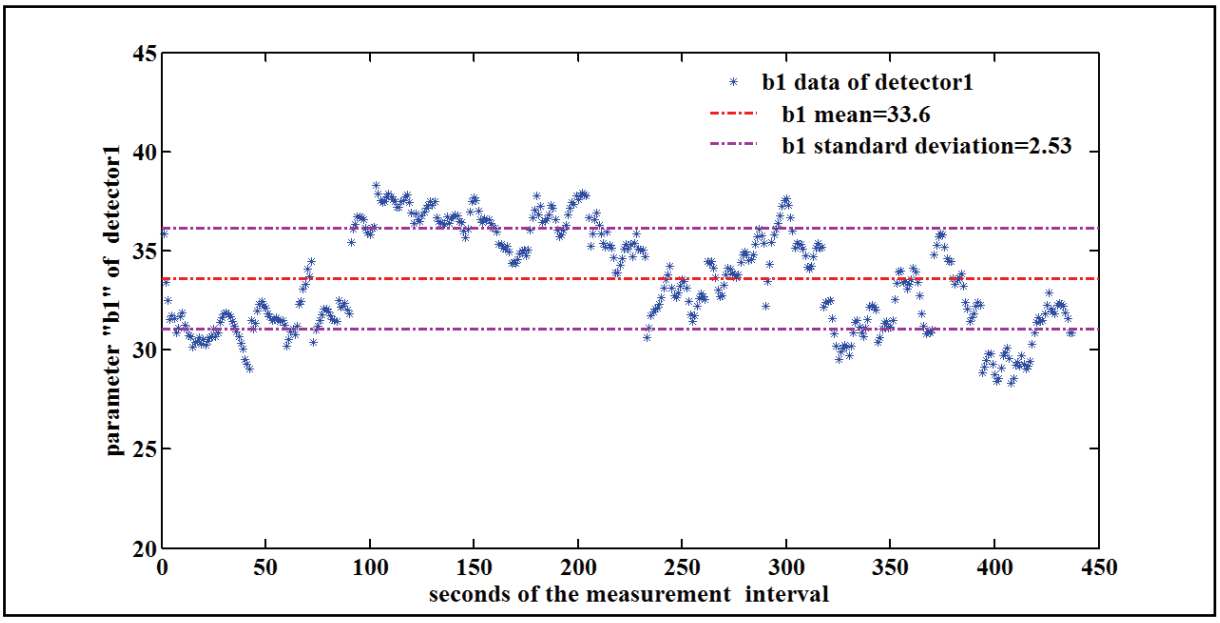

Figure 6.34 Exemplary plot for the variation of *b* parameter for the detector1 of the DUALER

As can be seen from Figure 6.33 to 6.36 the length of the interval selected is different for each detector. This is due to the instabilities of luminol flow during the flight which is different for each detector. The corresponding data for these instabilities are filtered. For detector1 in Figure 6.33 for the DUALER the variation of the values used to obtain the mean A1 is within 1σ and has a relative error of 15%. In Figure 6.34 the *b* are not as scattered as *a* due to the determination procedure ("*b*" is determined as O_{3k}-a_kX_k), and the B1 has a relative error of 7%. The A2 and B2 parameters for detector 2 have a relative error of 16% and 5% respectively.

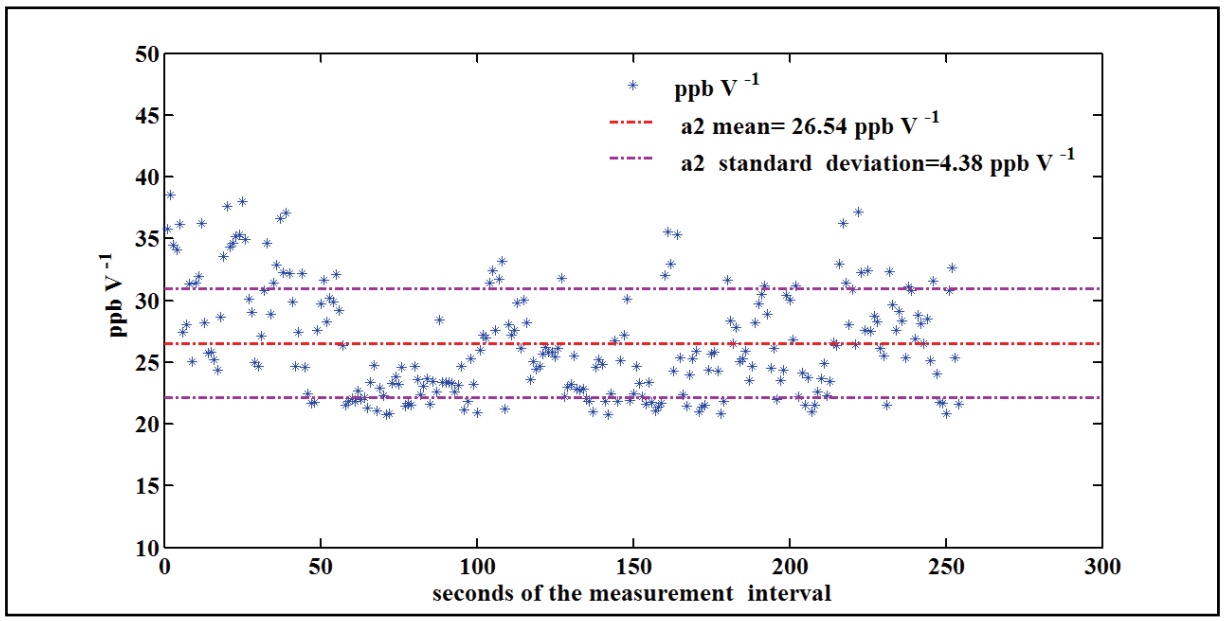

Figure 6.35 Exemplary plot for the variation of a parameter for detector2 of DUALER

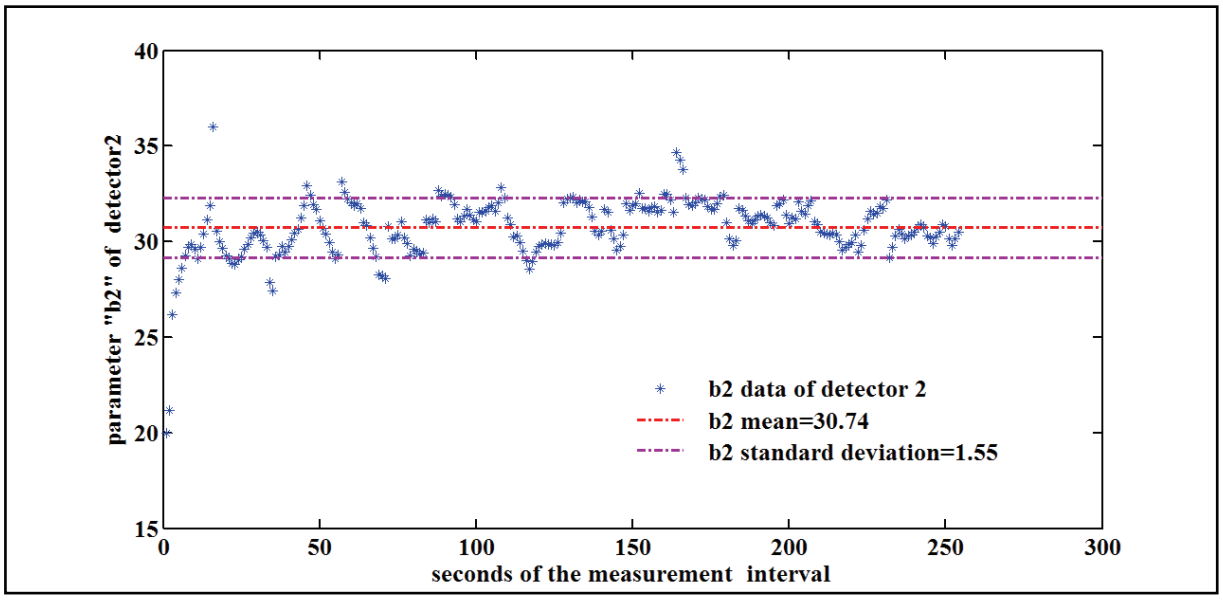

Figure 6.36 Exemplary plot for the variation of B parameter for detector2 of DUALER

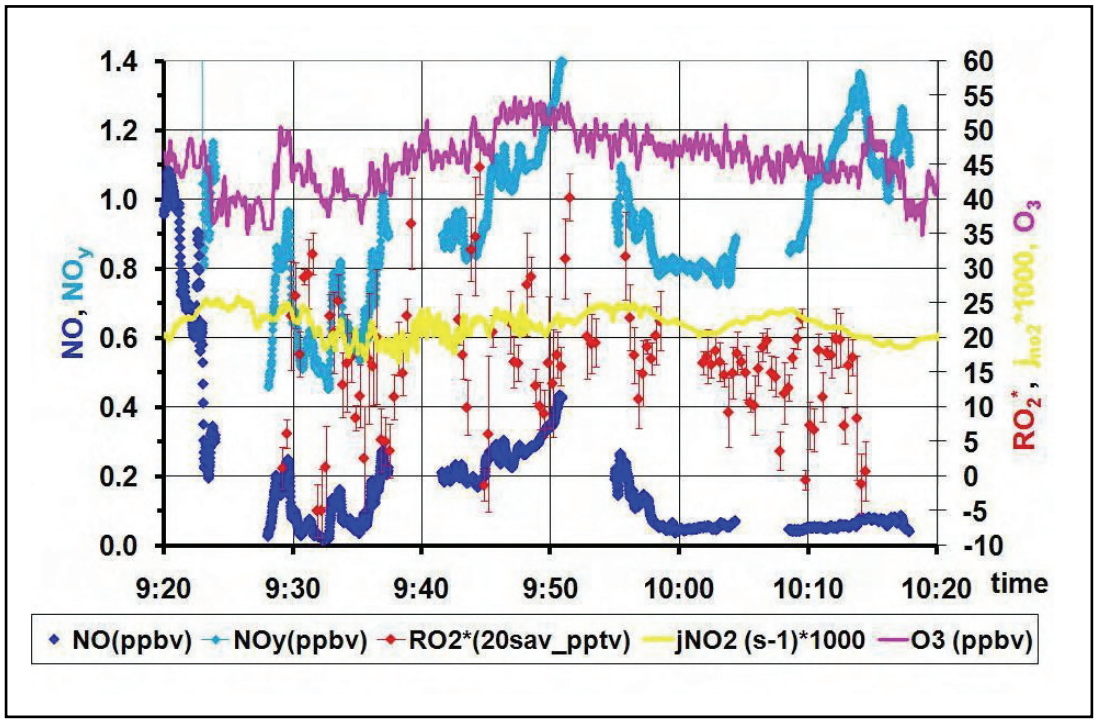

Figure 6.37 Measurement interval corresponding to the parameters variations shown in figures 6.33 to 6.36.

6.2.4 Analysis of peroxy radical measurements during AMMA

In the following text the peroxy radicals obtained during AMMA will be described and interpreted. Air masses of different photochemical activity were sampled during the SOP2 campaign. Therefore, the analysis of the measurements is grouped in three sections:

- RO_2^* measurements within convective episodes
- RO_2^* measurements within biomass burning plumes
- Vertical distribution of RO_2 over Ouagadougou

The analyses of the air masses undertaken in this study uses measurements of other constituents and parameters made on board the DLR- Falcon. These data are provided by the DLR-Institute of Atmospheric Physics. O_3 and CO_2 were measured using UV and IR absorption techniques, respectively (Schlager et al., 1997; Schulte et al., 1997). CO was detected with an UV fluorescence instrument (Gerbig et al., 1996). Reactive nitrogen compounds (NO, NO_y) were measured using two O_3/NO-chemiluminescence detectors and a gold converter for reduction of higher oxidized NO_y compounds to NO (Schlager et al., 1997; Ziereis et al., 2000). Formaldehyde, HCHO, was detected by a fluorometric technique (Hantzsch reaction). Characteristics of the instruments (accuracies, detection limits) are summarized in (Reeves et al., 2009). In addition clusters of 72h back trajectories launched in the vicinity of the aircraft location using the FLEXTRA model (Stohl et al., 1995; 1998) were consulted to gain additional information about the origin of the air masses sampled within the case studies (Andrés Hernández et al., 2009).

6.2.4.1 RO_2^* measurements within convective episodes

Data obtained during the first flight on the 15.08.06 are depicted in Figure 6.38 a, b, c. The objective of the flight was to measure the outflow of a MCS located over Mali after passing Ouagadogou the evening before. The DLR-Falcon reached this outflow area at the 287 mbar pressure level.

The NO_y and NO_x data measured during the flight (Figure 6.38 b) are high variable between 0.4-1.6 ppbv and 0.2-1 ppbv. This high variability is a typical signature for convective outflows.

The CO mixing ratios remain around 100- 110 ppbv, about 20 ppbv higher than outside the outflow area. O_3 remains practically constant at 45 ppbv for the whole period.

Figure 6.38 c focuses on the RO_2^* results, which on the average remain about 10 pptv with 40% error.

The increase of RO_2^* with NO up to the 0.5 ppb maximum (Figure 6.39), and the similarity of the RO_2^* and NO variation patterns are remarkable.

RO_2^* is expected to decrease as NO increases because the sink reactions of radicals with NO_x are gaining in importance (see section 1.2). The observed behaviour thus indicates the presence of a radical precursor being emitted simultaneously with NO. This could be a peroxy radical source, either transported by convection from another region and/or locally produced.

The existence of potential radical precursors in higher atmospheric layers has already been suggested and discussed in the scientific literature. Thus, the convective injection of peroxides has been suggested to be a source of HO_2 radicals by Prather et al., 1997; Cohan et al., 1999; Jaegle et al., 1997; and Faloona et al., 2000.

In a similar way, the convective pumping of carbonyl compounds like formaldehyde, acetaldehyde or acetone may also be responsible for local production of RO_2* Faloona et al.,2000, already reported on unexpected HO_2 values in different masses in the upper troposphere (at or above 6 km) in the presence of 100<NO<500pptv. These authors interpret the model underestimation of the HO_2 as a possible unmeasured HO_x source that happened to be spatially correlated with NO_x, independent of its origin. A similar underestimation has also been reported both for HO_2 and HO_2+RO_2 measurements performed during the TRACE-P campaign by using Peroxy radical Chemical Ionization Mass Spectroscopy (PerCIMS) (Cantrell et al., 2003b). Similarly, acetone seems to explain most of the missing HO_x in models for H_2O <25 to 30 ppm in the upper troposphere over the Pacific (McKeen et al., [1997]).

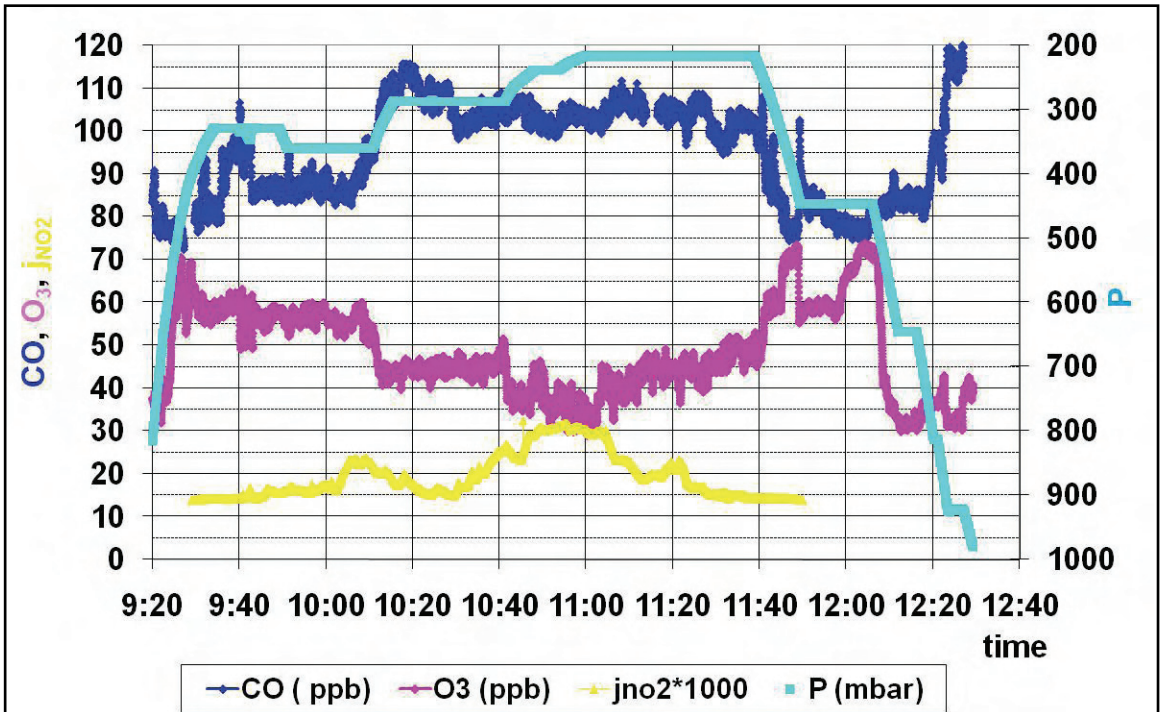

Figure 6.38 a Trace gas mixing ratios J_{NO2} measured during the DLR-Falcon flight on the 15 August 2006.

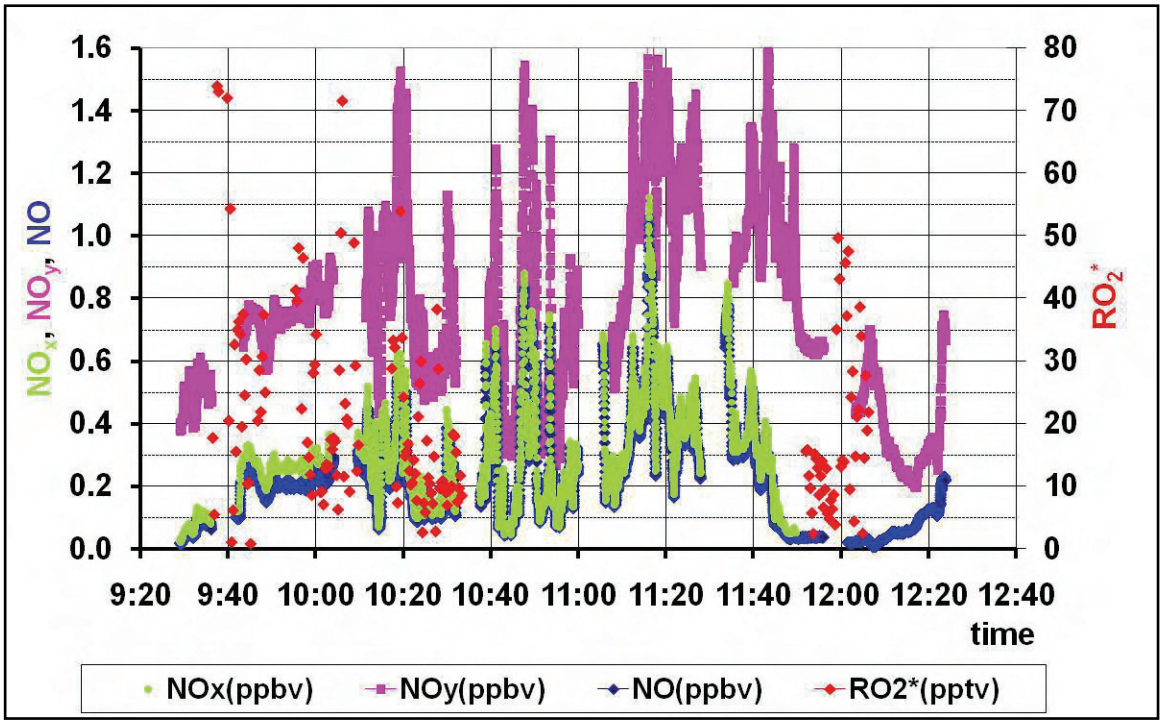

Figure 6.38b Trace gas mixing ratios measured during the DLR-Falcon flight on the 15 August 2006, RO_2^* measurements of DUALER.

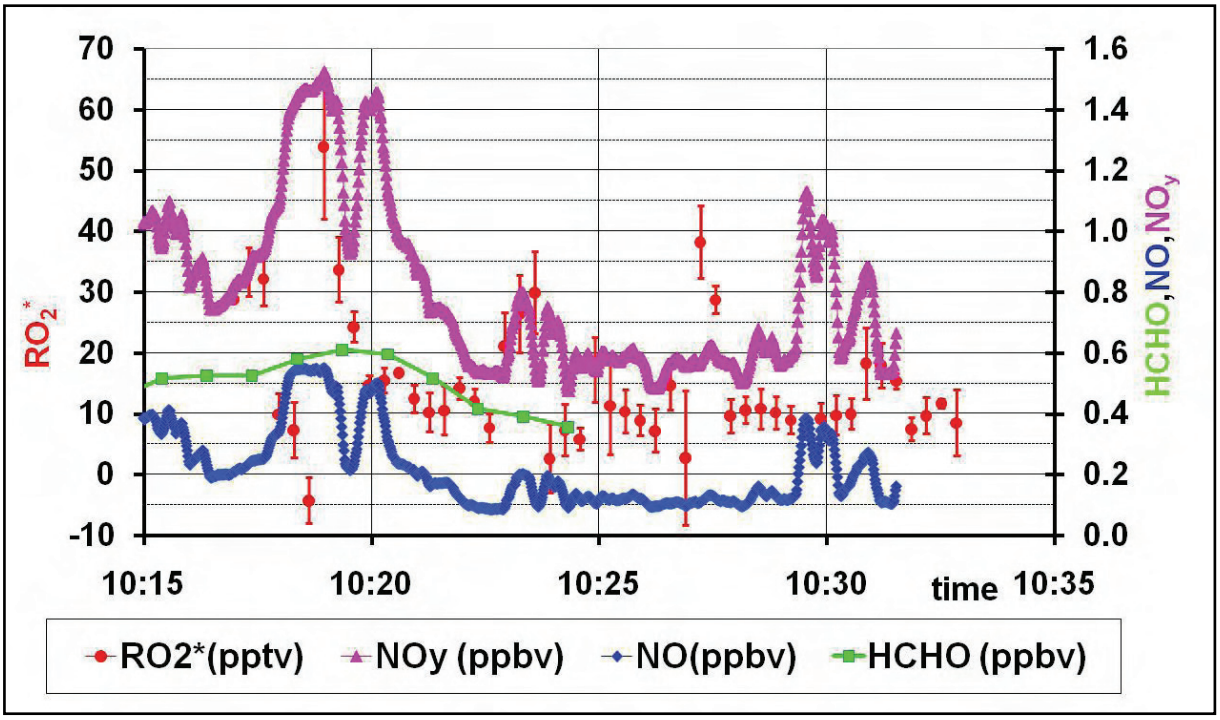

Figure 6.38c Trace gas mixing ratios measured during the DLR-Falcon flight on the 15 August 2006, RO_2^* measurements at 287 mbar. The depicted error bars only represent the statistical error of the 20 s. RO_2^* averages with a relative error 40%.

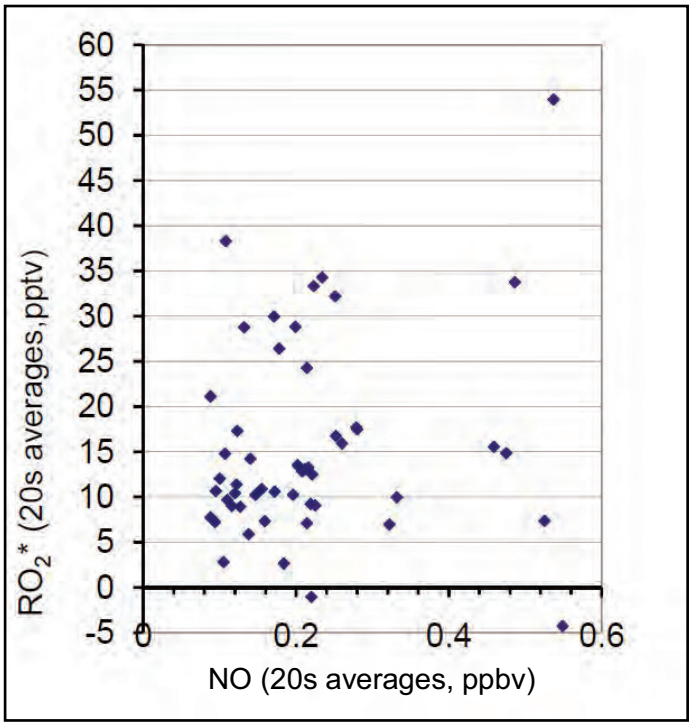

Figure 6.39 RO_2^* and NO observed on the 15.August.2006 at the 287 mbar level

The likeness of potential radical precursors was analysed. The available DLR-Falcon measurements of HCHO at this pressure level (Figure 6.38c) though presenting similarities with the NO and NO_y pattern are not enough to make any conclusive interpretation. On the other hand H_2O remained around 1000 ppm at the 287 mbar pressure level. Concerning the role of acetone, which has a lifetime of several days, as the NO to NO_2 ratio is relatively high (between 7 and 9) if acetone would be transported to upper layers, it should be quite effective in the production of HO_x, as the competing reaction of the formation of peroxyacetyl nitrate (PAN) is favoured by low NO to NO_2 ratios.

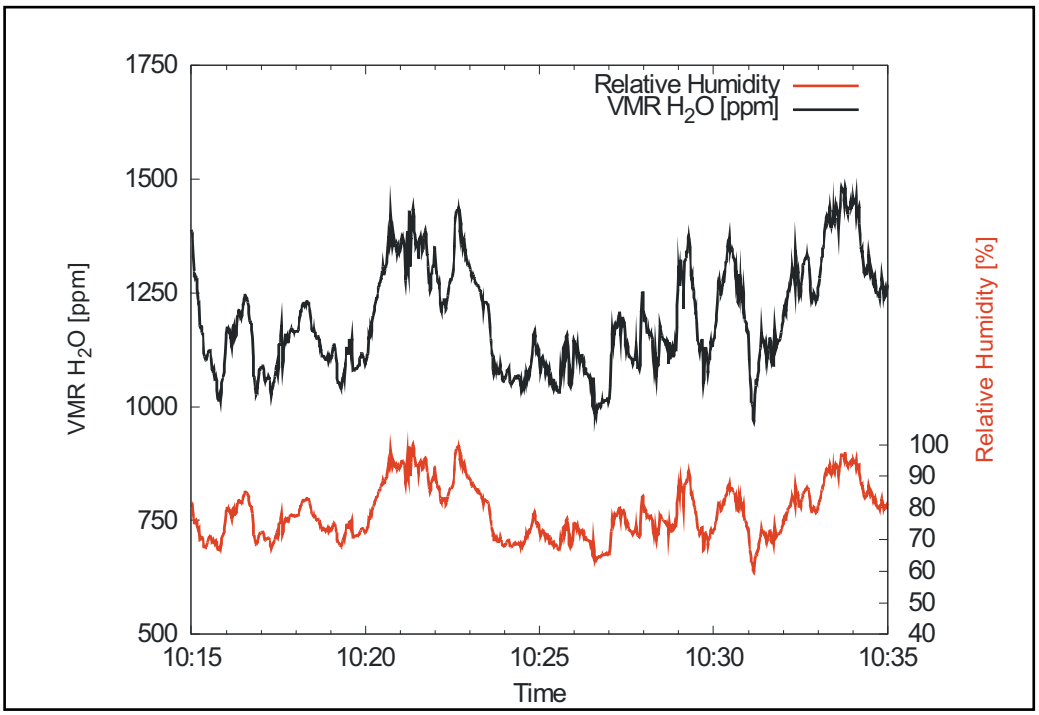

Figure 6.40 Water vapour observed on the 15.August.2006 at the 287 mbar level.The Higher humidity values between 10:20 and 10:24 confirm the presence of air masses affected by convection.

The humidity measured on the DLR-Falcon has been used as indicator of vertical transport of air masses. As shown in Figure 6.40, the increases in humidity at the 10 km flight altitude between 10:20h and 10:24h indicate air masses being uplifted by convection This has an effect in the local chemistry which might be responsible for the variability of the NO_x and RO_2^* in situ values.

Another example of convective outflow is given by the flight on the 04.08.06 Figure 6.41. At the 315 mbar pressure level the DLR-Falcon sampled the outflow of the MCS which has passed over Niamey the day before.

The aircraft remained within the MCS outflow till approximately 9:50 while keeping the pressure level till circa 10:20 hours. The variation of the absolute humidity confirms the vertical convection as can be seen in Figure 6.42. The humidity decreases clearly at 9:50.

NO and NO_y are highly variable during this measurement period, reaching 2.5 and 1.2 ppbv respectively at the beginning of the level around 9:15. At this point RO_2^* remain undetectable as expected in the presence of high NO concentrations, and until NO decreases down to the 0.2-0.5 ppbv level around 9:30.

The increase in the NO/NOy ratio from 0.04 up to 0.5 indicates the presence of relatively fresh emissions. The NO/NO_2 ratio remains relatively high (around 7) most of the time. That implies that as on the 15.08 flight if acetone were simultaneously transported with NO, the production of radicals would be favoured. This might explain the variability of the RO_2^* mixing ratios, occasionally following the NO variations and reaching up to 40 pptv. The error bars depicted in Figure 6.41b correspond to the statistical error of the 20 seconds averages. The total error of the RO_2* 20s averages is estimated to be within 37% .The presence of clouds likely introduces some additional data variability. The role of clouds as sink of radicals has been often discussed in the literature but still requires further clarification.

Concerning potential radical precursors, no obvious correlation with the HCHO data measured simultaneously onboard the DLR-Falcon is observed. This does not exclude however the presence of another source of organic radicals produced from the oxidation of carbon compounds.

Vertical transport from the layers below seems to be the most likely explanation of the observed NO. As presented in the summary of the AMMA observations by Reeves et al., 2009, the general pattern in the trace gas concentrations observed along the whole latitude range measured is indicative of the transport by convection to higher altitudes. The pattern comprises two layers of higher mixing ratios, one close to the surface up to 900 hPa and another at higher altitudes. Similar results are recently reported by Ancellet et al., 2009.

However, for NO, given the low mixing ratios measured within the boundary layer close to the surface Reeves et al.,2009, this transport must be enhanced by NO_x from lightning, which is expected during storm episodes within deep convective clouds.

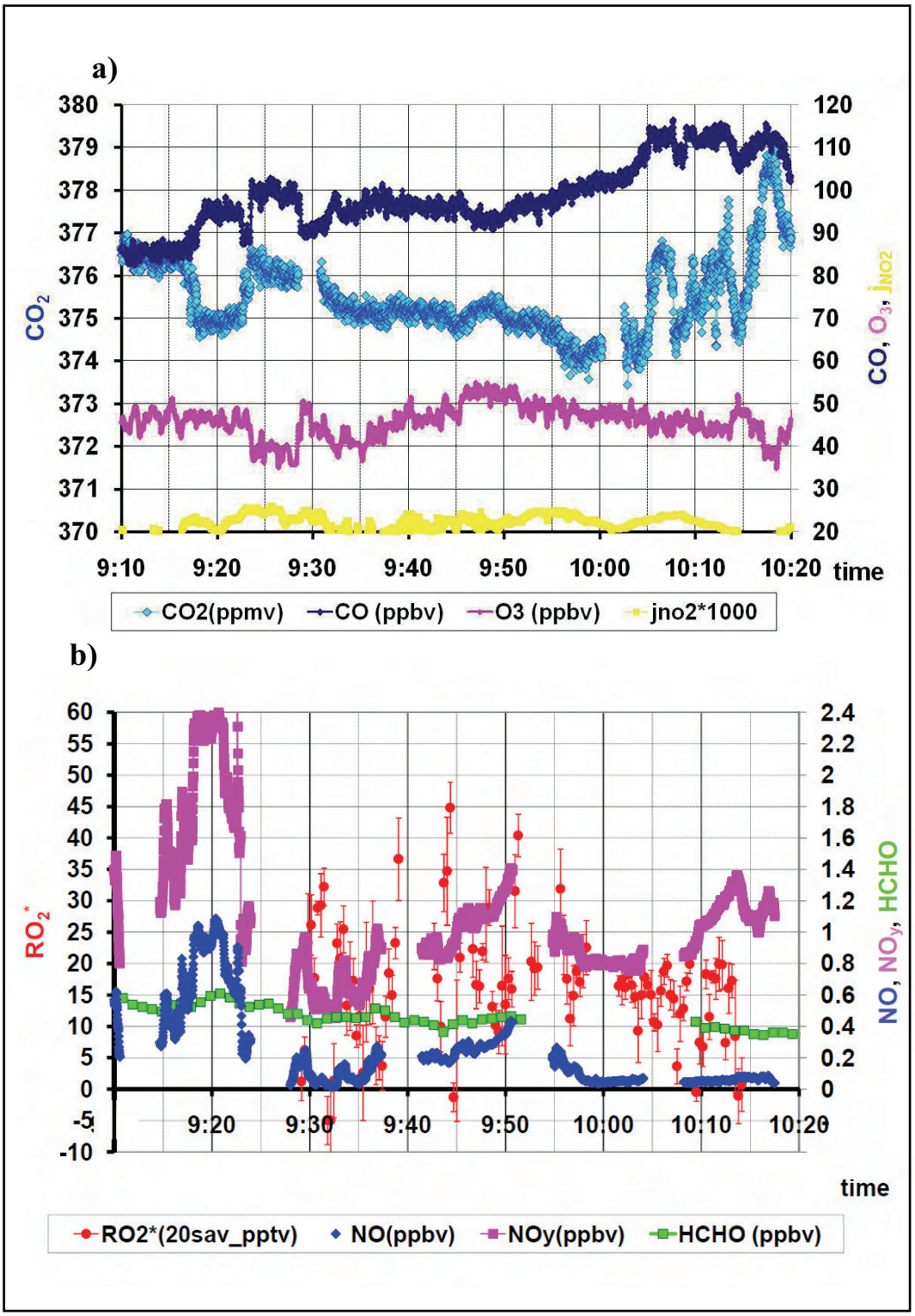

Figure 6.41 Trace gas mixing ratios measured during the DLR-Falcon flight on the 4 August 2006. The out flow of the MSC is reached at the 315 mbar pressure level (9:17h).The depicted RO_2^* error bars represent only the statistical error of the 20s averages, with a relative error 37%.

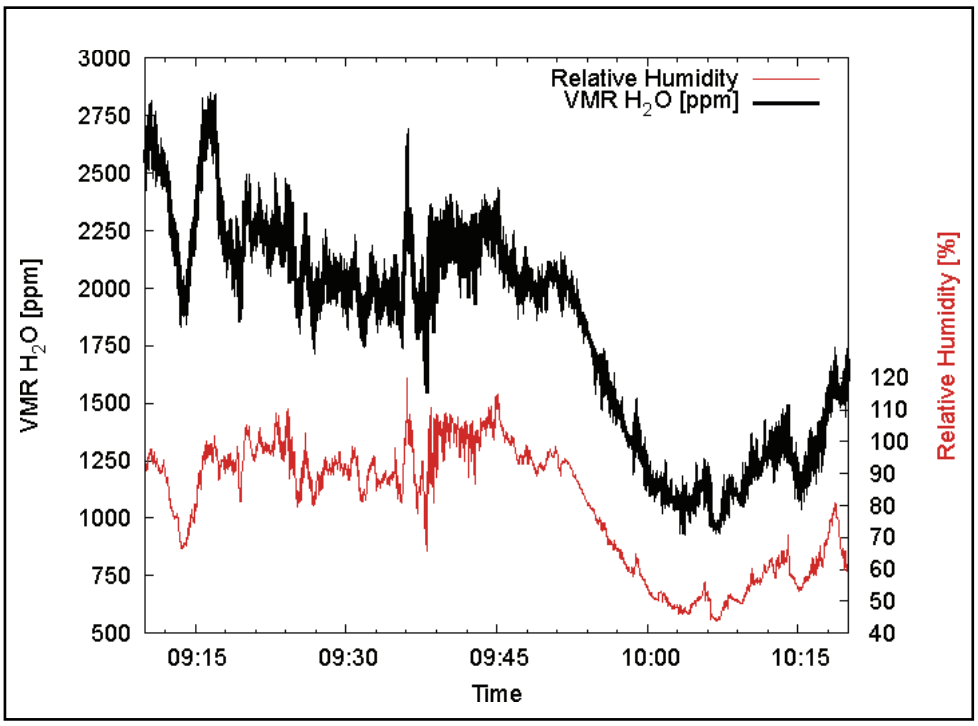

Figure 6.42 Water vapour measured during DLR-Falcon flight on the 4 August 2006. The convection zone is left at 9:50h.

After leaving the convective zone around 10:00 hours, CO increases gradually from 90 to 120 ppb, CO_2 from 374 up to 379 ppmv, NO decreases down to zero and the RO_2^* variability diminishes notably (RO_2^*: 5-25 pptv).

6.2.4.2 RO_2^* measurements in biomass burning plumes

On 4 and 13 August 2006 a vertical profile was taken as the DLR-Falcon reached the coast at Ghana. The flight tracks can be seen in Figure 6.43.

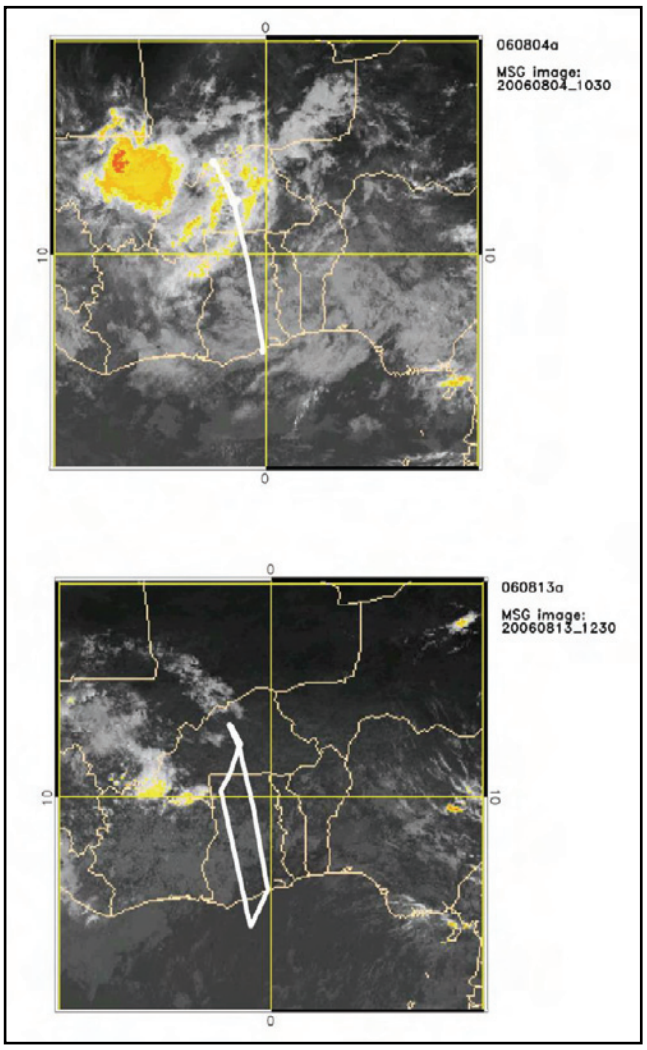

Figure 6.43 DLR-Falcon flight tracks on the a) 4.August.2006 b) 13.August.2006

The concentration of other trace gases, especially CO and CO_2 (Figure 6.44 and Figure 6.45) are indicative of the influence of a biomass burning plume at the higher pressure levels (570- 650 mbar).

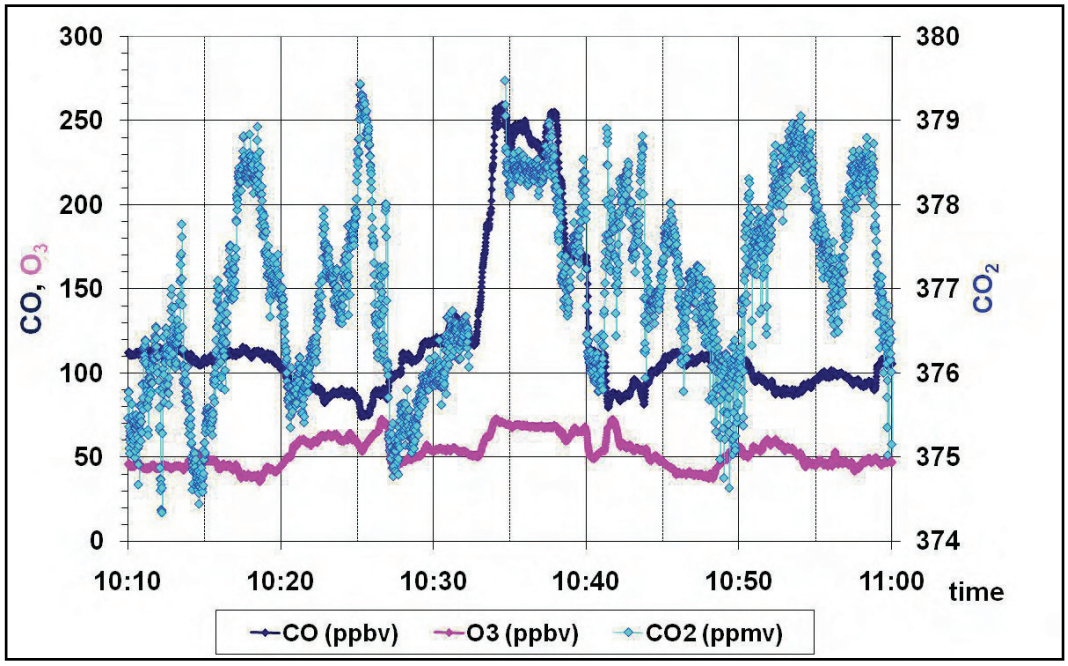

Figure 6.44 a) Trace gas mixing ratios measured during the coastal vertical profile on the 4 August 2006.

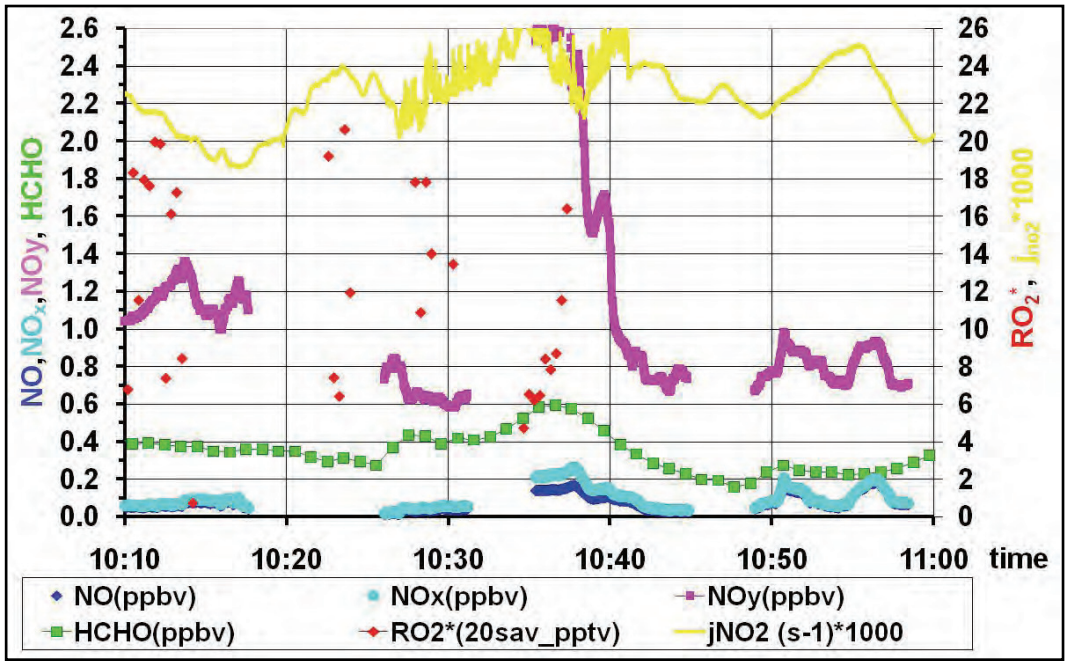

Figure 6.44 b) Trace gas mixing ratios measured during the coastal vertical profile on the 4 August 2006.

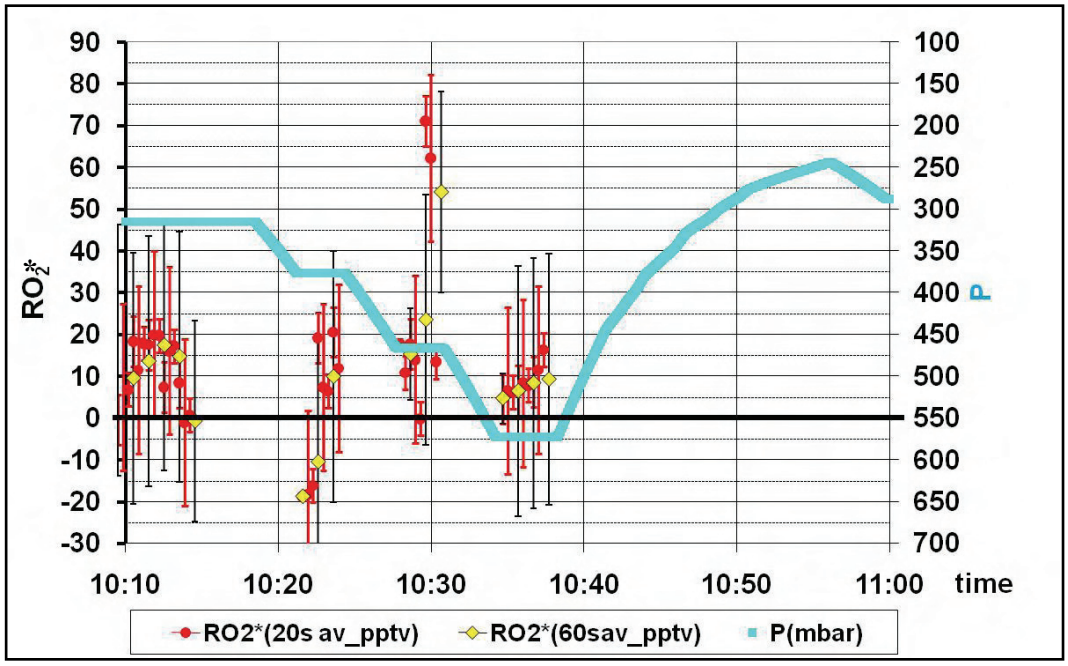

Figure 6.44 c) RO_2* mixing ratios measured during the DLR-Falcon flight on 4.August.2006. The statistical error of 20 and 60 s averages are depicted.

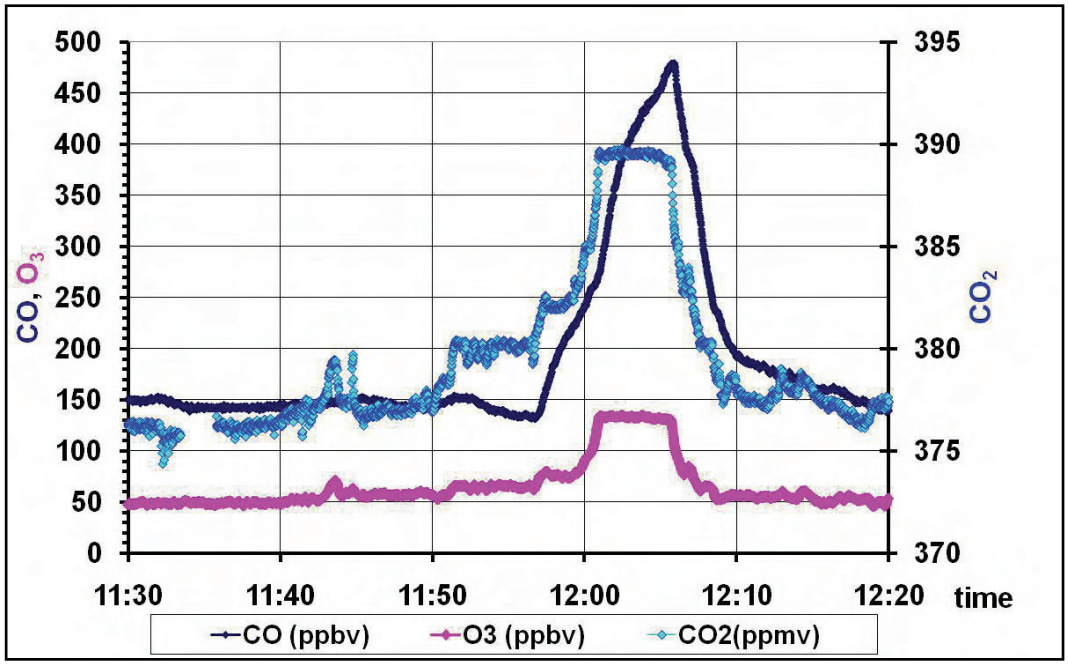

Figure 6.45 a) Trace gas mixing ratios measured during the coastal vertical profile on the 13.August.2006.

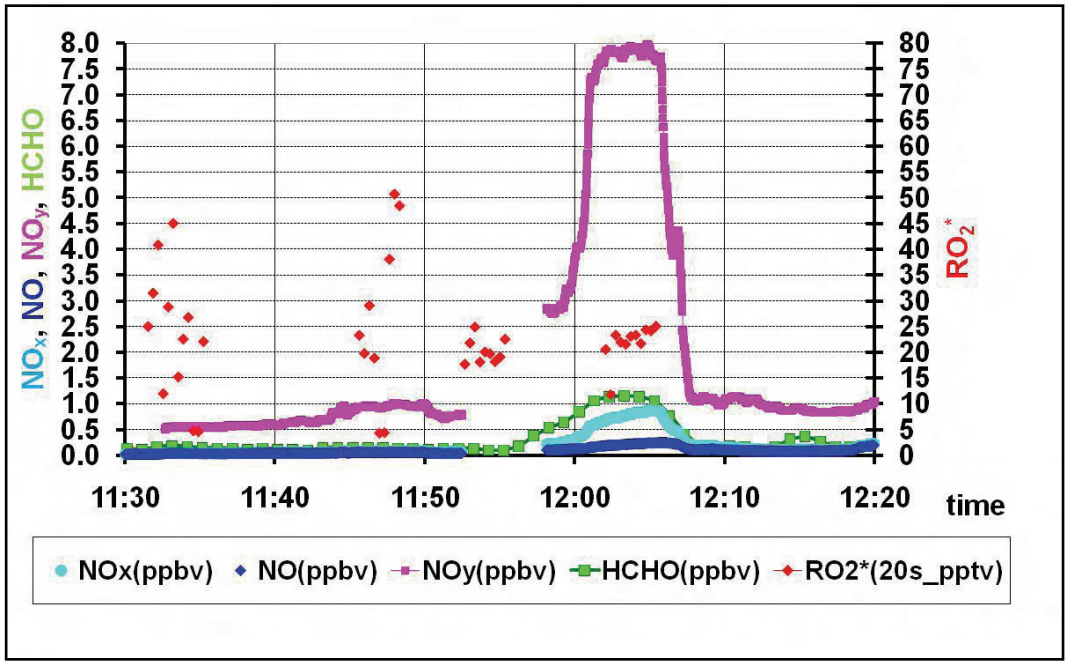

Figure 6.45 b) Trace gas mixing ratios measured during the coastal vertical profile on the 13 August 2006.

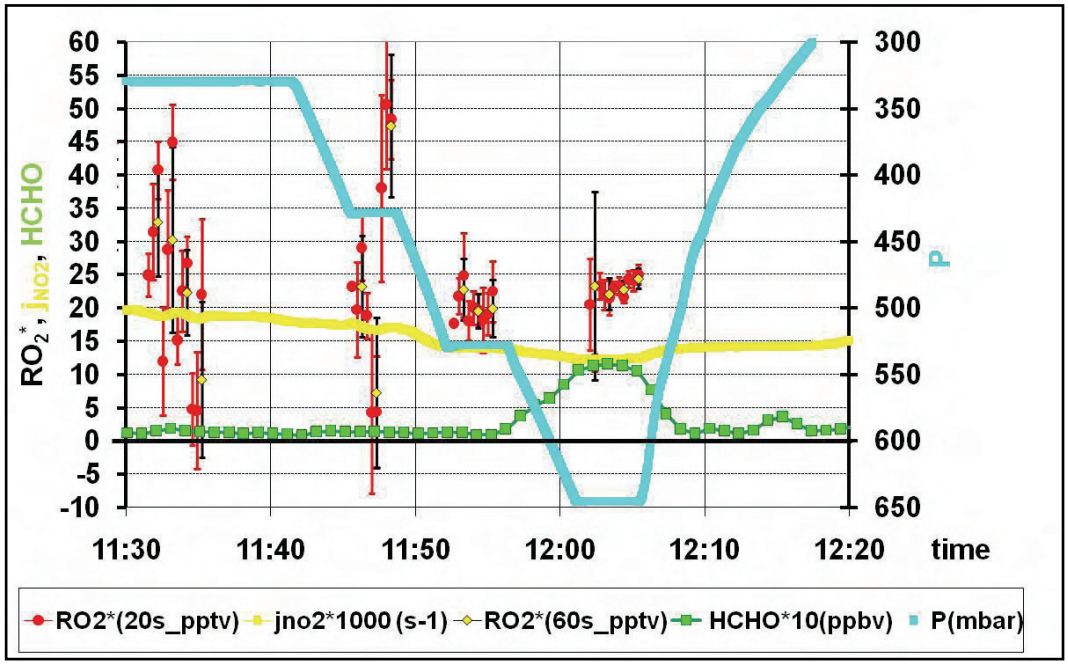

Figure 6.45 c) RO_2* mixing ratios measured during the DLR-Falcon flight on 13.August.2006. The statistical error of 20 and 60 s averages are depicted.

At the highest pressure layer, the trace gases CO, CO_2, O_3, NO and NO_y reach 260, 379, 70, 0.160 and 2.8 ppbv respectively on the 04.08.06. Similarly on the 13.08.06, CO, CO_2, O_3, NO and NOy reach 480, 390 133, 0.25 and 8 ppbv respectively (Figure 6.44 a,b and 6.45 a,b). Interestingly, RO_2^* follow the general pattern, being higher and less variable on the 13.08.06 (20-25 pptv) than on the 4.08.06 (5-15 pptv), in spite of the higher NO concentrations and the lower radiation indicated by the lower values of j_{NO2}, but in agreement with the larger CO and HCHO mixing ratios, the latter reaching 0.6 and 1.16 ppbv on the 04.08.06 and on the 13.08.06 respectively.

The NO/NO_y ratio remains quite low in both cases (around 0.04-0.05) indicating aged air masses. However, HCHO and acetone have both primary and secondary sources and can be therefore produced during the oxidation of the BB plume and act as source of peroxy radicals.

The CO satellite pictures in August from the TERRA-MOPITT (http://eosweb.larc.nasa.gov; Mari et al., 2008) showed in Figure 6.46 as well as the HCHO from the ENVISAT-SCIAMACHY (Reeves et al., 2009; Wittrock et al., 2006) instruments (Figure 6.47) indicate clearly the BB region in the proximity of the Gulf of Guinea and between 5°N and 10°S latitude.

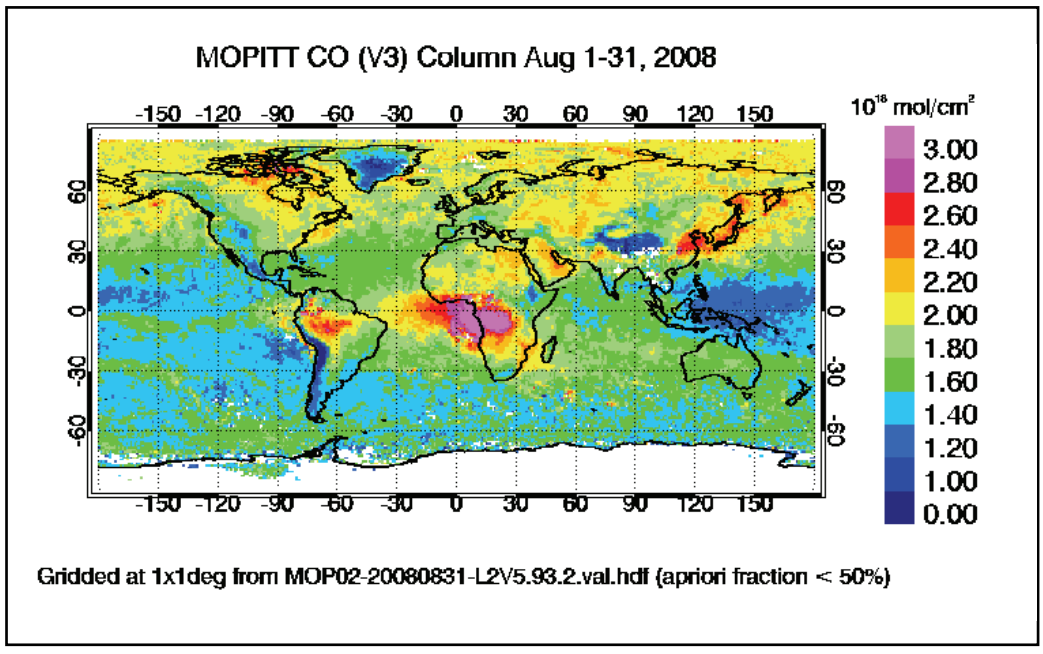

Figure 6.46 CO satellite data obtained in August from the TERRA-MOPITT

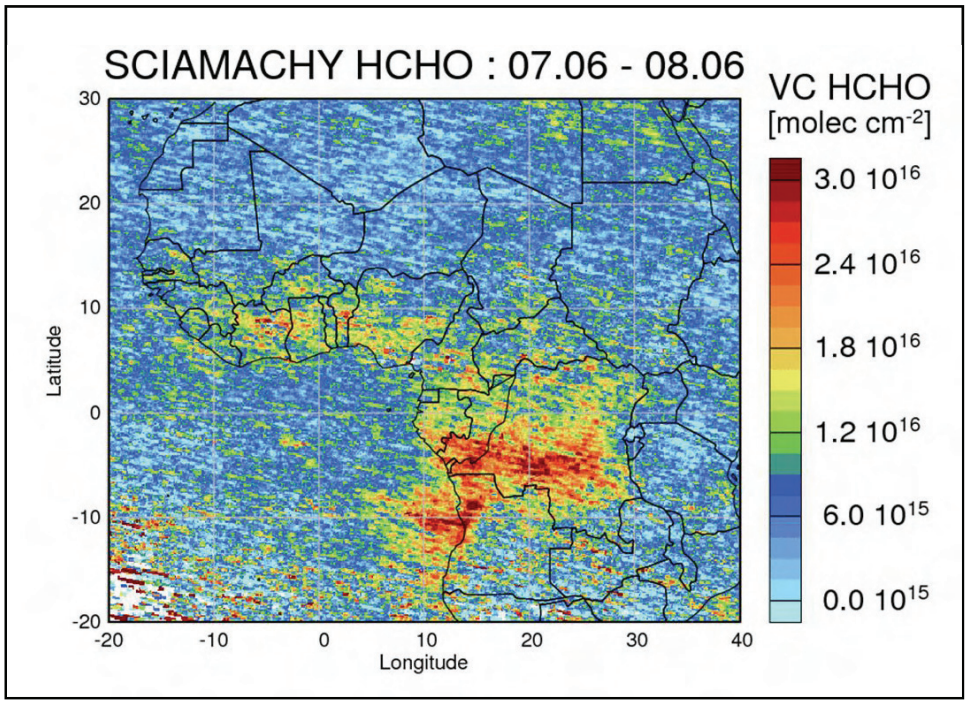

Figure 6.47 Vertical column of HCHO from ENVISAT-SCIAMACHY (Reeves et al., 2009; Wittrock et al., 2006).

Mari et al., 2008 distinguish three different periods during the wet season in Africa, affecting the intrusions of southern hemispheric fire plumes in the Northern Hemisphere. These are characterised by advection patterns related to differences in the position and strength of the African Easterly Jet. According to this classification, the 13th of August is within the second active phase, characterised by the advection of BB plumes out over the Atlantic in the mid troposphere. In contrast, the 4th of August corresponds to a break phase in which the pollutants emitted by the fires should be trapped over the continent and accumulate there till they reach convective regions located further north and are injected in the upper troposphere.

The vertical distribution of the trace gases measured on the 13.08 is less homogeneous than on the 04.08 and presents a clear layer between 500 and 650 mbar of higher concentrations and more photochemical activity (Figure 6.44c and 6.45c). This agrees with the idea of an air mass which has been in more recent contact with BB emissions and is transported at a lower pressure levels to the North as suggested by Mari et al., 2008 during the active phase.

Conversely, on the 04.08, as indicated by the CO_2 concentrations, the air mass sampled seems to have been largely mixed vertically, while the effect of the BB emissions have been lost in importance as the air mass aged, in spite of its potential further enrichment with new fire emissions during the trapping over the continent.

Figure 6.48 shows the projection of the corresponding trajectory densities onto the ground, i.e., the number of trajectories passing a certain volume of air (0.25°x0.25°x100 m),

and the longitude-height projection calculated in Andrés Hernández et al., 2009. For each projection the trajectory density is normalised to unity.

According to these trajectories, the air sampled on the 04.08.06 seems to originate from Nigeria in continental Africa, while at similar altitudes on the 13.08.06 the air masses originate almost exclusively from the biomass burning area in Cameroon-Congo close to the Gulf of Guinea. In addition, the air in the upper layers seems to be transported from Central Africa.

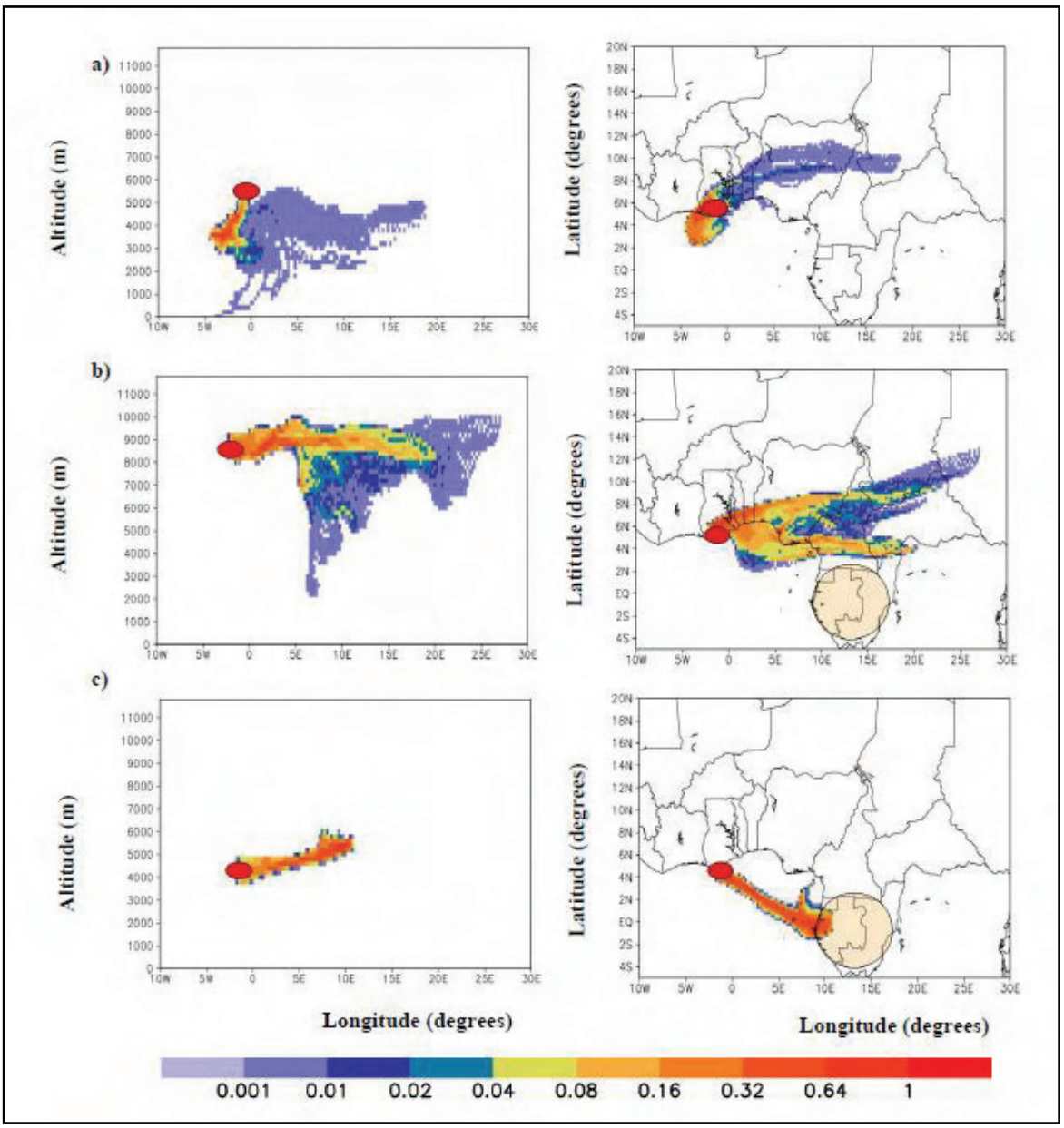

Figure 6.48 Trajectory densities calculated for the vertical profile measured on the (a) 4 August 2006 at 10:30h (b) 13 August 2006 at 11:40 h and c) 13 August 2006 at 12:15 h. The BB burning area according to the satellite data is highlighted.

6.2.4.3 Vertical distribution of RO_2^* over Ouagadougou

Vertical profiles of trace gases were taken over Ouagadougou in three different occasions during the SOP2 campaign. These correspond to the flights on the 11.08, 13.08 and 15.08 2006.

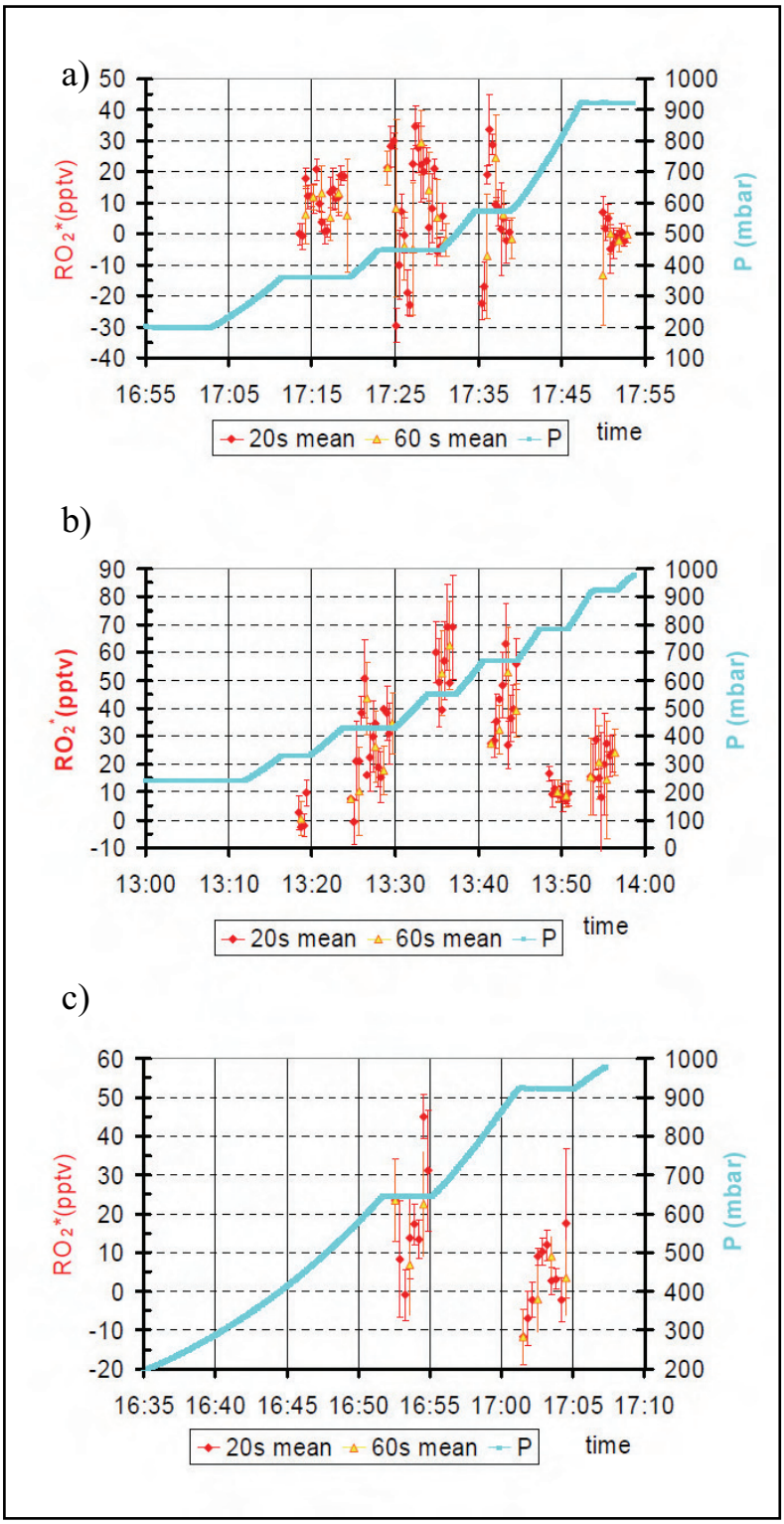

Figure 6.49 RO_2^* mixing ratios measured in vertical profiles taken over Ouagadougou on the a) 11 August 2006, b)13 August 2006 c)15 August 2006

Figure 6.49 summarise the 20 s and 60s averages of the RO_2^* mixing ratios measured at the different pressure levels. The calculated relative error on the 11 August 2006 is 42% on the 13 August 2006 30% and finally on the 15 August 2006 the relative error remains by 40%. Negative mixing ratios are occasionally calculated corresponding to signals measured close to the detection limit and representing high variability around zero, as well as during very rapid changes in other trace species, clouds, humidity etc. In spite of the chemical meaningless of negative mixing ratios, those values are not removed as they are not caused by instrument failures and can provide useful information about radical variability and instrument response in a rapid changing environment.

Vertical RO_2^* profiles taken on different days and under different conditions are not expected to be directly comparable. Peroxy radicals are involved in very local chemistry and as a consequence, their variations at each level are controlled by many different variables like the composition of air masses transported from different source regions, variations in the actinic radiation fields, possible loss reactions in the presence of clouds etc. However, in Figure 6.50 indicates a general vertical pattern with RO_2^* up maximum mixing ratios between 400 and 700 mbar.

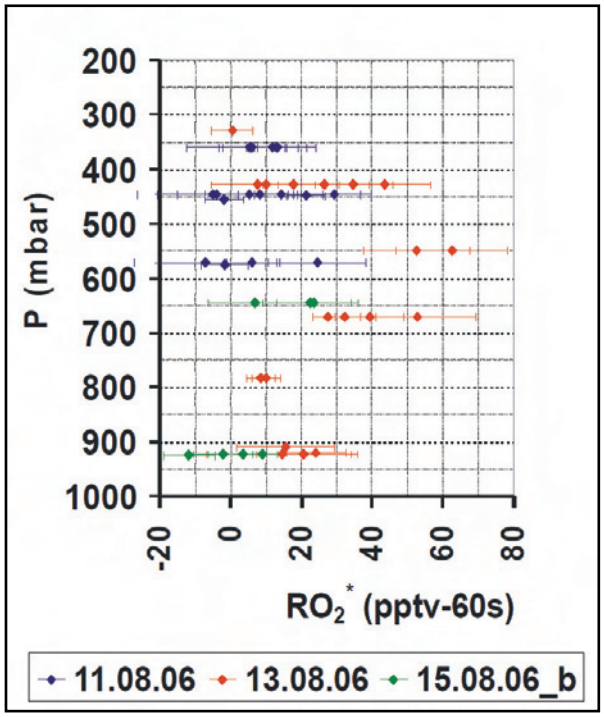

Figure 6.50 Vertical profiles of RO_2^* mixing ratios measured over Ouagadougou. The 60 s mean values and the corresponding error bars are depicted. The data of 15.August.2006b refers to the afternoon flight.

At a first glance the variability of the RO_2^* measurements seem to be large. However, a closer analysis shows that the variability is mostly explained by the presence of clouds, acting as a variable sink of radicals and by the variability of other controlling trace species like NO_x, CO and VOC (Figure 6.51).

This is for instance the case for the measurements taken on the 11.08 at 445 and 570 mbar and on 13.08 close to the surface. The low and variable values of j_{no2} ($\cong 0.006\ s^{-1}$) are indicative of the presence of clouds. This can have an influence in the photochemical production of radicals as a consequence of differences in the actinic conditions. Additionally they are expected to act as a sink of radicals although the mechanism is not well understood.

Variations in the vertical distribution of other trace gas can also play a significant role in the radical distribution. Thus, in some of the flights variations up to 20 ppbv O_3, 60 ppbv CO and 0.8 ppbv NO_x are detected within the same pressure level. On the 15.08 the NO_y at 920 mbar vary up to 20 ppb. This indicates the existence of various vertical layers of different composition and photochemical activity.

The general pattern of the RO_2^* vertical distribution presented in Figure 6.50 is in agreement with values previously reported in the literature for similar environments and conditions (Cantrell et al., 2003a).

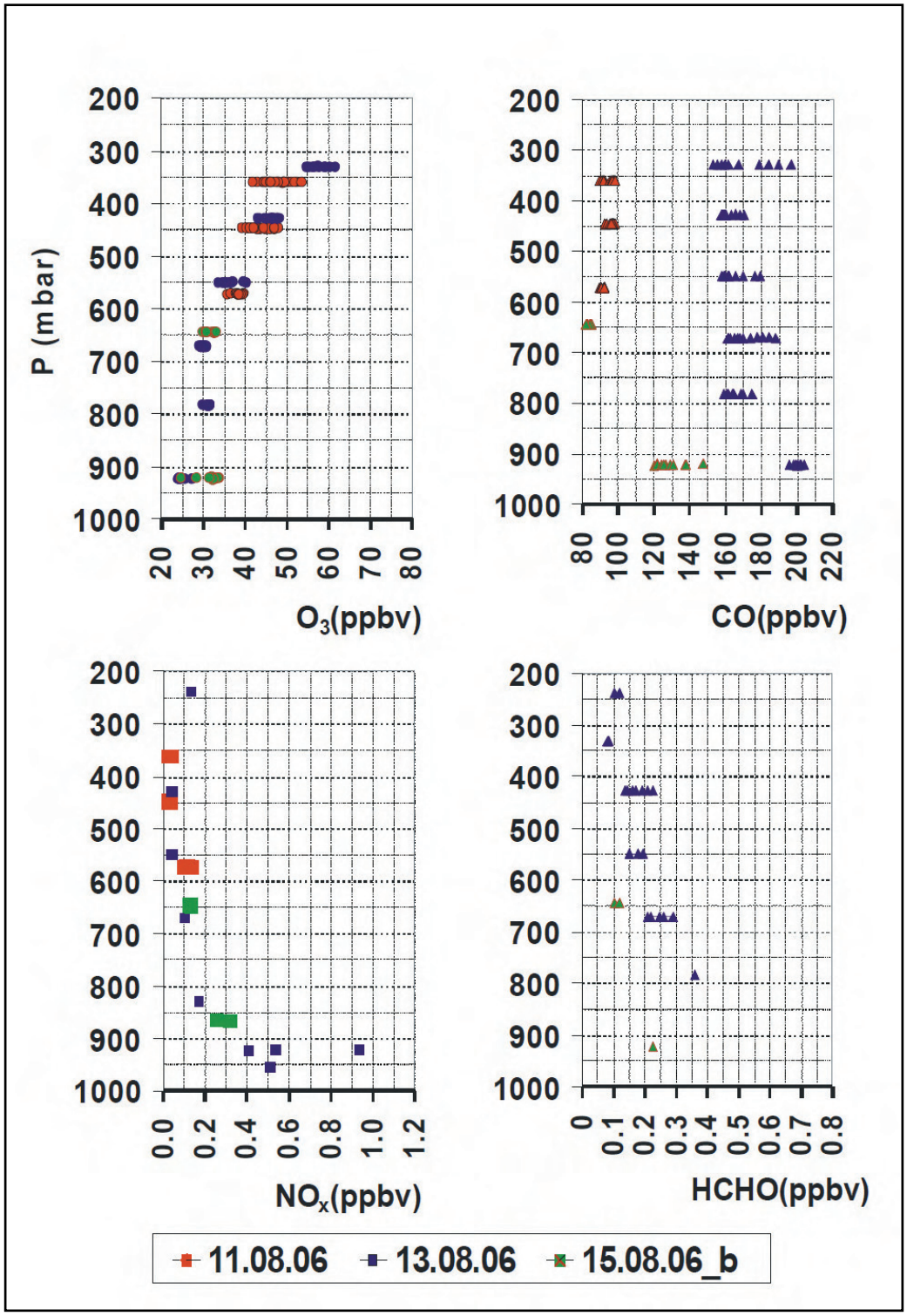

Figure 6.51 Trace gas mixing ratios measured over Ouagadougou on the 11 August 2006, 13 August 2006 and 15 August 2006. The data of 15 August 2006b refers to the afternoon flight.

7 Summary and Conclusions

The present work focused on two main lines of investigation:

a) Development and laboratory characterisation of a DUALER instrument (**DU**al channel **A**irborne peroxy radical chemica**L** amplifi**ER**) based on the PERCA (Peroxy Radical Chemical Amplification) technique for the measurement of peroxy radicals on airborne platforms.

b) Photochemical characterisation of air masses during the monsoon period in West Africa on the basis of peroxy radicals measured with the DUALER developed in a) after its deployment onboard the Falcon research aircraft of the DLR.

The activities carried out to fulfil these objectives, and the related conclusions are as follows:

a1) Based on previous experience of the TROLAS group with PERCA on various platforms, a new DUALER instrument was designed, including two important features: the simultaneous detection of radical and background signal in **two identical reactor-detector lines**, in order to cope with sudden fluctuations in background air during the measurement, and the **pressure stabilisation** of the instrument by means of a common pre-reactor nozzle where the pressure is regulated and kept constant. The double reactor and both detectors were constructed at the mechanical workshop of the University of Bremen

a2) A pressure chamber was implemented in the calibration procedure of the DUALER instrument in order to investigate the stability of its performanceon an airborne platform, i.e., the variation of the NO_2 detector signal and the chain length with the pressure.

a3) Calibrations were performed between 200-1000 mbar, comparing single and double reactors, with and without pressure regulation.

a4) A chemical box model was developed including main chemical reactions involved in the reactor and “radical traps” to simulate wall losses.

a5) The HO_2 calibration source was additionally modified to generate a mixture of HO_2 and CH_3O_2, the main peroxy radicals to be expected in ambient measurements and a series of calibrations at different pressures were carried out.

Main conclusions of this part of the work are:

- The luminol NO_2 detector requires operating at constant pressure on airborne platforms, due to fluctuations in the signal and sensitivity with the pressure.
- The pressure regulation leads to radical losses at the pre-reactor nozzle. The experimentally determined chain length is therefore an effective chain length (eCL), resulting from the amplification of the radicals reaching the gas addition point at the reactors. The losses at the pre-reactor nozzle are mainly wall losses.
- The eCL varies with $\Delta P = P_{air\ sample} - P_{DUALER}$, indicating the effect of turbulences and retention time in the wall losses at the pre-reactor nozzle. At different ΔP the eCL is therefore a result of these competing mechanisms in the wall losses which may reach a compensation point at about ΔP=500 mbar. For ΔP=500 mbar, an eCL 15% higher than at the maximum ΔP=800 mbar and at the minimum ΔP=100 mbar is obtained. The laboratory results show that the performance of the instrument during airborne measurements is expected to be best for ΔP around 500 mbar.
- The ratio between the eCL for a 100% HO_2 calibration sample and for a 50% CH_3O_2 and 50% HO_2 calibration mixture has a mean value of 0,84 over the pressure range 200 to 1000 mbar, when the DUALER is kept at 300 mbar. The higher eCL values are interpreted to be the result of lower CH_3O_2 wall loses in the pre-reactor nozzle.
- According to the box model and on the basis of the experimental results obtained at 300 mbar, the presence of CH_3O_2 in the sampled air may increase the uncertainty of the RO_2^* determination with a relative error contribution to the total error below 25% and most likely between 8- 14%.

b1) Subsequently the DUALER was deployed in the DLR Falcon and participated in the measurement campaign of the AMMA (African Monsoon Multidisciplinary Analysis) project. During AMMA, a total of 8 DLR-Falcon flights were conducted from Ouagadougou in Burkina Faso (12.15°N 1.30°W) in the period from 01.08.06 to 18.08.06. Part of the present work was operating the DUALER during this time period.

b2) Different software tools coded in Matlab were developed to analyse the raw data obtained during the measurement campaign.

b3) A mathematical procedure on the basis of simultaneous O_3 measurements on board was developed for monitoring in-flight variations in the sensitivity of the detector. This validation procedure was tested and applied to the analysis procedure.

b4) Air masses having different photochemical histories were investigated

The interpretation of the data obtained within this part of the work leads to following main conclusions:

- During the monsoon period RO_2^* mixing ratios of high variability and up to 50-60 pptv were observed in the outflow of mesoscale convective systems (MCS). It can be concluded that the MCS outflow air masses detected during the measurement campaign are still photochemically active.

- The RO_2^* variability is partly associated with the presence of clouds, which block and reflect photochemically active ultraviolet radiation.

- Occasionally, unexpected simultaneous increases of NO and RO_2^* are observed, indicating the presence of a radical precursor, which is related to NO emissions. As the NO mixing ratios measured during the period by other aircrafts in the boundary layer are generally lower, the observed NO_x must be to a large fraction related to lightning episodes rather than being exclusively convectively transported from the more polluted boundary layer to the upper levels.

- The differences in chemical composition of observed air masses affected by biomass burning plumes agree reasonably with the expected advection patterns related to the different phases of the African Easterly Jet. These plumes were detected within 400 and 500 mbar, containing RO_2^* mixing ratios around 20 pptv and with peak values up to 60 pptv which indicates the presence of photochemical active layers.

- The RO_2^* vertical distribution obtained from the flights over Ouagadougou shows maximum mixing ratios between 450 and 700 mbar in agreement with literature data taken under similar conditions. This maximum provides evidence for enhanced free radical production in this pressure range as a result of the uplifting of radical precursors from below.

The main scientific output of the present work has been summarised in two scientific publications: Andrés, Kartal, et al., 2009; and Kartal, et al., 2009.

Appendix 1

Least square method for error calculation

The linear parameters and the errors of the parameters of the NO_2 calibrations are calculated by using the least square method. The least square method is a procedure to determine the best fit line to data by calculating the fit parameters, in the case of NO_2 calibrations the parameters are *a* and *b* for the equation:

$$[NO_2]_k = aV_i + b \tag{1}$$

where $[NO_2]_k$ is the mixing ratio calculated with the fit parameters, V_i is the detector response in volts. The objective to apply the least square method to the data is to find out the best *a* and *b* with the criteria:

$$\begin{aligned} F(a,b) &= \sum_{i=1}^{N} e_i^{\,2} = \sum_{i=1}^{N} aV_i + b - [NO_2]_i^{\,2} \\ \frac{\delta F}{\delta a}|_a &= 0 \quad , \frac{\delta F}{\delta b}|_b = 0 \end{aligned} \tag{2}$$

where the $\frac{\delta F}{\delta a}$ and $\frac{\delta F}{\delta b}$ are the equations for calculating the fit parameters *a* and *b*, e_i is the residuals of the calculated mixing ratio with the fit parameter, and $[NO_2]_i$ is the mixing ratio produced during the calibration. The derivation of F according to *a* and *b* is set to zero, in order to have the minimum e_i deviation from the experimental data at the corresponding *a* and *b*.

The equations $\frac{\delta F}{\delta a}$ and $\frac{\delta F}{\delta b}$ in (2) can be solved by the matrix calculations as following:

$$A \cdot x = d \qquad x = (A^T \cdot A)^{-1} \cdot A^T \cdot d \tag{3}$$

where $x = \begin{bmatrix} a \\ b \end{bmatrix}$; $A = \begin{bmatrix} V_1 & 1 \\ . & . \\ . & . \\ V_N & 1 \end{bmatrix}$; $d = \begin{bmatrix} NO_{2\ 1} \\ NO_{2\ i} \\ NO_{2\ N} \end{bmatrix}$. The resulting x vector is consisting of the fit parameters obtained with least square method; x(1,1)=***a***, x(2,1)=***b*** (W. Menke, 1984).

This matrix operation simplifies the calculating of the fit parameters with computer programming.

The error of *a* and *b* is calculated in equation 4 and 5 on the basis of the mean square error (σ_{NO_2}) of the difference of the NO_2 mixing ratios calculated by the least square parameters and the experimental ones.

$$\sigma_a{}^2 = \frac{\sigma^2{}_{NO_2}}{\sum_{i=1}^{N} V_i^2 - \frac{1}{N}\left(\sum_{i=1}^{N} V_i\right)^2} \tag{4}$$

$$\sigma_b{}^2 = \frac{\sigma^2{}_{NO_2}\ \frac{1}{N}\sum_{i=1}^{N} V_i^2}{\sum_{i=1}^{N} V_i^2 - \frac{1}{N}\left(\sum_{i=1}^{N} V_i\right)^2} = \sigma_a{}^2\ \frac{1}{N}\sum_{i=1}^{N} V_i^2 \tag{5}$$

Finally the coefficient of determination R^2 is calculated by the ratio of the square of the error of the linear regression of the response of detectors and mixing ratio, and the standard deviation of the mixing ratios produced during the calibration as follows:

$$R^2 = 1 - \frac{1/N-1 \sum_{i=1}^{N} \left(NO_{2\ i} - aV_i - b\right)^2}{1/N-1 \sum_{i=1}^{N} \left(NO_{2\ i} - \text{mean}\ \ NO_{2\ 1..i..N}\right)^2} \tag{6}$$

As mentioned in section 3.4, the important factors which determine NO_2 calibration quality are the variations in the offset response of the detector that is due to the aging of the NO scrubbers to remove the NO_2 traces from NO flow, and to the variation of the efficiency of the surface reaction of NO_2 with luminol. The Figure A1 presents an example for a calibration in which the offset response is not constant.

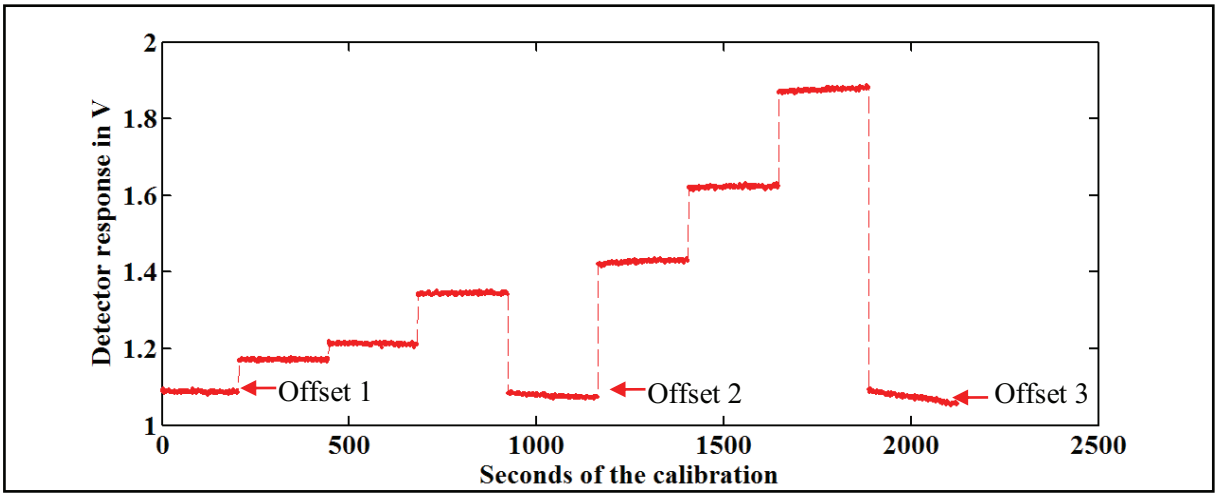

Figure A 1 Detector response in volts, each level corresponds to a mixing ratio of NO_2.

The least square fit method explained above calculates the $\sigma_a = 0,04\,\text{ppb}\,\text{V}^{-1}$, $\sigma_b = 0,05$. In figure A2, the volt signal versus ppb is plotted separately for each offset for clarification.

It can be seen from the Figure A2 the difference of the NO_2 parameters for each case. The standard deviation of *a* is 0,067 ppbV^{-1} and for the *b* remains by 0, 1. This confirms that the offset changes during the NO_2 calibrations which cannot be monitored by the general mathematical error analysis as these changes are not dominant in the whole calibration data set.

As indicated in section 3.4 a relative error of 3% is considered for the parameter *a* , which is a realistic estimation taking into account the reproducibility of the calibration parameters during a day being generally performed two calibrations per day.

a)

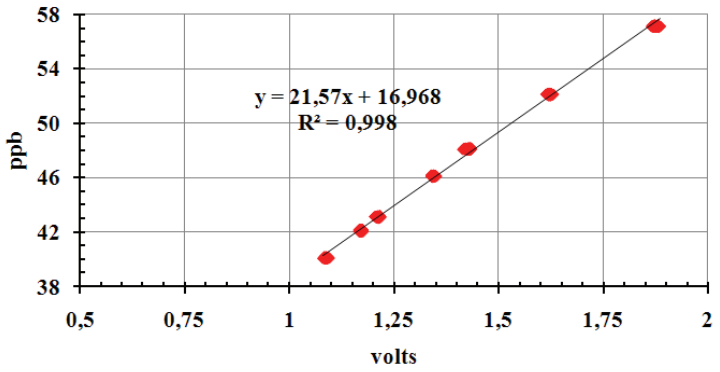

a) results considering only the first offset response

b)

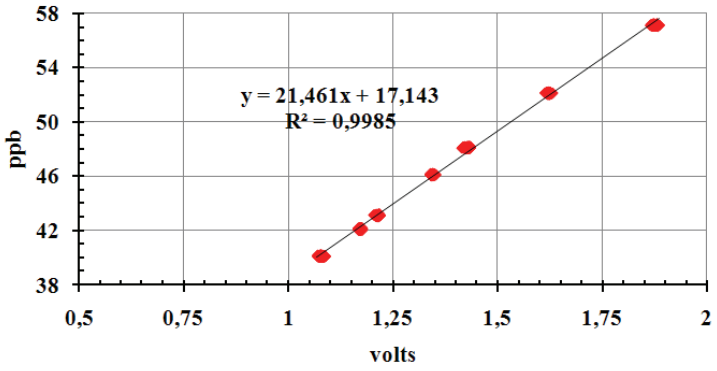

b) results considering only the second offset response

c)

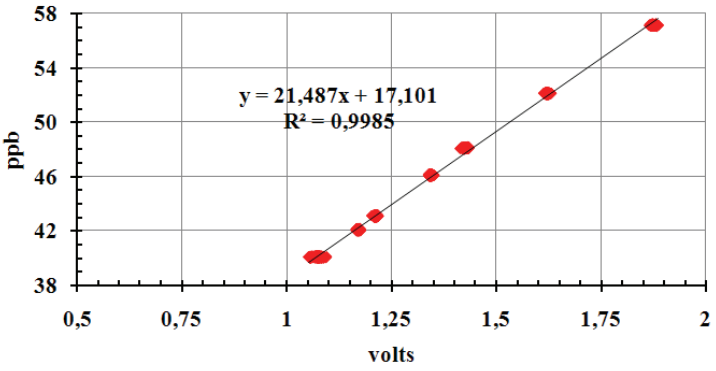

c) results considering only the third offset response

d)

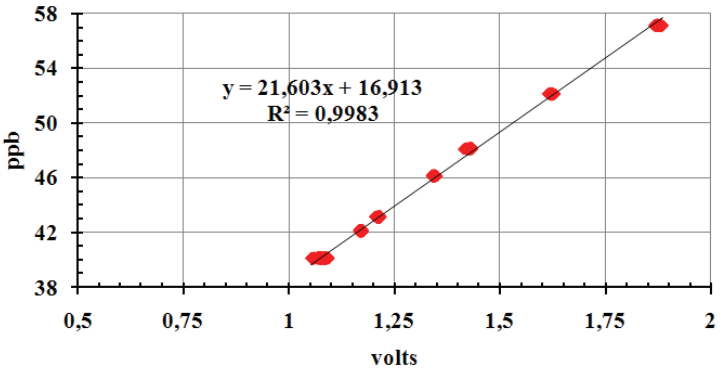

d) results considering the whole offset response

Figure A 2 Comparison of the results of a calibration using the different offset responses during the calibration.

Appendix 2

Chemical box model

The algorithm of the box model described in Chapter 4 can be explained schematically as following

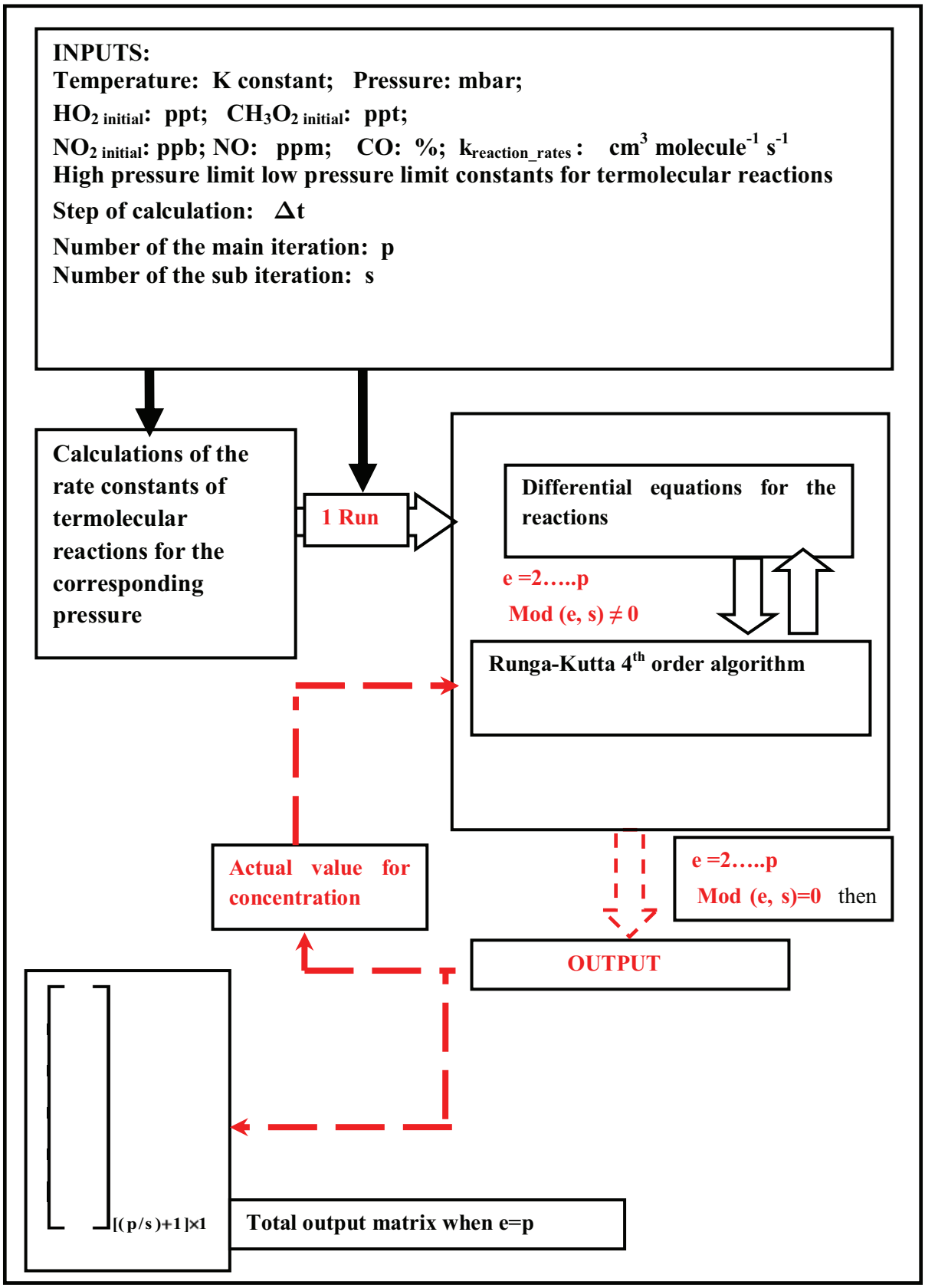
INPUTS:
Temperature: K constant; Pressure: mbar;
HO2 initial: ppt; CH3O2 initial: ppt;
NO2 initial: ppb; NO: ppm; CO: %; kreaction_rates : cm3 molecule-1 s-1
High pressure limit low pressure limit constants for termolecular reactions
Step of calculation: Δt
Number of the main iteration: p
Number of the sub iteration: s
Calculations of the rate constants of termolecular reactions for the corresponding pressure
1 Run
Differential equations for the reactions
e =2…..p
Mod (e, s) ≠ 0
Runga-Kutta 4th order algorithm
Actual value for concentration
e =2…..p
Mod (e, s)=0 then
OUTPUT
[(p/s)+1]×1
Total output matrix when e=p

As an example, the Runga Kutta algorithm is applied to a termolecular reaction;

$$C + B + M \rightarrow A + M$$

The input values are initial concentrations C_0, B_0, A_0, temperature, pressure, low and high pressure parameters to calculate k_{BC} for the corresponding pressure and temperature.

$$\frac{d[A]}{dt} = k_{BC}[B][C] \qquad k_{BC} : \text{rate constant of the reaction} \tag{7}$$

$$\frac{d[B]}{dt} = -k_{BC}[B][C] \tag{8}$$

$$\frac{d[C]}{dt} = -k_{BC}[B][C]$$

$$\frac{d[A]}{dt} = F(t, A(B(t),C(t),k_{BC})) \,, \quad \frac{d[B]}{dt} = Z(t, B(B(t),C(t), k_{BC})), \quad \frac{d[C]}{dt} = Z(t,C(C(t),B(t), k_{BC}))$$

$$\begin{aligned}
&A1 = \Delta t\, F(B_0, C_0, k_{BC}) \qquad B1 = \Delta t\, Z(B_0, C_0, k_{BC}) \qquad C1 = \Delta t\, Z(B_0, C_0, k_{BC}) \\
&A2 = \Delta t\, F(B_0 + 0.5 * B1, C_0 + 0.5 * C1, k_{BC}) \\
&B2 = \Delta t\, Z(B_0 + 0.5 * B1, C_0 + 0.5 * C1, k_{BC}) \\
&C2 = \Delta t\, Z(B_0 + 0.5 * B1, C_0 + 0.5 * C1, k_{BC}) \\
&A3 = \Delta t\, F(B_0 + 0.5 * B2, C_0 + 0.5 * C2, k_{BC}) \\
&B3 = \Delta t\, Z(B_0 + 0.5 * B2, C_0 + 0.5 * C2, k_{BC}) \\
&C3 = \Delta t\, Z(B_0 + 0.5 * B2, C_0 + 0.5 * C2, k_{BC}) \\
&A4 = \Delta t\, F(B_0 + B3, C_0 + C2, k_{BC}) \\
&B4 = \Delta t\, Z(B_0 + B3, C_0 + C3, k_{BC}) \\
&C4 = \Delta t\, Z(B_0 + B3, C_0 + C3, k_{BC}) \\
&\\
&A_1 = (A1 + 2 * A2 + 2 * A3 + A4) / 6 \\
&B_1 = (B1 + 2 * B2 + 2 * B3 + A4) / 6 \\
&C_1 = (C1 + 2 * C2 + 2 * C3 + C4) / 6
\end{aligned} \tag{9}$$

The group of equations above applies the Runga –Kutta 4 order algorithm to calculate the variations of the concentration with time. It should be noted that the initial values of p are updated after each sub-iteration. The number of values obtained at the end is (p/s)+1.

References

Agustí-Panareda, A. and Beljaars, A.:ECMWF's contribution to AMMA, ECMWF Newsletter, No 115, Spring 2008.

Andrés Hernández, M.D., Burkert, J., Reichert, L., Stöbener, D., Meyer- Arnek J., and Burrows, J.P., Dickerson, R.R., and Doddridge, B.: Marine boundary layer peroxy radical chemistry during the AEROSOLS99 campaign: measurements and analysis. Journal of Geophys. Res, 106, D18, 20,833-20,846, 2001.

Andrés-Hernández, M. D., Kartal, D., Reichert, L., Burrows, J.P, Arnek , J. M., Lichtenstern, M., Stock, P., and Schlager, H.: Peroxy radical observations over West Africa during the AMMA 2006: Photochemical activity in the outflow of convective systems, Atmos. Chem. Phy., 9, 3681-3685, 2009.

Archie W.C. Principles of Energy Conversion, 1991.

Atkins, P. W. Physical Chemistry Oxford University Press, 2001

Boeker, Egbert., Van Grondelle, Rienk.: Environmental Physics, John W.& Sons, 1994.

Burkert, J., Andrés-Hernández, M.D., Stöbener, D., Burrows, J.P., Weissenmayer, M., Kraus, A.: Peroxy radical and related trace gas measurements in the boundary layer above the Atlantic Ocean, J. Geophys. Res., 106 , 6 , p. 5457, 2001b.

Burkert, J., Behmann, T., Andrés Hernández, M.D., Weißenmayer, M., Perner, D., and Burrows, J.P.: Measurements of peroxy radicals in a forested area in Portugal. Chemosphere-Global change science, 3327-3338, 2001a.

Cantrell, C. A., Shetter, R. E., Gilpin, T. M., Calvert, J. G., Eisele, F. L, and Tanner, D. J.: Peroxy radical concentrations measured and calculated from trace gas measurements in the Mauna Loa Photochemistry Experiment 2, J. Geophys. Res., 101, 14653-14664, 1996a.

Cantrell, C. A., Shetter, R. E., Lind, J.A., et al., An Improved Chemical Amplifier Technique for Peroxy Radical Measurements, J. Geophys. Res., 98, 2897-28909, 1993.

Cantrell, C.A., Edwards, G.D., Stephens, S., Mauldin, L., et al.: Peroxy radical behaviour during the Transport and Chemical Evolution over the Pacific (TRACE-P) campaign as measured aboard the NASA P-3B aircraft, Journal of Geophysical Research, Vol. 108, No. D20, 8797, doi: 10.1029/2003JD003674, 2003b.

Cantrell, C.A., Edwards, G.D., Stephens, S., Mauldin, L., Kosciuch , E., Zondlo, M., and Eisele, F.: Peroxy radical observations using chemical ionization mass spectrometry during TOPSE, Journal of Geophysical Research, Vol. 108, No. D6, 8371, doi: 10.1029/2002JD002715, 2003a.

Cantrell, C.A., R.E. Shetter, and J. Calvert: Peroxy Radical Chemistry During Fieldvoc 1993 in Britain, France, Atmospheric Environment, 30(23), 3947-3957,1996.

Cantrell, C.A., Shetter R.E., and Calvert, J.G.: Dual-Inlet chemical amplifier for atmospheric peroxy radical measurements, Analytical Chemistry, 68, 4194-4199, 1996b.

Cantrell, C.A., Zimmer, A., and Tyndall, G.S.: Absorption cross sections for water vapour from 183 to 193 nm, Geophys. Res. Letters, 24, 2195-2198, 1997.

Carslaw, N., Creasey, D.J., Heard, D.E., Lewis, A.C., McQuaid, J.B., Pilling, M.J.,,Monks, P.S., Bandy B.J., and. Penkett, S.A: Modelling OH, HO_2, and RO_2 in the marine boundary layer: 1. Model construction and comparison with field measurements. Journal of Geophysical Research(Atmos.), 104 (D23), 30241-30255, 1999.

Clemitshaw, K., Carpenter, L., Penkett, S., and Jenkin, M.: A calibrated peroxy radical chemical amplifier for ground-based tropospheric measurements, J. Geophys. Res., 102, D21, 25405-25416, 1997.

Clemitshaw, K.C.: A review of instrumentation and measurement techniques for field studies of gas-phase tropospheric chemistry. Critical Reviews in Environmental Science and Technology, 34, 1-108, 2004.

Cotton, W. R., Anthes, R. A.: Storm and Cloud Dynamics, International Geophysics Series Volume 44, 1989.

Creasey, D., Heard, D.E., and Lee, J.D.: Absorption cross-section measurements of water vapour and oxygen at 185 nm. Implications for the calibration of field instruments to measure OH, HO_2 and RO_2 radicals, Geophys. Res. Lett. 27, 11, 1651-1654, 2000.

Curtis, A. R., and W. P. Sweetenham, FACSIMILE/CHEKMAT user's manual, AERE Rep. R-12805, Her Majesty's Stn. Off., Norwich, England, 1988

Edwards, G.D., Cantrell, C.A., Stephens, S., et al.: Chemical Ionization Mass Spectrometer Instrument for the measurement of tropospheric HO_2 and RO_2, Anal. Chem, 75, 5317-5327, 2003.

Eisele, F.L., D.J. Tanner: Ion-Assisted Tropospheric OH measurements, Journal of Geophysical Research, Vol 96, No. D5, 9295-9308, 1991.

Fleming, Z. L., Monks, P. S., Rickard, A. R., Bandy, B. J., Brough, N., Green, T. J., Reeves, C. E., and Penkett S. A.: Seasonal dependence of peroxy radical concentrations at a Northern hemisphere marine boundary layer site during summer and winter: evidence for radical activity in winter, Atmospheric Chemistry and Physics, 6, 5415-5433, 2006b.

Fleming, Z. L., Monks, P. S., Rickard, A. R., Heard, D. E., Bloss, W. J., Seakins, P.W., Still, T. J., Sommariva, R., Pilling, M. J. ,Morgan, R., Green, T. J., Brough N., Mills, G. P., Penkett, S. A., Lewis, A. C., Lee, J. D., Saiz-Lopez, A., and Plane J. M. C.: Peroxy radical chemistry and the control of ozone photochemistry at Mace Head, Ireland during the summer of 2002, Atmospheric Chemistry and Physics, 6, 2193-2214, 2006a.

Fuchs, H., Brauers, T., Häseler, R., et al.: Intercomparison of peroxy radical measurements obtained at atmospheric conditions by laser-induced fluorescence and electron spin resonance spectroscopy, Atmos. Meas. Tech. Discuss., 1, 375-399, 2008.

Gerbig, C., et al.: Fast response resonance fluorescence CO measurements aboard the C-130: Instrument characterisation and measurements made during North Atlantic Regional Experiment 1993, J. Geophys. Res. 101, 29229-29238, 1996.

Green, T.J., Brough, N., Reeves, C.E., Edwards, G.D., Monks P.S., and Penkett, S.A.: Airborne measurements of peroxy radicals using the PERCA technique, J.Environ.Monitoring., 5, 75-83, 2003.

Guenther, A., Hewitt, C.N., Erickson, D., Fall, R., Geron, C., Graedel, T., Harley, P., Klinger, L.,Lerdau, M., McKay, W.,A., Pierce, T., Scholes, B., Steinbrecher R., Tallamraju, R., Taylor,J., and Zimmerman, P.: A global-model of natural volatile organic-compoundemissions, J.Geophys. Res., 100 (D5), 8873-8892, 1995.

Hard, T. M., O'Brien, R. J., Chan, C. Y., and Mehrabzadeh, A. A.: Tropospheric free radical determination by FAGE, Environ. Sci. Technol. 18, 768–777, 1984.

Hastie, D.R., Weißenmayer, M., Burrows, J.P., and Harris, G.W.: Calibrated chemical amplifier for atmospheric ROx measurements, Anal. Chem. 63, 2048-2057, 1991.

Hayman, G.D.: Numerical Model of the Calibration Source of a PERCA Instrument, AEAT-24737/20410001/001, 1997.

Hofzumahaus, A., Brauers, T., Aschmutat, U., Brandenburger, U., Dorn, H.P., Hausmann, M., Heßling, M., Holland, F., Plass-Dülmer, C., Sedlacek, M., Weber, M.,and Ehhalt, D.H.: Reply Geophys. Res. Letters, 24, 23, 3039-40, 1997.

Holland, F., M. Heßling, and A. Hofzumahaus: In-Situ measurement of Tropospheric OH radicals by Laser-Induced Fluorescence- A Description of the KFA Instrument, Journal of the Atmospheric Sciences (52), 3393-3401, 1995.

Holton, J.R., Haynes, P.H., McIntyre, Douglas, A.R., Rood, R.B., and Pfister, L. : Stratosphere-troposphere exchange. Rev. Geo-phys., 33, 403-439, 1995.

Houze, R, A., Jr. : Mesoscale convective systems, Rev. Geophys., 42, RG40003, doi: 10.1029/2004RG000150, 2004.

Kartal,D., Peroxy radical measurements under controlled conditions and further investigation of pressure dependence of PERCA for airborne measurements, Master Thesis, 2004.

Kartal,D., Andrés-Hernández, M.D., Reichert, L., Schlager, H., and Burrows, J.P.,: Characterization of a DUALER instrument for airborne measurements of peroxy radicals during AMMA 2006, submitted to AMMA special issue in Atmospheric Chemistry and Physics at July 2009.

Laube, M und Höller, H. Meteorologie: Physikalische und chemische Eigenschaften der Luft, Band V/4b von Landolt-Börnstein, Zahlenwerte und Funktionen aus Naturwissenschaft und Technik, Neue Serie, Kapitel 5 Cloud Physics. Springer Verlag, Berlin Heidelberg, 1988.

Lelieveld, J., Butler T.M., et al.: Atmospheric oxidation capacity sustained by a tropical forest, Letters to Nature, Vol 452, doi: 10.1038/nature06870, 2008.

Mari, C.H., Cailley, G., Corre, L., Saunois, M., Attié, J.L., Thouret, V., and Stohl, A.: Tracing biomass burning plumes from the Southern Hemisphere during the AMMA 2006 wet season experiment, Atmos.Chem.Phys., 8, 3951-3961, 2008.

Mathews, J.H., Fink, K.K.: Numerical Methods Using Matlab, 4th Edition, 2004. ISBN:0-13-065248-2.

McKeen, S.A., Gierczak, T., Burkholder J.B., et al.: The photochemistry of acetone in the upper troposphere: a source of odd-hydrogen radicals, Geophys. Res. Letters, Vol 24, No 24, 3177-3180, 1997.

Menke,W. Geophysical Data Analysis: Discrete Inverse Theory. Academic Press, Inc,1984.
Mihelcic, D., A. Volz-Thomas, H.W. Pätz, D. Kley, M. Mihelcic: Numerical Analysis of ESR Spectra from Atmospheric Samples, J. Atmos. Chem., 11,271-297,1990.

Mihelcic, D., D. Klemp, P. Müsgen, H.W. Pätz and A.Volz-Thomas: Simultaneous measurements of peroxy and nitrate radicals at Schauinsland, J. Atmos. Chem. 16, 313-335,1993.

Mihelcic, D., P. Müsgen and D.H. Ehhalt: An Improved Method of Measuring Tropospheric NO_2 and RO_2 by Matrix Isolation and Electron Spin Resonance, J.Atmos. Chem., 3, 341-361, 1985.

Mihele, C.M., and Hastie, D.R.: The sensitivity of the radical amplifier to ambient water vapour. Geophys. Res. Letters 25, 1911-1913, 1998.

Mihele, C.M., M. Mozurkewich, and Hastie, D.R.: Radical loss in a chain reaction of CO and NO in the presence of water: Implications for the radical amplifier and atmospheric chemistry, Intern. J. Chem. Kinetics, 31, 145-152, 1999.

Monks P.S., Carpenter, L.J., and Penkett, S.A.: Night-time peroxy radical chemistry in the remote marine boundary layer over the Southern ocean, Geophys. Res. Letters, 23, 5, 535-538, 1996.

Paulson, S. E., and J. J. Orlando, The reactions of ozone with alkenes: An important source of HO_x in the boundary layer, Geophys. Res. Lett., 23(25), 3727–3730, 1996.

Reeves, C.E., Formenti, P., Ancellet, G., et al.: Chemical characterisation of the West Africa Monsoon during AMMA, to be submitted to ACP, AMMA Special Section, 2009.

Reichert, L., Andrés Hernández, M.D., Stöbener, D., Burkert, J., and Burrows, J.P.: Investigation of the effect of water complexes in the determination of peroxy radical ambient concentrations: implications for the atmosphere, Journal of Geophys. Res, 108, D1, 4017-4032, 2003.

Reiner, T., Hanke, M., and Arnold, F.: Atmospheric peroxy radical measurements by ion molecule reaction mass-spectrometry: a novel analytical method using amplifying chemical conversion to sulphuric acid, J. Geophys. Res., 102, 1311-1326, 1997

Schlager, H., Konopka, P. Schulte, P., Schumann, U., Ziereis, H., Arnold, F., Klemm, M., Hagen, D., Whitefield, P., Ovarlez, J.: In situ observations of air traffic emission signatures in the North Atlantic flight corridor, J. Geophys. Res., 102, 10739-10750, 1997.

Schulte, P., Schlager, H., Schumann, U., Baughcum, St. L., Deidwig F.: NOx emission indices of subsonic long-range jet aircraft at cruise altitude: In situ measurements and predictions, J. Geophys. Res., 102, 21431 - 21442, 1997.

Schultz, M., Heitlinger, M., Mihelcic, D., and Volz-Thomas, A.: A calibration source for peroxy radicals with built-in actinometry using H_2O and O_2 photolysis at 185nm. J. Geophys. Res. 100, 18811-18816, 1995.

Seinfeld H. J., Pandis S.N. : Atmospheric Chemistry and Physics, Wiley&Sons 1997. ISBN: 0-471-17816-0

Stöbener, D., Weiterentwicklung einer peroxyradikalquelle für die Kalibration von RO_2-Messungen in Außenluft, Diplomarbeit,Universität Bremen, 1999.

Stohl, A., and Seibert, P.: Accuracy of trajectories as determined from the conservation of meteorological tracers. Q. J. Roy. Met. Soc., 124, 1465-1484, 1998.

Stohl, A., Wotawa, G., Seibert, P., and Kromp-Kolb, H.: Interpolation errors in wind fields as a function of spatial and temporal resolution and their impact on different types of kinematic trajectories. J. Appl. Meteor., 34, 2149-2165, 1995.

The International Science Plan for AMMA, May 2005.

Volz-Thomas A., Pätz, H.-W., Houben, N., Konrad, S., Mihelcic, D.,Klüpfel, T., and Perner, D.: Inorganic trace gases and peroxy radicals during BERLIOZ at Pabstthum: An investigation of the photostationary state of NO x and O 3, J. Geophys. Res., 108 (D4), 8248, doi:10.1029/2001JD001255, 2003.

Wayne P.R : Atmospheric Chemistry , Oxford University Press, 2000. ISBN: 0-19-855571-7.

Wendel, G.J., Donald H. Stedman and Christopher A. Cantrell: Luminol-based Nitrogen Dioxide Detector. Anal. Chem. 55, 937, 1983.

Wittrock, F., Richter, A., Oetjen, H., Burrows, J.P., Kanakidou, M., Myriokefalitakis, S., Volkamer, R., Beirle, S., Platt U., and Wagner, T.: Simultaneous global observations of glyoxal and formaldehyde from space, Geophys. Res. Letters, Vol 33, L16804, doi: 10.1029 / 2006GL02 6310, 2006.

Yienger, J.J., and Levy, H.: Empirical-model of global soil-biogenic NOx emissions, J. Geophys.Res., 100 (D6), 11447-11464, 1995.

Yoshino, K., D. E. Freeman, J. R. Esmond, and W.H Parkinson: High resolution absorption cross section measurements and band oscillator strengths of the (1,0)-(12,0) Schumann-Runge bands of O_2. Planet Space Sci., 31, 339-353, 1983.

Zanis, P., Monks, P.S., Green, T.J., Schuepbach, E., Carpenter, L.J., Mills, G.P., Rickard, A.R. and Penkett, S.A.: Seasonal variation of peroxy radicals in the lower free troposphere based on observations from the FREE Tropospheric Experiments in the Swiss Alps, Geophysical Research Letters . 30 (10), 1497, doi:10.1029/2003GL017122, 2003.

Ziereis, H., Schlager, H., Schulte, P., van Velthoven, P., and Slemr, F.: Distributions of NO, NOx, and NOy in the upper troposphere and lower stratosphere between 28 and 61° N during POLINAT 2, J. Geophys. Res., 105, 3653-3664, 2000.

Zimmerman, P.R., Greenberg, J.P., and Westberg, C.E.: Measurements of atmospheric hydrocarbons and biogenic emission fluxes in the amazon boundery-layer, J. Geophys.Res., 93 (D2), 1407-1416, 1988.

Acknowledgements

The long residence of me at the Institute of Environmental Physics of University Bremen as a master student and a PhD. student was a collection of experiences for my scientific and social background.

During this present work as in every work, the motivation, the patience had a minus slope. At these situations, Maria Dolores Andrés Hernández (Lola) had always the formula or the methodology to change the direction of the slope. I want to thank a lot to Lola for her scientific leading during this work and for her friendship.

It is an honour for me that Prof. Dr. J.P. Burrows supervised this work and that I felt always the trust of him behind me. Thanks a lot to the support of Prof. Dr. J.P. Burrows with his ability to teach how to see the light at the end of dark tunnels during this work. The results of the discussions during this work with him enabled me to distinguish if the light at the end of the tunnel is belonging to a train or to the sun.

Special thanks to Lars Reichert, for sharing his experiences in the experimental work and for no ending discussions about every subject.

Thanks to Petra Schumacher for her supports at the preparations for the measurement campaigns and in laboratory experiments.

Without the efforts of mechanical workshop of the Institute of Environmental Physics this work would not come to the end. Thanks to Elke Sorgenicht, Andre Brünkers and Simone Eilers and all members of the mechanical workshop.

I want to thank Juan Carlos Gómez Martín for the spark of the modelling study of this work.

I want to thank also to Vladyslav Nenakhov, Markus Horstjann, Anna Chrobry for the advices during this work.

Finally, I want to thank to my wife Derya Kartal for the tees and coffees during the long nights and for her patience.

Curriculum Vitae

Personal Information

Name:	Deniz Kartal
Birth place:	20.04.1975 in Radolfzell am Bodensee
Marital status:	Married
Citizenship:	Turkish

Education

04/2002-08/2004	Master Degree at theUniversity of Bremen; Department of „Environmental Physics“ Experimental Master Thesis at the University of Bremen; Subject: “Peroxy radical measurements under controlled conditions and further investigation of pressure dependence of PERCA for airborne measurements” Degree: Master of Science in Environmental Physics Overall Grade: „B”
10/1994 – 06/2001	Bachelor Degree as Physics Engineer at Technical University of Istanbul (ITU) Thesis at Technical University of Istanbul; Subject: “Solar Energy as an Alternative Energy Source at 21.Century” Overall Grade: „B” Degree: Bachelor of Science in Physics

09/1987 - 06/1994	60th Year Anatolian High School, Izmir, Turkey
09/1982 - 06/1987	Cemil Akyüz Ilkokulu (Primary school), Izmir, Turkey

Work Experience

07/2005-…….	Research scientist at the Environmental Physics Institute at the University of Bremen.
03/2002-09/2004	Laboratory Assistance as a master student at the Environmental Physics Institute at the University of Bremen.
08/2000 – 12/2001	Laboratory Technician at British International Schools, Istanbul

Language Skills

Turkish (Native Language)

German (good at communication)

English (speaking and writing good)

Computer Skills

Computer skills:	Software Skills:
	MS-Office
	Programming-Language:
	MATLAB,
	SOLID EDGE,
	Agilent Vee Pro 6.0 (DT Vee)
	Labview

LIST of PUBLICATIONS

- Kartal, D.: Solar Energy as an Alternative Energy Source at 21. Century, Senior Thesis , 2001.

- Kartal, D.: Peroxy radical measurements under controlled conditions and further investigation of pressure dependence of PERCA for airborne measurements, Master Thesis , 2004.

- M.D. Andrés Hernández, D.Kartal, L. Reichert and J.P. Burrows: PERCA Airborne measurements: Chain length variation with pressure and temperature, Poster, Leeds, 2005.

- D.Kartal, M.D. Andrés Hernández, L. Reichert, H. Schlager and J.P. Burrows : Peroxy radical observations over West Africa. Part1: Measurements on the board DLR-Falcon, Poster, Karlsruhe, 2007.

- M.D. Andrés Hernández, D.Kartal, L. Reichert, H. Schlager and J.P. Burrows : Peroxy radical observations over West Africa. Part2: Vertical distribution measured during SOP2, Poster, Karlsruhe, 2007.

- D.Kartal, M.D. Andrés Hernández, L. Reichert, V.Nenakhov, and J.P. Burrows: Further characterization of Dual channel reactor system (DUALER) used for measurements on the board DLR-Falcon during AMMA SOP2, Vienna, 2008.

- Andrés-Hernández, M. D., Kartal, D., Reichert, L., Burrows, J.P, Arnek , J. M., Lichtenstern, M., Stock, P., and Schlager, H.: Peroxy radical observations over West Africa during the AMMA 2006: Photochemical activity in the outflow of convective systems, Atmos. Chem. Phy., 9, 3681-3685, 2009.

- Kartal,D., Andrés-Hernández, M.D., Reichert, L., Schlager, H., and Burrows, J.P.,: Characterization of a DUALER instrument for airborne measurements of peroxy radicals during AMMA 2006, submitted to AMMA special issue in Atmospheric Chemistry and Physics at July 2009.